Mathematical models to improve complex-valued fMRI in the presence of motion, confounding physiologic phenomena, and temporal variations in bulk B0 magnetic field inhomogeneity

Andrew D. Hahn

August 12, 2011

Contents

List of Figures

List of Tables

Committee Members

Daniel B. Rowe[1,2] (Advisor)
Gary H. Glover[3,4,5,6]
James S. Hyde[1,8]
Robert W. Prost[1,8]
Kathleen M. Schmainda[1,8]

[1] Department of Biophysics, Medical College of Wisconsin, Milwaukee, Wisconsin, United States
[2] Department of Mathematics, Statistics and Computer Science, 1313 W. Wisconsin Ave., Milwaukee, WI, 53233
[3] Department of Radiology, Stanford University, Palo Alto, California, United States
[4] Department of Neurosciences, Stanford University, Palo Alto, California, United States
[5] Department of Biophysics, Stanford University, Palo Alto, California, United States
[6] Department of Electrical Engineering, Stanford University, Palo Alto, California, United States
[7] Department of Psychology, Stanford University, Palo Alto, California, United States
[8] Department of Radiology, Medical College of Wisconsin, Milwaukee, Wisconsin, United States

For Molly and Owen, with sincere gratitude and love

Acknowledgements

There are innumerable people who, throughout my life both personally and professionally have had some sizable impact on the course I have chosen, currently culminating in the work contained within this reasonably substantial document. I can only specifically mention a few here, but I acknowledge them all the same.

My family deserves more recognition here than I can express. My parents have been excellent role models and always encouraged education for the sake of knowledge, experience and richness it brings to life. My brother has helped me learn patience and humility, but in all seriousness has been a great source of support, confidence and friendship. My grandparents have also always encouraged learning and critical thinking. I feel I have been blessed in my relationships with them and they make up much of who I am and what I do today. My wife has stood in a class by herself these past few years. She keeps me sane, supporting me during struggling times and making sure I remember all my shortcomings when I start to have too high an opinion of myself. She has sacrificed and done what was needed at all times. I cannot say enough. I also feel I must mention her parents as well, especially for their efforts over the few months since the birth of our son. They have helped babysit, keep house and yard and provided me the time needed to finish my graduate work.

My advisor, Dr. Daniel Rowe, who has been a great person to work with over the years. I have learned so much from him and his ability to handle the way I work, specifically my tendency to be very independent and isolated at times, has made this experience both worthwhile and enjoyable.

The other members of my committee have influenced my work in their own ways. Dr. Kathleen Schmainda has been a great teacher and Dr. James Hyde has often been a reliable source of advice. Both they and Dr. Robert Prost and Dr. Gary Glover have provided insightful feedback and suggestions with respect to my work and helped me become a better investigator. Importantly, all of my committee members are outstanding members of and contributors to their fields. I have been motivated by the honor of having such outstanding researchers guiding and evaluating my own efforts.

At the Medical College of Wisconsin, I feel I should mention Dr. Andrzej Jesmanowicz, who has not only been a great instructor, but has helped me invaluably in my efforts to tame the scanner at times. Dr. Vinai Roopchansingh helped me get on my feet when I first arrived and helped jumpstart my MRI data processing. The help and advice provided by Dr. Andrew Nencka, who was a graduate student in our

lab for the first three years of my studies, cannot be understated. He provides a great role model, has excellent understanding of MR physics and statistical processing and is extremely generous with his time and expertise.

Abstract

Typical fMRI experiments involve analysis of only the magnitude portion of the acquired signal to detect the functional response to an applied stimulus. However, there are potential benefits to using the fully complex-valued signal in fMRI. Purely in terms of mathematical advantage, statistical power can be increased in complex-valued models as opposed to magnitude-only only models simply due to the fact that twice as many data points are included. This can be important when sample size is small, but is less relevant with a large number of samples. Additionally, the complex-valued model appropriately characterizes the noise across the entire range of signal-to-noise ratio (SNR). This is generally not the case in magnitude-only models, which tend to mischaracterize the noise distribution at low SNR. Besides the statistical advantages, analysis of both magnitude and phase can be applied to potentially enhance investigation into functional brain activity, since the physiologic information encoded in the phase is likely to be quite different than that of the magnitude. However, noise in the phase component of the complex-valued fMRI signal is much more pronounced and detrimental to statistical analysis than that in the magnitude. This complex-valued noise, its effect on complex-valued statistical modeling of the functional response, and the development and demonstration of techniques to alleviate its detrimental impact are the main themes of this dissertation. We repeatedly demonstrate in this work that application of complex-valued models to typically processed fMRI time series is generally impractical due to significant un-modeled signal variance. However, we also show that by modeling and correcting for the temporal fluctuations in the main B0 magnetic field, complex-valued time series characteristics and statistical analysis greatly improve. We describe the theoretical development of the model for estimating the temporally dynamic field fluctuations and characterize its performance in simulated, phantom and human fMRI data in a variety of situations. We further develop the post-processing model by incrementally including, along with the dynamic field correction, covariates of bulk motion and the "nuisance" physiologic phenomena of respiration and heart beat in the complex-valued linear regression model applied to test for the presence of functional activity. It is shown that, while the dynamic field correction easily provides the most significant benefit in terms of noise reduction, the highest performance is obtained by including both motion and physiologic covariates in the model along with applying the field correction. In this case, complex-valued noise variance and temporal characteristics (including statistical distribution and independence) are vastly improved. Finally, we demonstrate the application of this full model in fMRI data acquired under conditions typically difficult to analyze, which include data acquired in the presence of swallowing or chewing. In all, this work shows the obstacles that must be overcome when performing complex-valued analysis and develops and evaluates a model with which to do so robustly. In the process, we present further evidence of the potential benefits of complex-valued analysis.

Chapter 1

Introduction

Reliable utilization of the complex-valued data for analysis of functional MRI (fMRI) time series has been the main goal of our recent work. There are a number of theoretical advantages of complex-valued techniques beyond what the standard magnitude-only methods can provide, but the former is essentially never applied in practice. Over the course of our work, we have identified some of the underlying reasons for this and developed methodology to attempt to negate them. We present these developments in this work and demonstrate how our progress has narrowed the gap between the theoretical potential and the reality of complex-valued fMRI.

In the first of the six chapters of this dissertation, we present the background for the motivation for and methods for performing complex-valued fMRI. Additionally, we review the sources and effects of noise in fMRI along with the techniques often used to suppress them. The significant challenges facing realistically reliable complex-valued modeling are demonstrated experimentally in chapter 2, although this is a theme of the entire work and is emphasized throughout. This chapter also presents the model for estimation and correction of temporal variations in the bulk B_0 magnetic field. These field fluctuations have a significant impact on the acquired data, most notably in the phase, and this technique provides the backbone for our noise and artifact reduction processing. The following two chapters investigate the impact of complex-valued regression with covariates of motion and physiologic phenomena (heart rate and respiration), both with and without the dynamic field correction. These chapters also continue to provide insight into the temporal characteristics the of complex-valued fMRI, both as acquired and following application of these corrections. Chapter 5 demonstrates a few of the types of complex-valued analytics that can be obtained when the data is corrected using the model developed over the previous three chapters. These results are a strong indication that the potential applications and advantages of complex-valued analysis of appropriately corrected data may be within reach. The final chapter provides a summary and we discuss potential areas of future research that would build upon the progress made so far.

1.1 Functional MRI Contrast

Traditional fMRI involves detecting signal changes, or contrast, between two or more different states of functional stimulation. Here, we briefly discuss certain physiologic correlates of brain activity and their expected impact on signal contrast, both in the magnitude and phase.

1.1.1 BOLD

The blood oxygenation level dependent (BOLD) signal [1] is the basis for nearly all fMRI experimentation. As its name indicates, it manifests from hemodynamic changes, specifically changes in blood oxygenation, that occur in response to neuronal activity. When neurons increase their activity, the blood flow to and the oxygen consumption at the active cortical site increase disproportionately, yielding a higher blood oxygen concentration both at and downstream of the active cortex. Because deoxyhemoglobin is paramagnetic but oxyhemoglobin is not, the presence of the former leads to an increase in the magnetic susceptibility of the blood, and vice versa. Since the blood susceptibility is dependent on the relative concentration of deoxygenated and oxygenated hemoglobin, but the surrounding tissue is not, the difference in susceptibility between the two varies with oxygenation. Precisely, the difference in their susceptibilities decreases as oxygenation increases, resulting in a more homogeneous magnetic field within a voxel containing both tissue and blood vessels. The spin system within the voxel is thus more coherent and signal intensity increases.

BOLD is typically associated with magnitude contrast, but can produce phase contrast in certain situations as well. If a voxel contains large or coherently oriented vessels, the magnetic field changes resulting from the reduced blood susceptibility can be coherent enough across the voxel to produce a net phase shift [2]. Complex-valued response modeling may be useful for differentiating different vascular morphologies [3, 4].

1.1.2 Non-BOLD

Other types of contrast can also be used to study brain function. Among them is arterial spin labeling (ASL), which provides blood flow measurements by using endogenous blood tagged by an inversion pulse for contrast [5]. Magnitude-only statistical analysis is typical here as well, but complex-valued analysis could be beneficial, especially due to the commonly low signal-to-noise ratio (SNR) of the technique [6]. Diffusion weighted fMRI is another technique used to generate functionally related contrast [7, 8]. Blood flow, volume and susceptibility changes can all affect the apparent diffusion, and other physiologic effects, such as cell swelling, have been suggested as possible mechanisms for functional diffusion contrast as well. The estimation of the diffusion coefficients usually involves a fit of the magnitude data, but complex-valued methods may prove useful for this type of technique as well [9].

The potential contrast arising directly from neuronal action potentials is an attractive investigative tool because is would be a direct indication cortical activity, opposed to traditional BOLD contrast which is a non-specific correlative effect. This technique, termed neuronal current MRI (ncMRI), has not been proven feasible at this time but continues to be an active area of research [10, 11, 12, 13, 14]. Models have been proposed and simulations performed that suggest that the response to neuronal firing manifests in the magnitude and phase [15, 16, 17], indicating that complex-valued analytical techniques may offer the best chance for detection.

1.2 Statistical Modeling of fMRI Time Series

A least squares regression model is generally used to determine the presence of functionally related contrast [18]. As we have previously mentioned, this is typically performed on only the signal magnitude, and is relatively straightforward. However, the MRI signal is inherently complex-valued. Converting this signal into the magnitude has two detrimental consequences: (1) while noise in the real/imaginary data is normally distributed, the noise structure in the magnitude is only normally distributed at high SNR and (2) it reduces the number of data values to be fit by half.

Even if no significant response is expected in the phase (i.e. the signal of interest is effectively real), fitting the complex-valued data can alleviate these issues.

Simultaneous fitting of the magnitude and phase, opposed to fitting each individually, is required to appropriately model the noise due to the fact that the noise, which is independently additive to the real and imaginary data, is coupled when converted to magnitude and phase. Unfortunately, the magnitude and phase have a non-linear relationship with the acquired real and imaginary data, suggesting a non-linear least squares approach to fitting a model. While this is possible, linear techniques are preferred. While a variety of linear models have been proposed to consider special cases of complex-valued regression modeling, the most general that appropriately considers the noise and allows general simultaneous modeling of both magnitude and phase is that from Rowe [19]. Arbitrary groups of covariates may be fit to both magnitude and phase, and maximum likelihood statistics can be computed for a range of hypothesis tests. Using this type of model, (1) all the acquired data can be used in the fit, theoretically increasing detection power, (2) noise is modeled appropriately to account for the coupled uncertainty in magnitude and phase covariate coefficient estimations so fits are accurate even at low SNR, and (3) contrast, or lack thereof, can be modeled and tested for in both magnitude and phase.

A less commonly utilized technique for fMRI analysis is independent component analysis (ICA) [20]. This is a data driven technique that separates the signal into a specified number of independent components, one or more of which is expected to be related to a functional response. It is advantageous in that no model need be specified, as that model is extracted from the data itself, but disadvantageous in that the true number of components in the signal cannot be known. In any case, application of this method in the complex domain has been presented by Calhoun et al. [21], and it could be used in lieu of a model such as that described above.

1.3 Noise in Complex-valued fMRI Time Series

In order to reliably detect the presence of a functionally related signal embedded in an fMRI time course, the relative strength of the signal of interest to the noise must be high enough. Additionally, models which estimate the signal in the presence of noise assume it has certain properties, such as an independent and identically normal distribution. Thermal sources of noise are unavoidable and have the desired characteristics, but a variety of other "noise" components can be present in the time series that not only reduce detection power by increasing signal variance, but often have undesirable properties that violate model assumptions. We discuss here how two main sources of noise, subject motion and physiologic processes such as respiration and heart beat, induce noise in the magnitude and phase of fMRI data. The effects of changes in bulk susceptibility, often caused by these processes, is explained as well.

Respiration can be associated with bulk head motion in certain cases, and blood oxygenation and blood flow are modulated by the respiratory cycle as well [22]. This in turn modulates the blood susceptibility and thus results in a respiration related BOLD response that is strongly dependent on the phase of the respiratory cycle and the depth of respiration [23, 24, 25]. The cardiac cycle also modulates blood flow, and induces a pulse in the flow of blood and cerebrospinal fluid. This effect is dependent on cardiac cycle phase during acquisition, and is typically a spatially local phenomenon, most apparent near the sulci, ventricles and blood vessels [26]. The manifestation of these processes in the signal is expected to be similar to typical BOLD contrast, in that it is dependent on the coherence of the susceptibility and flow changes with a voxel volume. When flow or susceptibility changes coherently over voxel sized spatial scales, as might be expected in ventricles and larger vessels, phase change is expected. Otherwise magnitude signal change will result.

The obvious result of bulk motion occurring between the i^{th} and j^{th} acquisitions is the reflection of the same bulk motion represented in the i^{th} and j^{th} reconstructed volumes. An additional consequence, far more important with respect to phase noise, is that tissues with different magnetic susceptibilities are reoriented. This causes a change in the magnetic field, which can be quite detrimental. Besides bulk motion within the field of view, motion outside the field of view can induce significant fluctuations in the magnetic field within the imaging plane. This includes involuntary chest wall motion associated with respiration or voluntary movement such as swallowing, speaking or chewing [27, 28]. As a significant portion of the work in the following chapters pertains to these fluctuations and removal of their effects, we will provide somewhat more detailed background here.

First, we present the equation describing the signal which is acquired in MRI,

$$s(t) = \iint \rho(x,y,t) e^{\left(i \left\{ \gamma \int_0^t \left(xG_x(\tau) + yG_y(\tau) + \Delta B(x,y,\tau) \right) d\tau + \Phi_0(x,y) \right\} \right)} dxdy. \tag{1.1}$$

Here ρ is the proton spin density, γ is the gyromagnetic ratio, G_x and G_y are the x and y magnetic field gradients, ΔB is the difference in the strength of the magnetic field from resonance, Φ_0 is the initial phase of the radio frequency pulse, and s is the acquired signal in time. The variable t is the time elapsed since the application of the RF excitation pulse. Here we don't explicitly show the inherent tissue relaxation properties, T_1 and T_2, which can be grouped into the ρ function for our purposes. The important term here for our purposes is $\Delta B(x, y, t)$. We can separate it out and express Eq. 1.1 in slightly different terms

$$b\left(x, y, t\left(k_x, k_y\right)\right) = e^{\left(i\left\{\gamma \int_0^{t(k_x,k_y)} \Delta B(x, y, \tau) d\tau + \Phi_0(x, y)\right\}\right)} \tag{1.2}$$

$$s(k_x, k_y) = \iint b\left(x, y, t\left(k_x, k_y\right)\right) \rho(x, y) e^{i2\pi\,(k_x x + k_y y)} dx dy \tag{1.3}$$

$$k_x = \gamma \int_0^t G_x(t) dt, \qquad k_y = \gamma \int_0^t G_y(t) dt, \tag{1.4}$$

where the variable t from Eq. 1.1 is now the function tk_x, k_y, and represents the time between the RF pulse and acquisition of the (k_x, k_y) point. If we inverse Fourier Transform both sides of Eq. 1.3 and recognize that its right hand side is equal to the Fourier Transform of ρ multiplied by b, then we obtain the actual reconstructed image, $\rho' = IFT\{s\}$, in terms of the true image, ρ, convolved with the inverse Fourier Transform of b, B.

$$B\left(x, y, f\left(u, v\right)\right) = \iint b\left(x, y, t\left(k_x, k_y\right)\right) e^{i2\pi\,(k_x x + k_y y)} dx dy \tag{1.5}$$

$$\rho'(u, v) = \iint \rho(x, y) B\left(x, y, f\left(u - x, v - y\right)\right) dx dy \tag{1.6}$$

Equation 1.6 represents a convolution of ρ with a kernel that varies according to points in the reconstructed image. Each point $\rho'(u_i, v_i)$ is computed by convolving $\rho(x, y)$

with $B(x, y, f(u_i, vi)$. Intuitively, B provides a mapping between where points in the true space will be mapped to in the reconstructed space due to the off-resonance. Expressing the form of the B kernel, which is the inverse Fourier Transform of Eq. 1.2, is relatively straightforward if we make the assumption that ΔB is time invariant over the course of the acquisition. Ignoring the constant Φ_0 term for the moment, the assumption of time invariance reduced Eq. 1.2 to

$$b\left(x, y, t\left(k_x, k_y\right)\right) = e^{i\gamma\Delta B(x,y)\,(t_p(k_x,k_y)+TE)} \tag{1.7}$$

$$t_p = t - TE, \qquad t_p(k_x = 0, k_y = 0) = 0, \tag{1.8}$$

where the change in the timing function is made so that it is independent of the echo time, TE. We note here that t_p is a pulse sequence dependent function, and we can use to define a pulse sequence dependent kernel in response to a unit off-resonance, h_{psq}, that is dependent on this timing alone. The B kernel can then be expressed in terms of h_{psq},

$$h_{psq}(u, v) = IFT\left\{e^{i\gamma t_p(k_x,k_y)}\right\} \tag{1.9}$$

$$\begin{aligned} B(x, y, f(u, v)) &= IFT\left\{e^{i\gamma\,(t_p(k_x,k_y)+TE)\,\Delta B\,(x,y)}\right\} e^{i\Phi_0} \\ &= h_{psq}\left(\frac{u}{\Delta B(x,y)}, \frac{v}{\Delta B(x,y)}\right) e^{i\,(\gamma\Delta B\,(x,y)\,TE+\Phi_0)}. \end{aligned} \tag{1.10}$$

An important consequence of this result is that a spin at location (x, y) will accumulate a phase equal to the product of the off-resonance at that point and the echo time, independent of the pulse sequence trajectory. If ΔB is relatively constant in a voxel, a phase change will be observed and if it is variant over small spatial scales, spins will destructively interfere.

In cartesian echo-planar imaging (EPI), which is the pulse sequence used in the experimentation to follow, the timing function is $t_p(k_x, k_y) = t_{esp}k_y$, where t_{esp} is the time between acquisition of the $k_x = 0$ point in adjacent k_y lines. This assumes each k_y line is acquired instantaneously, which is reasonable. The off-resonance kernel, h_{epi}, is then

$$h_{epi} = \delta\left(u, v + \frac{\gamma t_{esp}\Delta B\left(x, y\right)}{2\pi}\right)e^{i\left(\gamma\Delta B\left(x, y\right)TE + \Phi_0\right)} \tag{1.11}$$

which indicates that the off-resonance causes a shift along the y direction in the image, i.e. geometric warping, in addition to the phase accumulation. If the off-resonance varies from image to image, the warping will vary in time as will the image phase. Additionally, if sub-voxel gradients in ΔB fluctuate as well, it can lead to variations in image intensity and potentially phase.

1.4 Noise Reduction in fMRI Time Series

Noise resulting from motion is generally corrected retrospectively by performing bulk image registration of all acquired volumes to a reference, or base, volume. The first step in the process is to estimate the motion itself. This is usually done in images space through a least squares approach to minimizing the residual error between each volume and the base [29], but k-space based methods have been proposed as well, which may offer some advantages [30]. It is also not uncommon to regress the fMRI time series using the motion parameters as nuisance covariates to remove addition motion correlated noise [31]. This can be an issue, of course, if motion happens to be correlated with task.

Physiologically related noise, specifically in terms of respiratory and cardiovascular processes, is generally handled through nuisance regression of waveforms which correlate with the response to the phenomena in the acquired signal. In order to accomplish this, seperate monitoring of respiration and heart rate is required, using any number of different types of equipment to do so. One of the most commonly used methods to generate compensatory waveforms and remove the offending signal components is RETROICOR [32]. This method involves generating a low order Fourier series basis for functions of respiratory and cardiac cycle phase at the point of image acquisition, fitting these to the data and removing the fitted components. This is designed to eliminate signal that is time locked to the respiratory and cardiac phase. More recently, other work has shown that other covariates of these processes may also be useful, for example respiration volume per time (RVT) [23]. Investigation into the impulse response functions associated with respiration and heart rate has also been presented [24, 33].

It should be noted that the above mentioned techniques were designed for and are almost exclusively used for correction of the magnitude. Some recent effort has been made to investigate the impact of RETROICOR correction in phase data, however [34].

The noise that results from time variability in the magnetic field, as discussed in the previous section, is nearly never directly corrected for. Off-resonance of the magnetic field is typically treated as static over the course of a time series, and all images are corrected with a single field map for the purposes of removing geometric distortions, which improves registration to higher resolution anatomical data. Additionally, some of the corrections for motion and physiologic processes will indirectly correct some of the effects arising from field fluctuations. If off-resonance changes are spatially uniform, as often is the case with respect to respiration induced fluctuations, the shifting of voxels as described by Eq. 1.11 will also be uniform and will imitate bulk motion. It will also be correlated with respiration so nuisance regression of respiratory waveforms will indirectly remove some of these effect as well. As will be shown over the course of the remainder of this work, the effect of time variant off-resonance is not terribly detrimental in the magnitude, but is terribly so in the phase. Characterizing and reliably removing these effects is the topic of the following chapter.

Chapter 2

Temporal fluctuations in the B_0 magnetic field

The topic of this chapter, which marks the beginning of the report on our main experimental findings, involves the development and implementation of a novel method for estimating and subsequently correcting signal errors arising from temporal fluctuations in the main magnetic field. The underlying motivation for undertaking this task is an apparent underperformance of complex-valued statistical modeling of fMRI data, specifically in this case with a complex-constant phase model. Additionally, no existing methods were robust enough to perform the required task. After presenting the theoretical basis for the model of the field dynamics, we present data from phantom, simulated and human experimental data. In the phantom we demonstrate that the correction can reduce the signal changes arising from intentional disturbance of the field during the time series acquisition. Hypothetical fMRI data sets are then simulated with and without the influence of off-resonance variations in order to compare corrected data with an ideal control and to attempt to characterize the influence the field variations have on uncorrected results compared to controls. Finally, human fMRI data is acquired in subjects instructed to breathe heavily or perform jaw motions while simultaneously performing a finger tapping functional task. Magnitude only and complex-valued statistics are computed and compared before and after correction. Additionally, the signal component at the heavy breathing/jaw motion frequency is investigated before and after correction. The field correction unquestionably makes a significant difference in complex-valued analysis, which, at least using the complex-constant phase model, is essentially useless in uncorrected data under these conditions. The impact of correction in the magnitude is less apparent, but simulated data suggests there may be more subtle effects.

2.1 Introduction

Experiments in functional MRI (fMRI) often involve single-shot gradient echo echo-planar imaging (GE-EPI) pulse sequences to maximize acquisition speed and blood oxygenation level dependent (BOLD) contrast [35]. However, inhomogeneities in the static magnetic field can result in severe artifacts, most notably image warping and signal loss. Correcting these errors has been a consistent field of research. In general, this correction is a two-step process, involving estimation of the spatially dependent main field offsets followed by image correction based on the estimated map. The field map can be calculated in a variety of ways [36, 37, 38], often with two or more reference images acquired at different echo time (TE) values [36]. In practice, the field offsets are assumed to be temporally invariant, justifying the correction of an entire time series of images with a single map. Although large scale inhomogeneities are generally constant over experimental time series, this assumption fails when considering sensitive phase data due to the small scale changes associated with the resonance offset caused by the breathing cycle [39, 40] and slight changes in the orientation of tissue boundaries. The former is unavoidable in vivo, and subject movement, whether inside or outside the field of view, can cause non-negligible changes in the magnetic field due to reorientation of the aforementioned susceptibility profile. When the field changes, so does the induced spatial warping, which can have significant consequences. For example, this warping and its associated voxel intensity modulation can cause less reliable bulk motion correction [41]. In addition, spatial specificity is sacrificed as the point spread function associated with the off-resonance changes [42]. These phenomena are well known and often have non-negligible effects, most notably additional temporal (non-white) “noise” that reduces strength and specificity of activation statistics. Accompanying phase changes can have similar detrimental impact on complex, or phase sensitive activation models [2, 43]. In depth performance analysis of these methods and identification of their sensitivity to these potentially large phase variations has resulted in the recognition of the potential value of correcting for off-resonance dynamics [44]. An alternative method involves a model for magnitude activation in complex data, and has been developed to account for phase variations [19]. However, it can be difficult to provide valid regressors for phase, and even when properly modeled, dynamic image warping artifacts still remain, currently making this a less attractive solution.

Current methods to combat the problem of temporal field variations include low resolution field mapping with a type of dual-echo single-shot EPI [45], zero-order field offset correction using only a pair of navigator echoes [39, 46], and real-time magnetic field shimming based on a priori knowledge of the field changes resulting from a regular phenomena [47]. While each of these provides certain benefits, issues exist preventing their widespread use. Each method struggles to provide field maps with a combination of high resolution, SNR and spatial order to be useful to correct for commonly unpredictable and non-linear temporal field dynamics. Alternatively, effects from certain field variations may be removable without either field measurements or shimming by monitoring physiologic phenomena that influence field changes, such as breathing rate. Signal components at the measured frequencies can then be retrospectively accounted for [48]. This method not only requires the acquisition of physiologic information but may remove signal of interest aliased to the frequency of the physiologic fluctuations while failing to remove “noise” due to field changes arising from unmonitored sources.

One of the most common methods of field map estimation involves acquiring images at different echo times and comparing the difference in phase evolution between the two [36]. Given two images I_1 and I_2, with echo times TE_1 and TE_2 respectively, the general equation for the estimated resonance offset in a voxel at location (m, n), denoted by $\Delta\hat{\omega}(m, n)$ (radians/sec), can be written as

$$\Delta\hat{\omega}(m, n) = \frac{arg\big(I_2(m, n)I_1^*(m, n)\big)}{(TE_2 - TE_1)} \tag{2.1}$$

where $I_i(m, n)$ represents the complex value of the voxel with coordinates (m, n) in image $i = 1, 2$, $*$ denotes complex conjugation, and the arg operator returns the phase angle of its argument. The signal-to-noise ratio (SNR) of $\Delta\hat{\omega}(m, n)$ is proportional to the ratio of $TE_2 - TE_1$ (referred to as ΔTE) divided by the geometric mean of the standard deviation of the phase noise in the two images. Thus, increasing the difference in echo times decreases variation in the field map, but with such an increase, complicated phase wrapping can occur, along with an offsetting increase in phase variance resulting from the longer TE. These issues require the echo time difference be kept relatively short and multiple references are sometimes acquired to achieve the necessary accuracy [37], inherently requiring more time. For these reasons, it is not surprising that previous evaluation of methods based on Eq. 2.1 for dynamic field mapping has not produced promising results [49]. While the work of Hutton et al. [49] is not exactly contemporary, there is not, to our knowledge, more recent literature which evaluates the performance of these type of dynamic field mapping techniques. More current work has demonstrated the effectiveness of a prospective method based on real-time shimming to compensate for dynamic field fluctuations resulting from respiration [50]. This type of prospective method does not suffer from the aforementioned problems, however.

The recent method of Lamberton et al. [51] also utilizes Eq. 2.1 but assumes invariance of the RF pulse phase (and thus the initial spin phase, Φ_0) from shot to shot to alleviate the need for two unique images at each time point to calculate the corresponding field map. Rather, because Φ_0 is the same for all images, it can be used for reference (as I_1 is in Eq. 2.1) as the image phase at $TE = 0$. Additionally, this method provides a maximum ΔTE without increasing the echo time of each acquired image. However, because the static field will likely cause the phase of each image to wrap many times over the course of TE, complicated phase unwrapping procedures are necessary to find the correct phase accumulation in reference to the initial phase.

In order to apply the method, an initial measurement of Φ_0 is also required before acquiring the image time series.

The method of Lamberton et al. [51] can be extended to find the difference, $\delta\hat{\omega}_t$, between the resonance offset during acquisition of the t^{th} image, $\Delta\omega_t$, and the average resonance offset during the entire series acquisition, $\overline{\Delta\omega}$, rather than attempting to directly calculate the absolute resonance offset at each time point. Further analysis yields

$$\delta\hat{\omega}_t(m,n) = \frac{arg\left\{ I_t(m,n) \sum_{j=1}^{N} \frac{I_j^*(m,n)}{|I_j(m,n)|} \right\}}{(TE_2 - TE_1)} \tag{2.2}$$

for a series of N images with identical TE. This provides two significant advantages over the method as presented by Lamberton et al. [51]. First, while ΔTE remains TE, the phase of I_t will not normally differ by $> 2\pi$ from the average image phase (represented by the summation in Eq. 2.2), which removes the need for any phase unwrapping. Second, correction for temporal variations in off-resonance (using the $\delta\hat{\omega}_t$ measurements) can be performed without any reference at all, as $\delta\hat{\omega}_t$ does not depend on Φ_0. While a static effect would remain in this case, a single measurement of $\Delta\omega$ (similarly to Lamberton et al. [51]) provides the means to fully correct every image in a series with no need to apply any phase unwrapping. The benefit of the proposed method is mostly realized through the convenience of avoiding phase unwrapping and the ability to correct for field dynamics in the absence of any reference. Performance of the methods, determined by the accuracy of the measured fields, should be very similar, except when phase is incorrectly unwrapped, as both otherwise share similar sources of error.

2.2 Theory

The proposed method relies on the assumption that the initial spin phase, Φ_0, remains constant throughout the acquisition of a series of images, although the value of Φ_0 is inconsequential. The validity of this assumption is a significant topic of Lamberton et al. [51], and is well addressed in the literature. It is also true that, in general, any multi-shot imaging modality requires RF pulse consistency from shot to shot and as a result, Φ_0 is almost always necessarily assumed to be constant through time. Other field mapping methods making this assumption are commonly used with a great degree of success [37, 52], further illustrating its practical validity.

Let the value of Φ_0 represent the phase of an image, I_0, acquired with $TE = 0$. In other words, $\Phi_0(m, n) = arg\big(I_0(m, n)\big)$, where $I_0(m, n)$ is the complex value of the voxel with coordinates (m, n). The value of Φ_0 is assumed to be unknown, but constant from acquisition to acquisition in a series of N images, with each image in the series having echo time TE. Then from Eq. 2.1, the estimated magnetic field offset in the voxel with coordinates (m,n) in the t^{th} image, represented as $\Delta\hat{\omega}_t(m, n)$ (radians/sec) can be written as

$$\Delta\hat{\omega}_t(m, n) = \frac{arg\big(I_t(m, n) I_0^*(m, n)\big)}{TE} \tag{2.3}$$

The average estimated magnetic field offset present during the entire series acquisition in the voxel with coordinates (m, n), represented as $\overline{\Delta\hat{\omega}(m, n)}$, (in radians/sec) can be similarly written as

$$\overline{\Delta\hat{\omega}(m,n)} = \frac{arg\big(\overline{I(m,n)}I_0^*(m,n)\big)}{TE} \tag{2.4a}$$

$$\overline{I(m,n)} = \sum_{j=1}^{N} \frac{I_j(m,n)}{|I_j(m,n)|} \tag{2.4b}$$

Given the unknown nature of I_0, neither Eq. 2.3 nor Eq. 2.4a can be calculated directly. However, by writing $\Delta\hat{\omega}_t(m,n)$ in terms of $\overline{\Delta\hat{\omega}(m,n)}$ plus some offset, $\delta\hat{\omega}_t(m,n)$,

$$\Delta\hat{\omega}_t(m,n) = \overline{\Delta\hat{\omega}(m,n)} + \delta\hat{\omega}_t(m,n) \tag{2.5}$$

it is possible to solve for $\delta\hat{\omega}_t(m,n)$ by combining Eqs. 2.3 through 2.5, and rearranging the variables to arrive at Eq. 2.2, which does not directly depend on $I_0(m,n)$.

2.3 Materials and Methods

2.3.1 Simulation

A computer simulation was designed in Matlab (The Mathworks, Natick, MA, USA) to test the potential benefits of the time varying magnetic field correction on an fMRI series. First, gradient waveforms were generated for the given imaging parameters (GE-EPI, 96 × 96 matrix, $TE = 42.7$ ms, $BW = 125$ kHz, echo spacing= 0.708 ms, and FOV= 24 cm). Maps of spin density, transverse relaxation time and main magnetic field offset, denoted as $\rho(x,y)$, $T_2^*(x,y)$ and $\Delta B_0(x,y)$ respectively, were provided as input, and the k-space signal based on these three input maps and the generated gradient waveforms, G_x and G_y, was output according to

$$S(m\Delta t) = \sum_{q=\frac{-N_x}{2}}^{\frac{N_x}{2}-1} \sum_{r=\frac{-N_y}{2}}^{\frac{N_y}{2}-1} \rho(q\Delta x, r\Delta y) e^{\left(\dfrac{m\Delta t}{T_2^*(q\Delta x, r\Delta y)}\right)} \times e^{i\gamma\Delta t\left(\sum_{w=0}^{m}\big(G_x(w\Delta t)q\Delta x + G_y(w\Delta t)r\Delta y\big) + m\Delta B(q\Delta x, r\Delta y)\right)} \tag{2.6}$$

where N_x and N_y are the number of discrete points in ρ along the x and y dimensions. After acquisition of S, the samples are placed accordingly in the 2D k-space matrix for image reconstruction. In Eq. 2.6, Δt is not necessarily the sampling interval, but is the resolution with which the summation in the exponential is computed. The values of m at which samples are actually recorded are not necessarily sequential, and will be determined by the gradient sequence and other parameters. As Δx, Δy and Δt approach zero, the summations become better estimations of the integral representing the theoretical signal, but computation time grows quickly. With larger values, some error is induced through inability to properly account for k-space truncation and poorer modeling of the continuous image acquisition process.

Two different series of 276 images were created in this way using the same, temporally constant, $\rho(x, y)$ map for each series. In each series, identical magnitude and/or phase activations were simulated by locally modulating the value of T_2^* for magnitude change and ΔB_0 for phase change in a block design pattern (20 repetitions rest followed by 16 epochs of 8 repetitions active and 8 repetitions rest). Six different combinations of activation types and sizes were considered, indicated by pairs of T_2^*

ΔT_2^*	ΔB_0	CNR^{a,b}	$\Delta\Phi$	Series A (control)						Series B, static correction						Series B, dynamic correction					
(ms)	(nT)		(°)	z-statistics^a		β_0^a	β_1^a	β_2^a	σ^a	z-statistics^a		β_0^a	β_1^a	β_2^a	σ^a	z-statistics^a		β_0^a	β_1^a	β_2^a	σ^a
				MO	CP		$\times 10^7$	$\times 10^2$	$\times 10^2$	MO	CP		$\times 10^7$	$\times 10^2$	$\times 10^2$	MO	CP		$\times 10^7$	$\times 10^2$	$\times 10^2$
.432	0	1.24	0	4.09	4.12	.408	.49	2.68	1.08	3.71	1.18	.406	-4.56	2.58	1.15	3.91	3.66	.410	4.77	2.72	1.14
.216	9.17	.49	6	1.61	.941	.407	-1.88	1.06	1.08	1.64	.70	.405	-4.36	1.10	1.15	1.62	1.04	.408	4.92	1.14	1.14
.432	4.58	1.19	3	3.90	3.27	.408	1.99	2.56	1.08	3.63	1.14	.406	-4.70	2.51	1.15	3.73	3.11	.409	4.92	2.62	1.14
0	4.58	.07	3	-.25	-.24	.406	.84	-.15	1.08	-.16	.38	.404	-4.29	-.14	1.15	-.14	-.12	.407	4.88	-.09	1.14
.432	9.17	1.01	6	3.59	2.19	.408	-.67	2.38	1.08	3.48	1.06	.406	-4.35	2.41	1.15	3.50	2.29	.409	4.76	2.47	1.14
.216	4.58	.56	3	1.83	1.52	.407	-.92	1.20	1.08	1.75	.76	.405	-4.48	1.19	1.15	1.79	1.49	.408	4.92	1.25	1.14

Table 2.1: Simulation parameters and results

---

[a] Average value over all regions of interest.

[b] CNR= $\frac{\beta_2}{(2\sigma)}$

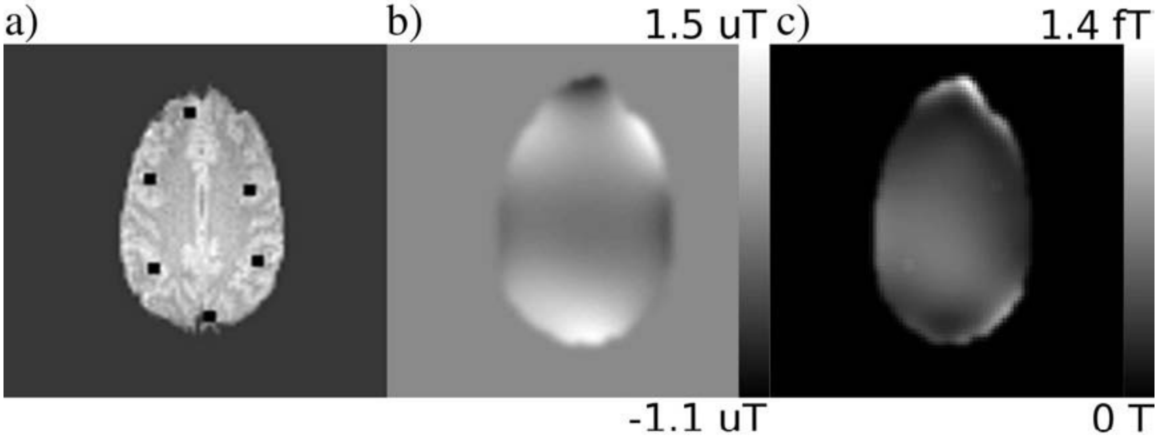

Figure 2.1: Spin density map, ρ, used for simulation (a). Regions of simulated activation are represented by black squares. The global, static field offset applied in simulation and the variance of the simulated dynamic field used in simulation are shown in b and c, respectively.

and ΔB_0 changes in the first two columns of Table 2.1. Each combination was simulated in 6 different 3 voxel by 3 voxel regions, shown in Fig. 2.1a. The use of the various locations is directed at averaging out the influence of differences in spatial contrast, size of field variations, and field gradients in the field offset.

The first of the two series (series A) was simulated under the influence of an additional global, *static*, ΔB_0 field, which is shown in Fig. 2.1b. The second series (series B) was simulated under the influence of a global, *time variant*, δB_0 field in addition to the aforementioned static field, so that the total field present was $\Delta B_0 + \delta B_0$. The variance of the time variant field is shown in Fig. 2.1c. All fields used for simulation were taken from fields modeled directly from experimental data of a human subject performing a deep breathing task at 0.167 Hz. The initial value of the δB_0 map for series B was equal to zero so that the initial field offset was identical for series A and B and equal to ΔB_0. In order to measure this initial field inhomogeneity, an additional 10 images were simulated using this initial ΔB_0 time point only, and images 2, 4, 6, 8 and 10 had the TE increased to 47.2 ms.

The only difference between series A and series B is the time varying portion of the magnetic field offset. As such, series A serves as a control, allowing for determination of the effect of the time varying field as well as the quality of the correction.

Series A was corrected for static field inhomogeneities using an initial measurement of the field offset, $\Delta\hat{\omega}_1$, acquired with the first 5 pairs of simulated images using Eq. 2.1. Series B was corrected in two different ways, firstly identically to the static correction for series A, and secondly using a dynamic field correction, using maps of $\delta\hat{\omega}_i$ calculated with Eq. 2.6. Subsequently, $\Delta\hat{\omega}_i$ was calculated for images 11 through 286 (the first 10 images were discarded after being used to find $\Delta\hat{\omega}_i$ as described above), and a fourth order polynomial was fit to each $\Delta\hat{\omega}_i$ map, helping to eliminate spatially varying random noise. Additionally, this process prevented the removal of the local high spatial frequency ΔB_0 modulations so that phase activations remained in the corrected time series. As a final processing step, the polynomial field models were allowed to smoothly fall to zero outside the object area by applying a mask over the imaged object, which had been previously dilated and smoothed by a Gaussian filter with FHWM of 4 voxels.

Once magnetic field estimations had been made using the proposed method, the appropriate corrections were applied using the Simulated Phase Rewinding (SPHERE) method [53]. In the static case, the initial $\Delta\hat{\omega}_1$ map was applied to each image, while the $\Delta\hat{\omega}_i$ map was used to correct the i^{th} image in the dynamic case. This provided a direct means to evaluate the effects of dynamic correction.

Activation statistics were calculated for each corrected time series using two different methods. The first method, most typically used, analyzes only the magnitude of the image time series, and is thus termed the magnitude-only (MO) method [54, 55]. This was implemented with a general linear model (GLM) with regression for constant and linear trends, as well as for the task reference function, which was equal to 1 during stimulus and -1 during rest. The second method used was the complex constant phase (CP) method [43]. This is a complex-valued linear model which models the phase as constant through time. If the phase contains time-variant signals, overall variance is increased resulting in a decrease in the significance of detected activity in the magnitude. This technique has been shown to be biased against voxels containing phase changes, and useful due to their likely association with venous macrovasculature [2, 44]. Comparisons between the activation statistics (z-statistics) from the different time series were made in order to gain insight into (i) how temporal variations in ΔB_0 affect the activation statistics, and (ii) the effectiveness of the dynamic field calculation (and subsequent correction) method in restoring the original activation.

2.3.2 Phantom

In addition to simulations, imaging experiments were performed. First, a spherical phantom filled with SiO_2 oil was imaged to evaluate the potential of the proposed dynamic field mapping method to correct for the effects of a time varying magnetic field offset in a controlled environment. The experiment was performed using a GE Signa LX 3T scanner (General Electric, Milwaukee, WI) with a GE-EPI pulse sequence (8 axial slices, 64 × 64 matrix, $TE = 44.1$ ms, $TR = 1$ s, flip angle= 45°, $BW = 125$ kHz, echo spacing= 0.624 ms, FOV= 24 cm, slice thickness= 3.8 mm, and 276 repetitions). During the acquisition of the images, perturbations in the main field were induced by manually moving a bottle filled with water along the InferiorSuperior axis at a rate of 0.2 Hz. These field perturbations would mimic those seen with motion outside of the field of view, such as breathing. This is in contrast to motion within the field of view, which would also cause field changes, but is not simulated here. The perturbation frequency of 0.2 Hz was chosen to approximate a normal breathing rate, but perturbation rate should not affect the results, as long as intra-acquisition effects remain small. The peak-to-peak displacement of the bottle was approximately 20 cm, and it was brought as close to the phantom as possible without entering the field of view. This resulted in field fluctuations on par with those measured in human data (see Figure 2.5 for comparison).

In this case, no initial reference of an absolute field offset map was calculated, i.e. only the maps of $\delta\hat{\omega}_i$ were estimated and applied, as correction for $\delta\hat{\omega}_i$ alone should reduce effects of the temporal variations in $\Delta\omega$.

The raw estimated maps were processed in an identical fashion to that described in section 2.3.1 and the SPHERE method of correction was used as well.

2.3.3 Human

Additionally, two separate imaging experiments were performed with a human subject to evaluate the dynamic field map corrections in vivo in two different situations where temporal changes in the magnetic field were likely to occur. Experiments were both performed using the same GE 3T scanner as for the phantom experiment. A GE-

EPI pulse sequence was used for both experiments (9 axial slices, 96×96 matrix, $TE = 42.8$ ms, $TR = 1$ s, flip angle= 45°, $BW = 125$ kHz, echo spacing= 0.768 ms, FOV= 24 cm, slice thickness= 2.5 mm, and 296 repetitions). Even repetitions up to repetition 20 had an increased TE of 47.8 ms and were used in Eq. 2.1 for calculation of $\Delta\hat{\omega}_1$. The first 20 repetitions were subsequently discarded, leaving the last 276 repetitions for further analysis. Smaller voxel size (and thus longer TE) was used to increase the effect of the field variations, which are smaller in these experiments than in the phantom.

Each experiment involved a combination of two tasks. The task common to both was visually cued bilateral finger tapping (the "functional" task), which followed a simple block design (20 s off, 16 epochs of 8 s on, 8 s off, for 0.0625 Hz task on/off frequency, starting at repetition 21). In the first experiment, the second task was deep, heavy breathing at a rate of 0.167 Hz. The second experiment replaced the heavy breathing with opening and closing of the jaw at the same rate. In each case, the timing of the second task was cued visually along with the "functional" task cue. The purpose of the second, "field modulating" task, was to modulate the main field at a known rate in order to make the effects on the time series clear and to allow more straightforward evaluation of the correction.

The experimental design provides an initial estimate of the field offset, $\Delta\hat{\omega}_1$, and thus, both static and dynamic correction were performed in the same manner as described for the Simulation. Again, the SPHERE method was used to apply the correction.

Following the correction for the magnetic field offset, each corrected image series was motion corrected using the AFNI [29] 3dvolreg program. Motion correction was applied to the magnitude images only, as is usually the case. Available motion correction techniques are not optimized for complex valued data and are thus not applied. The evaluation of such techniques, although necessary, is beyond the scope of this manuscript.

The processing resulted in four time series for each experiment: static field corrected with and without motion correction; and dynamic field corrected with and without motion correction. Activation statistics using both the MO and CP methods were computed in the same manner as described for the Simulation, only in this case, the first 10 images were discarded to allow the magnetization to reach steady state and the task reference function was delayed 4 s to account for hemodynamic delay. Because motion correction was applied only to magnitude data, complex activation statistics were not calculated after applying the motion correction.

2.4 Results

2.4.1 Simulation

In order to analyze the effects of the time varying magnetic field as well as the quality of the correction method, 100 iterations of each image series were processed, each with the addition of random, normally distributed noise added to both the real and imaginary channels of the simulated k-space signal. The amplitude of the added noise was such that the maximum contrast to noise ratio in the magnitude signal was approximately 1. Because six different combinations of magnitude and/or phase activations were used, a total of 600 iterations of each series were performed, with

100 iterations for each of the different activation sizes in each region.

The statistics generated for Fig. 2.2 originate from images simulated with a unique activation type from Table 2.1 in each region (iterated 100 times). The top left ROI (Fig. 2.1a) contains the combination from the first row of Table 2.1 (no ΔB_0 change) and the regions were assigned the remaining combinations, down the rows of Table 2.1, in clockwise order. The mean values (z-statistics, beta coefficients) are computed from 100 samples, and the power being referred to is the percentage of times a voxel was active above a $p = 0.01$ unadjusted threshold.

The nearly total lack of voxels with a mean CP z-statistic above threshold (Fig. 2.2d) as well an almost complete loss of power (Fig. 2.2f) after static correction alone is precisely the expected result in the presence of the time variant field. Additionally, the losses appear nearly completely recoverable after dynamic correction. The observed detrimental effects, which are not accounted for by the static correction, can be attributed to phase changes caused by the variable field, which are greatly reduced by the dynamic corrections. Such variations will result in abnormally high complex residuals, reducing statistical significance in voxels that have no true physiologically related phase changes. Dynamic warping and shifting in the image from field variations can be visualized through the regression beta coefficients of the static images (Figs. 2.2g and h). The regression attempts to model the signal changes due to these effects, which are most apparent from elevated beta coefficients in areas of high spatial contrast, such as the object boundaries. Again, these undesirable signal components are largely diminished after dynamic correction.

The effect on MO activations and power (Figs. 2.2a through c) is not as clear, but

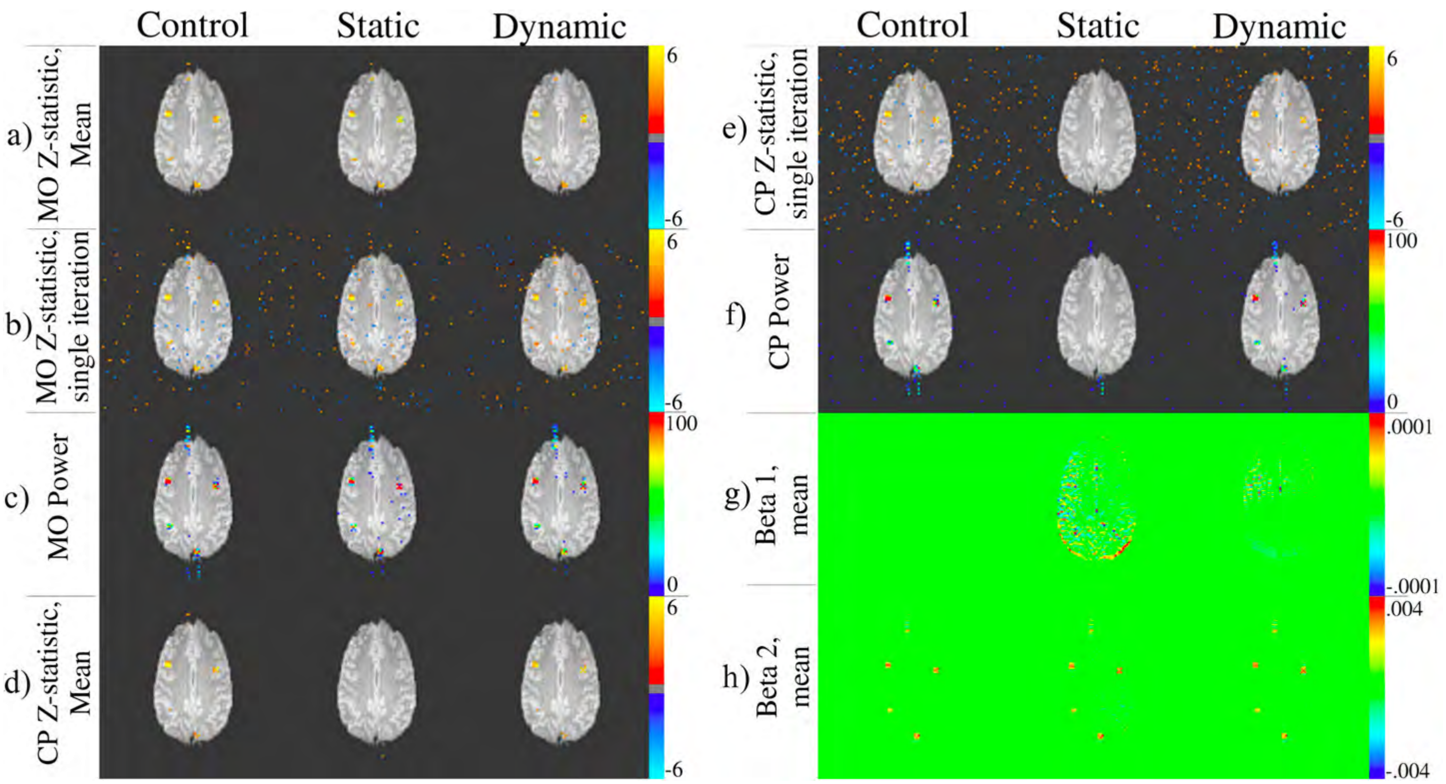

Figure 2.2: fMRI statistics resulting from simulated activation. Control refers to data set simulated with no dynamic field variations. Static and dynamic refer to the correction applied to the data set simulated with dynamic field changes. z-statistic maps shown with an unadjusted threshold of $p < 0.01$. All power maps shown with threshold of power $\geq 5\%$. Most notable are the loss of statistical power in the constant phase (CP) statistics (d-f) in the static case and the recovery of power after dynamic correction. Magnitude-only (MO) statistics (a-c) do not show much difference between cases.

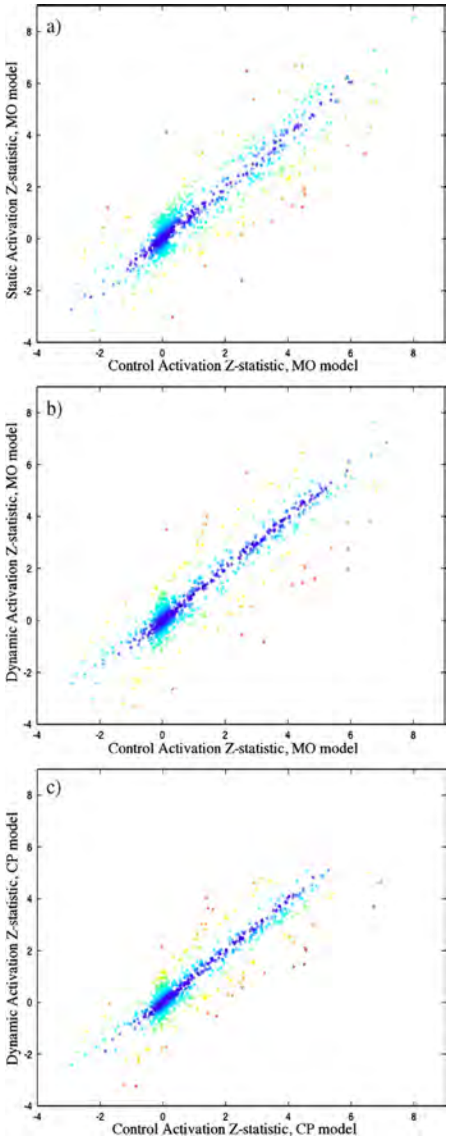

Figure 2.3: Scatter plots of mean MO z-statistics for static correction vs. control (a) and dynamic correction vs. control (b). Also shown, a scatter plot of mean CP z-statistics for the dynamic correction vs. control (c). Points are color coded by the amount of variation of the dependent variable from the control (small variation = dark blue, large variation = red). z-statistics following dynamic correction appear closer to the control z-statistics than those following static correction (i.e. less scatter around a straight line in (b) than in (a)).

comparison of the two correction methods against the control suggests that the field variations reduce the precision and accuracy of the calculated activations, with evidence provided in Figs. 2.3 and 2.4. The data displayed in these figures, as well as that used in the following analysis, comes only from voxels within the six ROIs after expanding the regions by 2 voxels on each side. The apparent tighter clustering of points around a 45° line in Fig. 2.3 and narrower error distributions in Fig. 2.4 with correction suggest that the statistics tend more often toward the control (expected) value than without. To confirm this, concordance correlation coefficients [56] between the control and both the static and dynamic mean MO activation z-statistics were computed to determine the reproducibility of the true (control) activations in each, resulting in values of 0.902 ($z = 1.485$, $p = 0.069$) and 0.919 ($z = 1.58$, $p = 0.057$) respectively. High coefficients (low p-values) suggest the presence of a *one-to-one* relationship between data sets, in contrast to the Pearson correlation coefficient, which detects *any* linear relationship. These results provide evidence for better reproducibility in dynamically corrected images. Additionally, the variance of the mean MO z-statistic error (from the control) in the static and dynamic results were $\sigma^2_{stat} = 0.623$ and $\sigma^2_{dyn} = 0.512$ respectively, with a hypothesis test of H_0: $\sigma^2_{stat} \leq \sigma^2_{dyn}$ vs. H_a: $\sigma^2_{stat} > \sigma^2_{dyn}$ resulting in $p = 0.0018$ ($F(899, 899) = 1.215$). Additionally, the variances of the error in the power are $\sigma^2_{stat} = 199.74$ and $\sigma^2_{dyn} = 174.91$, and the same test results in $p = .0233$ ($F(899, 899) = 1.142$). It is also important to note that t-tests for non-zero mean of the error in all of these cases is not significant. This evidence strongly suggests that 1) on average, MO statistics in dynamically corrected data will have less variation about the true value, and 2) with correction, the probability that voxels will be above

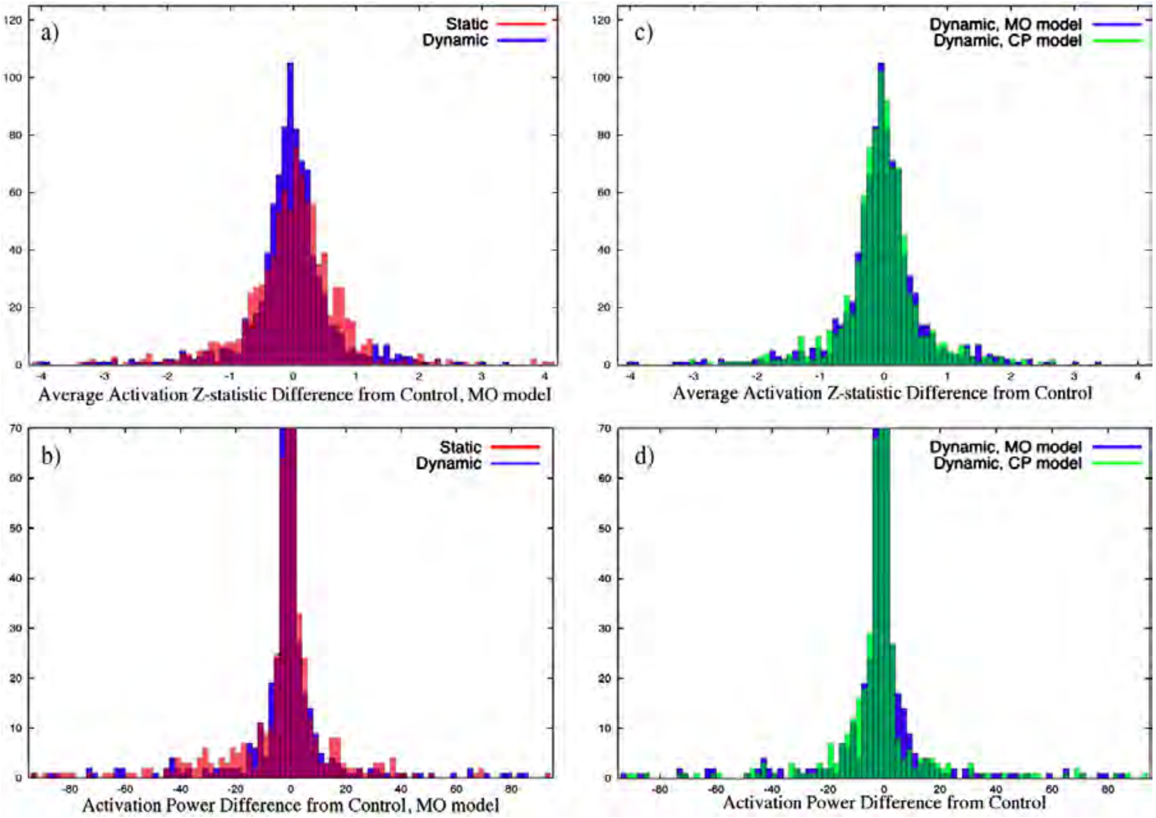

Figure 2.4: Histograms of static and dynamic mean MO z-statistic error, defined as difference from control (a), static and dynamic MO power error (b), MO and CP z-statistic error after dynamic correction (c), and MO and CP power error after dynamic correction (d). Voxels included in the analysis contained regions defined by expanding the active ROIs (see Fig. 2.1a)) by 2 voxels on each side. ROI's were expanded by 2 voxels to capture any errors in static or dynamic corrected data associated with a shift in the area of detected activity.

the threshold chosen here will be closer to the probability of being above threshold in the absence of any changing field.

Similar comparison can be made between the two statistical models with dynamic correction. The dynamic and control mean CP z-statistics have a concordance correlation coefficient of 0.911 ($z = 1.53, p = 0.063$), indicating reproducibility similar to that of the MO statistics. A test of H_0: $\sigma^2_{dyn,MO} \leq \sigma^2_{dyn,CP}$ vs. H_a: $\sigma^2_{dyn,MO} > \sigma^2_{dyn,CP}$, where $\sigma^2_{dyn,CP}$ and $\sigma^2_{dyn,MO}$ represent the CP and MO power error variances, does not provide a significant result ($\sigma^2_{dyn,MO} = 174.91$, $\sigma^2_{dyn,CP} = 165.00$, $F(899, 899) = 1.06$, $p = 0.193$). However, the same test with $\sigma^2_{dyn,CP}$ and $\sigma^2_{dyn,MO}$ equal to the mean CP and MO z-statistic error variances respectively, results in $p < 0.005$ ($\sigma^2_{dyn,MO} = 0.512$, $\sigma^2_{dyn,CP} = 0.390$, $F(899, 899) = 1.312$), providing evidence supporting a reduction in statistical error variation across voxels for the CP model when used in conjunction with the dynamic correction.

The validity of previous analysis using the F-test for difference in variance between populations relies on normally distributed and independent populations. The distributions in Fig. 2.4 appear normally distributed and correlations between populations were moderate ($r < 0.45$) in all cases, with the exception of the final test between the mean CP and MO z-statistic error variances after dynamic correction ($r = 0.975$). Correlation between populations will reduce the significance of these tests, however the large sample sizes used will diminish the effect. To appropriately qualify the significance of the results, the null distribution of the random variables was verified for every test case by Monte Carlo simulation (10,000 iterations).

2.4.2 Phantom

The variance of the induced field perturbations is shown in Fig. 2.5a. The effect that these magnetic field dynamics have on the series of phantom images can be visualized well through the voxel power spectra. Fig. 2.6 displays the power spectrum of the magnitude signal from a particularly affected voxel, emphasizing the large component

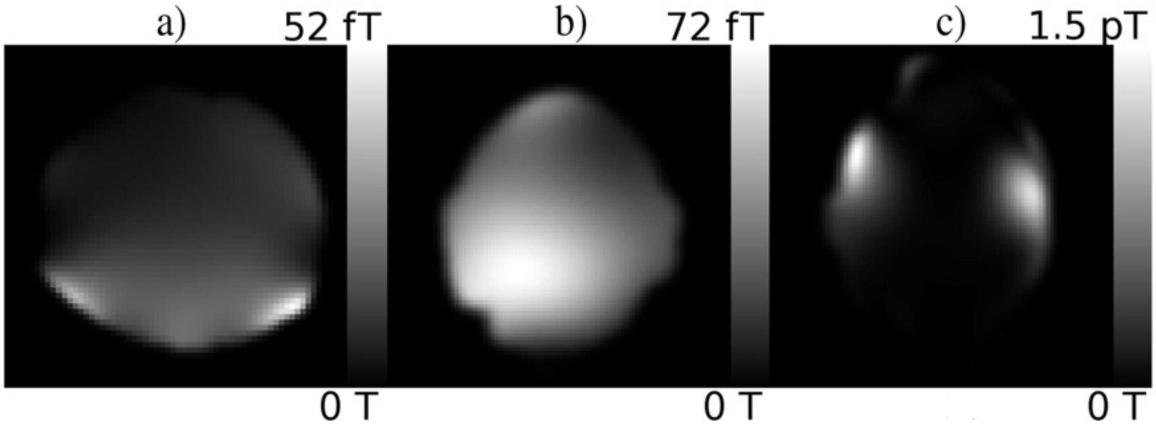

Figure 2.5: Maps of the temporal variance in the estimated magnetic field during the phantom, human data with heavy breathing, and human data with jaw motion experiments are shown in a, b and c respectively. Maps were computed from axial slices.

at approximately 0.2 Hz corresponding to the frequency of the field perturbations. The voxel-wise amplitude of the power spectrum at 0.2 Hz (Figs. 2.7a and b) gives a good indication of the effect of the time varying field in both the magnitude and the phase through time. Two important things are made clear by these images. First, the most affected voxels in the magnitude power spectra occur in areas of high spatial contrast along the phase encoding direction (top to bottom), as expected. Second, the stronger amplitude in the power spectra near the bottom of the image reveals the origin of the applied field perturbations.

Further evidence of the effect of the temporal field perturbations is provided through two regression analyses. The first fit a 0.2 Hz sinusoid, including regressors for a constant and linear trend. The sinusoid phase was determined by the 0.2 Hz component in the image phase time course. The sinusoid regression coefficients

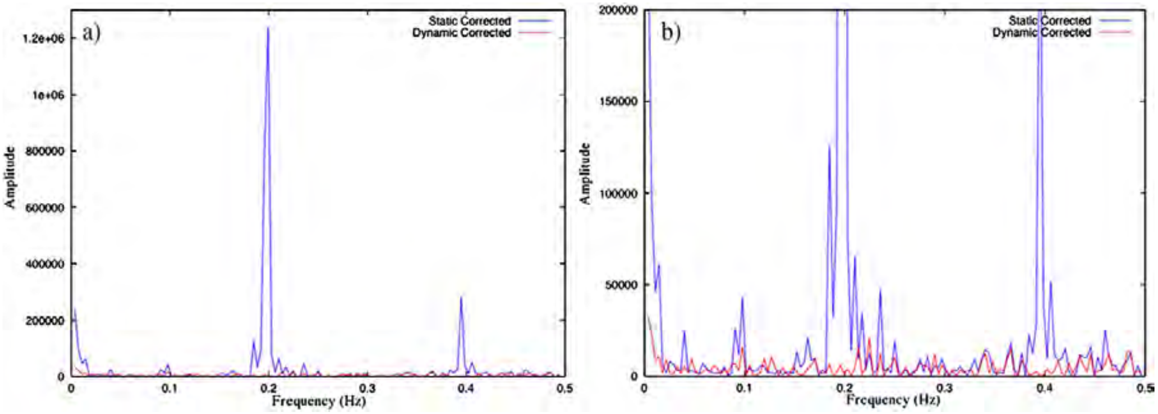

Figure 2.6: Power spectra of a single voxel time series with (red) and without (blue) correction. The same plot is shown full scale (a) and at reduced scale (b).

(Fig. 2.7c), whose values indicate the effect of the field variations on the voxel magnitude, are largest in areas of high spatial contrast, in agreement with the previous data. In the second regression the sinusoid reference was removed and the variance of the residuals (shown in Fig. 2.7d) was used as the indicator of the size of the effect of the changing field, with larger residuals implying larger effects. These results are consistent with the previous evidence shown in Figures 2.7a and c.

The desired consequence of the dynamic correction is reduced signal characteristics correlating with applied field perturbations while maintaining a similar level of noise. This is demonstrated by reduction of the large 0.2 Hz peak in the power spectrum (Figs. 2.6, 2.7a and 2.7b), and Fig. 2.6 shows reduction in several smaller structural components, while the noise floor appears consistent. The results of the regression analyses are similar. Specifically, Fig. 2.7d further suggests that no additional signal is induced by the correction, which would increase the residuals shown here.

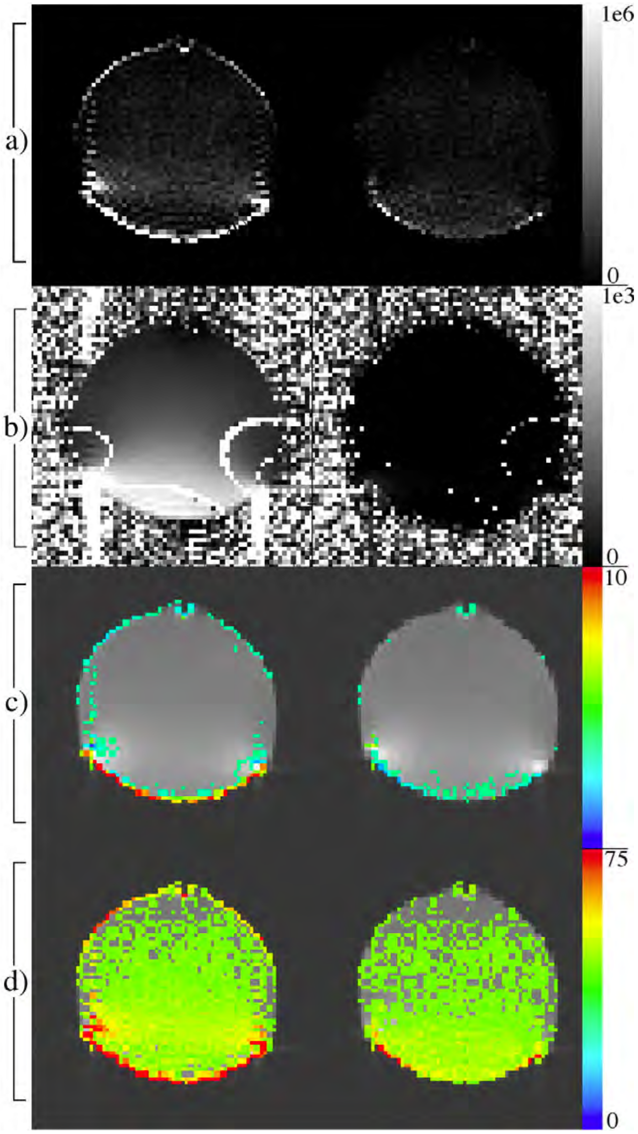

Figure 2.7: Voxel-wise maps shown are amplitudes of the magnitude (row a) and phase (row b) power spectra at 0.2 Hz, regression coefficients of a 0.2 Hz sine wave (row c) and mean squared error of a regression fit of a constant and linear reference (row d). Row c and row d shown with threshold of 2 and 17.5 respectively. Images on the right and left correspond to data with and without dynamic correction respectively. Dynamic field correction reduces the 0.2 Hz signal and reduces error variance compared to the uncorrected data.

2.4.3 Human

The temporal variance in the estimated magnetic field is shown for the heavy breathing and jaw motion experiments in Figs. 2.5b and c. The activation z-statistic maps computed for both the MO and CP models (Fig. 2.8) show recovery of CP activation statistics after correcting for the dynamic field as suggested by simulation. At a false discovery rate (FDR) corrected threshold for multiple comparisons [57] of $p < 0.05$, practically all of the complex activation is eliminated in the static case for both experiments. Also corroborating simulated results, dynamic correction has a less obvious impact on the MO activations. Activation maps (not shown) resulting from the same finger-tapping task with no intentional field perturbations showed similar results, although the change in the complex activation was not quite as dramatic. Although the correction appears to provide little at the provided threshold in this case, further analyses gives evidence for a benefit of dynamic correction in the magnitude of the image time series which could lead to more significantly improved activation statistics for tasks with less robust active response or requiring motion nearer to the imaging field of view.

The power in the magnitude signal at 0.167 Hz (Fig. 2.9) illustrates how the dynamic correction reduces the effect of the time varying field. In both experiments, the dynamic correction alone reduces the unwanted signal component. However, both field perturbation tasks are likely accompanied by correlated head motion within the field of view, which will not be removed by any field correction. Therefore, it's not surprising that the best results in both cases result from performing dynamic field correction followed by bulk motion correction. Results of the heavy breathing

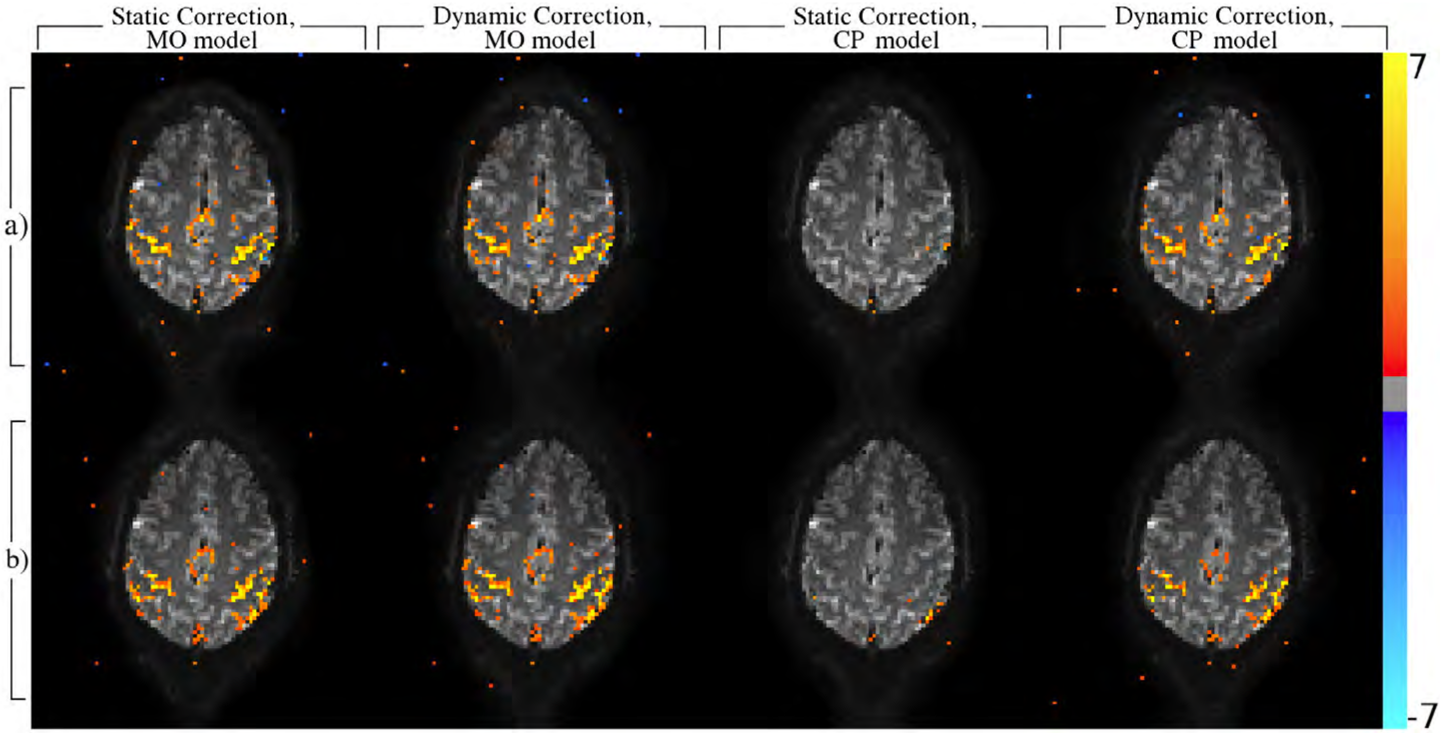

Figure 2.8: Activation maps (z-statistic) corresponding to a finger tapping task in a single slice in experiments where the subject was asked to additionally breath heavily at 0.167 Hz (row a) or open and close their mouth at 0.167 Hz (row b). Voxels were considered active at a FDR corrected threshold of $p < 0.05$. This demonstrates that dynamic correction restores the CP activation detection power compared to static correction only.

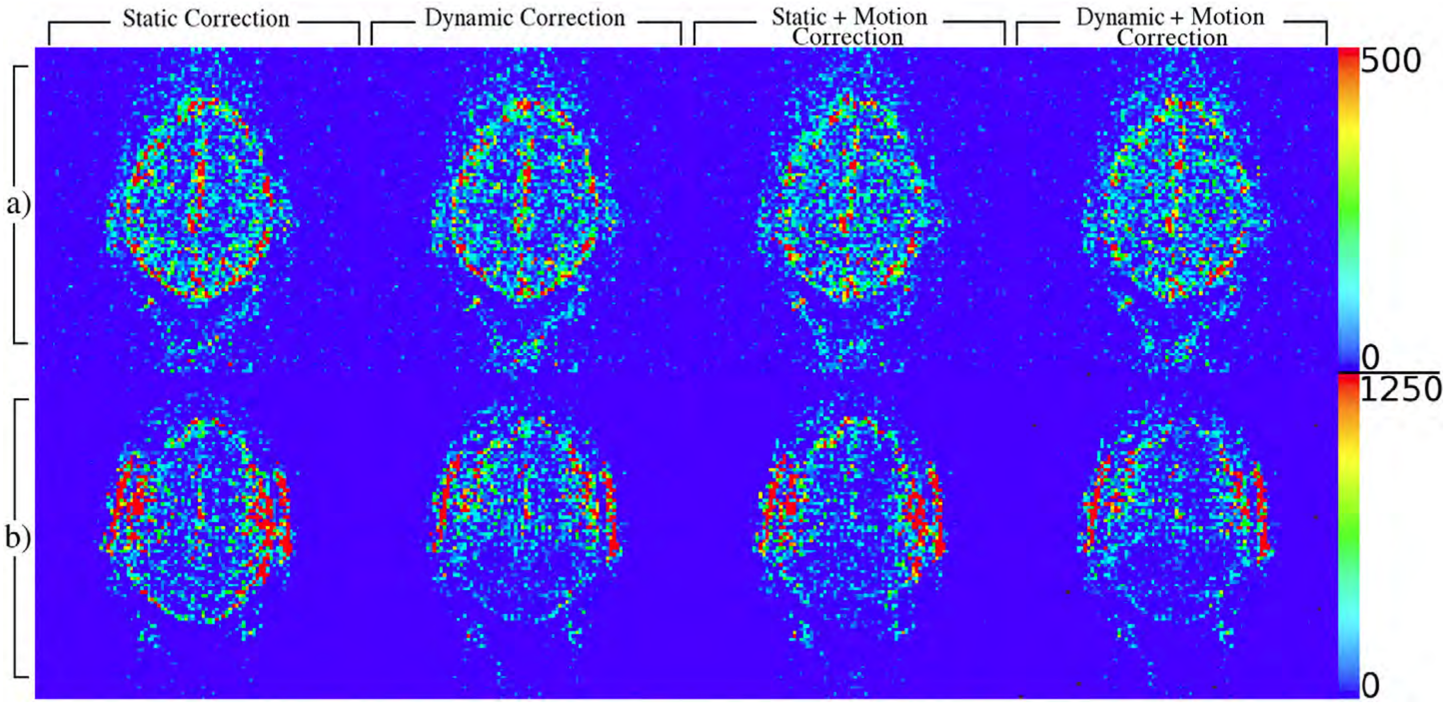

Figure 2.9: Maps of the 0.167 Hz peak amplitude in the voxel-wise magnitude power spectrum from experiments involving heavy subject breathing at 0.167 Hz (row a) or subject jaw motion (open/close) at 0.167 Hz (row b) computed after various combinations of field and motion corrections. In both experiments, the greatest reduction in the power at 0.167 Hz is achieved after both dynamic field and motion correction.

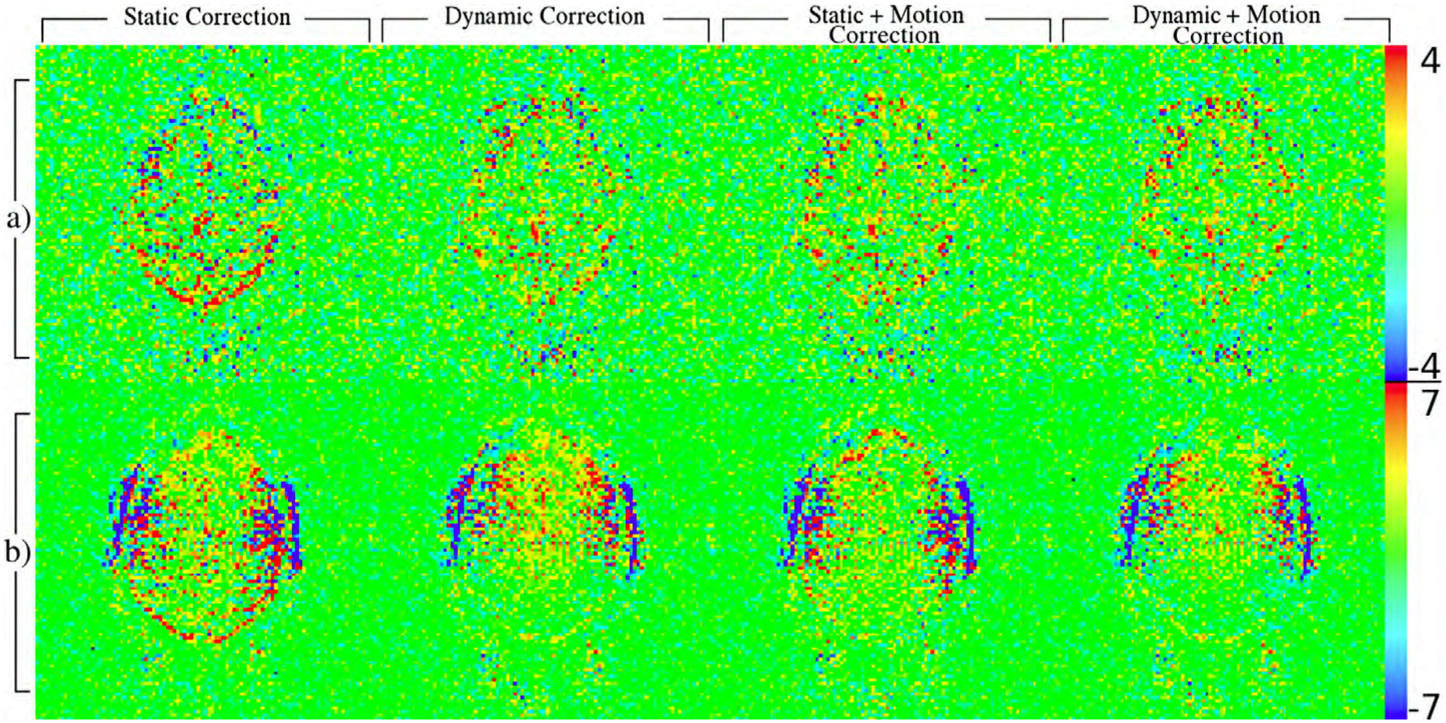

Figure 2.10: Maps of the regression coefficients for 0.167 Hz sine wave from experiments involving heavy subject breathing at 0.167 Hz (rowa) or jaw motion (open/close) at 0.167 Hz (row b) computed after various combinations of field and motion corrections. In both experiments, the 0.167 Hz sinusoid is least prevalent after both dynamic field and motion correction.

experiment (Fig. 2.9a) suggest that field changes were relatively constant spatially, and a very small amount of breathing related head motion occurred. The slight improvement resulting from motion correction, indicated by reduction in the 0.167 Hz signal power, even after dynamic correction, is evidence for the presence of true motion. However, the ability of motion correction alone to provide similar results is likely due to spatial constancy in field variations, which would manifest as apparent bulk motion and is thus correctable as such. With jaw motion (Fig. 2.9b), field changes predictably had more spatial variability, preventing motion correction from performing as well without the dynamic field correction.

A multiple regression analysis was performed as well, which fit a 0.167 Hz sinusoid in addition to the constant, linear and finger tapping task reference functions used for the activation models (Figs. 2.10a and b). These results are in good agreement with the previous data, and support the same conclusions.

Finally, quality of the bulk motion correction parameters calculated by 3dvolreg was evaluated using the root mean square (RMS) error between each volume repetition in the series and the volume used as the base for alignment. A paired t-test of H_0: $\mu_{ERR,stat} = \mu^2_{ERR,dyn}$ vs. H_a: $\mu_{ERR,stat} \neq \mu^2_{ERR,dyn}$, where $\mu_{ERR,stat}$ and $\mu_{ERR,dyn}$ are the mean RMS error after static and dynamic correction respectively, resulted in $p \ll 0.0001$ ($t = 6.24$) in the heavy breathing experiment and $p \ll 0.0001$ ($t = 12.73$) in the jaw motion experiment. This significantly supports the conclusion that dynamic correction improves subsequent motion correction and, predictably, benefit is increased as the field changes become more spatially variant, i.e. the differences in the variations over space contain higher order terms.

2.5 Discussion

The results of our investigations consistently show how temporal changes in the magnetic field can largely confound statistics that rely on models of phase that do not account for these effects. More interestingly, the strikingly positive results of dynamic correction for complex data analysis are demonstrated with a similar consistency, and similar benefits would be expected when using other phase sensitive statistical models [2, 58]. Additionally, evidence suggests the dynamic correction improves the ability to perform motion correction and can reduce temporal magnitude signal components likely induced by temporal field variations. This is especially true in areas most susceptible to these changes, such as areas of high spatial contrast along the phase encoding direction. However, the data shown reveals little change in the MO activations after performing the correction. When the variation in the magnetic field is relatively constant over space, as often results from breathing, motion correction alone provides comparable results to the dynamic correction in the magnitude signal. However, when the field changes with significant spatial variability, bulk motion correction alone was not able to match the performance of the dynamic field correction. In either case, however, motion correction was improved when applied after the dynamic correction. Also, the indirect effect of bulk motion on phase cannot be removed with bulk motion correction, but the dynamic correction accomplishes this as well.

Better results may be achievable by utilizing more effective correction methods than SPHERE. The inverse approaches [59, 60] have shown the ability to provide improved intensity correction, especially in the presence of large field gradients. These techniques require field maps estimated in non-warped space, which is not the case for this method, preventing their use. However, investigation into methods of applying these or similar techniques to dynamic field mapping is underway.

This straightforward method requires no additional reference scan, specialized pulse sequences or hardware. In addition, it can be applied to any previously acquired GE-EPI data set where complex data is available. It is, however, only applicable to single shot GE-EPI and can be applied retrospectively. Neglecting computation time, the summation in Eq. 2.2, representing the average phase of all images, could be computed from a subset, such as the first 25 images in a series, to enable pseudo-real-time application of the corrections. Possibly the most important potential drawback is the dependence on the temporal invariance in the phase of the radio frequency pulse. However, nearly every multi-shot imaging method relies on this invariance to hold true. However, extreme amounts of movement within the transmit coil can alter its loading and thus the homogeneity of the B_1 field phase. This is unlikely to occur within the range of routine scans [51], even those requiring small amounts of head movement.

Overall, the proposed method for measuring and subsequent correction of MRI time series for effects of temporal dynamics in the main (static) magnetic field, which we will refer to as TOAST (Temporal Off-resonance Alignment of Single-echo Time-series), has shown the capability of restoring statistical power to the complex constant phase fMRI activation model. Simulation results also indicate that the dynamic correction results in more robust statistics, which more reliably represent the true underlying activation. While it is difficult to directly conclude this from experimental data, there is clear evidence showing reduction in undesired signal components correlating strongly with known temporal magnetic field variations, suggesting this to be the case.

Chapter 3

Enhancing detection of complex-valued functional activity

The work in this chapter builds upon the Temporal Off-resonance Alignment of Single-echo Timeseries (TOAST) dynamic field correction of the previous chapter by including nuisance regression of motion covariates in the complex-valued linear model. We compare TOAST with nuisance regression, i.e. including covariates of signal not-of-interest in the multiple linear regression model, as well as application of both together with each other and with uncorrected time series. In data sets from a human asked to breathe heavily or move their jaw while performing a functional task, we compute and compare magnitude-only, phase-only and magnitude and phase activations using a more general complex-valued linear model than the complex-constant phase model utilized in the preceding experimentation. This allows us to demonstrate that the corrections not only stabilize the phase, but preserve functionally related response in magnitude and phase. We also present time series analysis of the complex-valued residuals of the linear model following different corrections, specifically in terms of their normality and temporal independence. A simulation designed to emulate the human fMRI data sets is also performed and identical analysis presented. Finally, we compute complex-valued activations in a more typical fMRI data set which is not corrupted by a nuisance task such as heavy breathing. The results of these analyses indicate that it is worthwhile to include motion covariate regression with the TOAST correction for complex-valued analysis preprocessing. However, the nuisance regression alone is not sufficient and is greatly outperformed by TOAST. Correction with both methods greatly increases the strength of detected activity and greatly improves the distribution and temporal independence of the noise. These results further indicate that complex-valued analysis is not feasible, at least not reliably, in the uncorrected data. This is true even in the more typical fMRI dataset with no nuisance task.

3.1 Introduction

The state of the spin system and the magnetic environment in MRI have unique effects on the magnitude and phase portions of the complex-valued reconstructed image. Accordingly, in a functional MRI (fMRI) time series, each signal component may contain different information pertaining to the changing system and environment encoded in its temporal response, which can then be used to infer certain physiology and/or physiologic function. Analysis of only the magnitude is standard in traditional Blood Oxygenation Level Dependent (BOLD) [35, 54] fMRI, but the potential value of the phase signal for the study of brain function and physiology may be substantial.

For example, the hemodynamic phase response can provide useful information in BOLD fMRI. The phase offset caused by a change in blood oxygenation, flow and/or volume is dependent on the vascular morphology [2, 61] much more so than is the magnitude. The theory presented suggests that voxels containing relatively small, randomly oriented vessels will show little phase change as opposed to voxels with larger, more coherently oriented vessels where significant phase change is expected. This distinction could be used to distinguish voxels more likely to contain cortical neurons from a delocalized area containing either penetrating or pial veins draining the active cortex [2, 44, 62]. Recent findings indicate, however, that hemodynamic phase response occurs in areas of microvasculature as well, suggesting a bulk magnetization effect leading to a net phase change [63]. While this could confound identification of large vessels, it also presents an opportunity to use this response to further the understanding of hemodynamic biophysics.

Phase may be even more useful in neuronal current MRI (ncMRI) for the direct detection of action potentials [10]. The induced magnetic field expected from such an event is small, but potentially large enough to noticeably disturb the system and be detected. Simulations have shown that a larger phase than magnitude effect is expected in ncMRI [16], and phantom studies have come to similar conclusion [64, 65]. Although an *in vitro* experiment showed promising results suggesting a detectable ncMRI signal [12], at this point no robust or undeniable detections have been reported *in vivo* [11, 66].

The lack of complex-valued BOLD fMRI used in practice and the lack of firm success or failure with ncMRI can be partially attributed to phase instability, which has been recently investigated by Hagberg et al. [67]. Their results indicate that the presence of physiological noise tends to be more detrimental to phase than magnitude in terms of temporal standard deviation of phase (tSD_{Φ}) and magnitude temporal signal-to-noise ratio ($tSNR$). Although physiologic noise is certainly detrimental in both magnitude and phase, the particularly sensitive nature of the phase to these phenomena often renders it of little use in statistical analysis.

Using the sensitivity of the phase robustly and repeatably as an investigative tool requires improved signal quality through reduction of the effects of noise described above. This ideal signal would consist of the smallest independently and identically distributed white Gaussian noise, as well as the largest evoked signal response possible. Any other structured signal confounds detection of the desired response unless properly modeled. Identifying the ideal pulse sequence parameters and using multiple receiver coils can help minimize noise and maximize response, while applying post-acquisition modeling techniques can either provide direct stabilization or attempt to compensate for nuisance signals. A recently developed dynamic magnetic field map estimation and correction post-process [68] appears capable of compensating for or removing signal likely caused by larger spatial scale temporal fluctuations in magnetic field. This was shown to significantly reduce phase variance and magnitude signal correlated with the field dynamics. By restricting the spatial variability of the estimated field, spatially local changes remain unaffected, only removing dynamics on larger spatial scales.

Appropriate statistical modeling is also important for detection of functional response. A line of research involving complex-valued regression models has been described in the literature [19, 43, 55, 69, 70, 71, 72, 73], and each is appropriate in certain situations. In general, these models fall into two separate categories: the magnitude and phase signals are either uncoupled, as in the case of Lai and Glover [69] as well as in Lee et al. [70], or coupled appropriately as in Nan and Nowak [71], Rowe and Logan [43, 55], and Rowe [19, 73]. These models are only appropriate whenever the phase data represents relevant information, i.e. is dependent on the state of an input of interest. Examples of situations where phase has a relavent response are discussed above, and results will be presented below supporting a relationship between the phase and task performance. When used appropriately, complex-valued regression models provide the inherent benefit of increasing statistical power simply by using twice as many data values as a scalar alternative [72]. Inappropriate tests with irrelevant phase data will in fact be less powerful than if phase was excluded altogether. The complex-valued model can be designed to detect task related phase changes in addition to task related magnitude changes [19] thereby increasing the possible circumstances under which activation is detected for a given signal-to-noise ratio (SNR) and contrast-to-noise ratio (CNR) [6]. Furthermore, by operating on real and imaginary data, the potential problems with magnitude and phase distributions at low SNR, which approach Raleigh and uniform distributions respectively [43], are avoided. Data analysis was performed with the model from Rowe [19] in this work. It is the most flexible, allowing separate, arbitrary design matrices for the magnitude and phase, however it is also more computationally intensive. This computational complexity can be spared in certain, more restricted situations. It is worth emphasizing that using a complex-valued approach *requires* an expected response reference for both magnitude and phase, and very poorly chosen phase responses can limit its usefulness. When this is the case, it may be appropriate to analyze only the magnitude data [54, 55, 72] using a general linear model (GLM). Analysis of only the phase might also be appropriate, either with the same technique (in the absence of wraparound), or with a more advanced angular regression model [58]. Clearly, the statistical advantages of the joint magnitude and phase complex-valued methods would be sacrificed.

As an alternative to using a GLM for complex-valued statistical analysis, a method for independent component analysis (ICA) of complex-valued data has been provided by Calhoun et al. [21]. Like all ICA techniques, the algorithm does not require regressors a priori like the GLM, but rather generates them from the signal itself under linear independence constraints. This provides certain advantages, most notably that the response to input can be unknown, which is not feasible with a GLM. For the purposes of this work, ICA is not appropriate for this precise reason. The need to include or exclude certain regresssors such as estimated motion parameters led to the choice of a GLM.

The work reported in Hahn et al. [68] presented the framework for the TOAST method and showed its usefulness with regards to phase stabilization and use with the complex constant phase statistical model [43]. The results presented here aim to extend that work in two ways: 1) by evaluating the addition of nuisance regression using estimated motion parameters [74] to the complex-valued post-processing pipeline, and 2) by demonstrating the potential to repeatably provide access to physiologic information embedded in the phase of the complex-valued fMRI signal that may be otherwise practically undetectable, rather than simply the ability to provide phase stabilization. Specifically, the most general complex-valued statistical model of Rowe

[19] is used to show improved detection ability in both magnitude and phase as opposed to simply demonstrating improved detection in magnitude assuming temporally constant phase. This is accomplished by first demonstrating this ability in human experimental fMRI time series. Additionally, the effect of the dynamic field corrections and nuisance regression on the magnitude and phase stability in terms of the variance, autocorrelation and distribution of the residuals after regression is presented. This is followed by similar analysis of simulated fMRI data to provide verification of the experimental results. The reliability shown to be provided by these techniques will hopefully make complex-valued analysis more commonplace, and presents greater opportunity to measure and utilize all the fMRI data acquired to investigate various physiologic processes.

3.2 Materials and Methods

3.2.1 Data Acquisition

All experimental fMRI data was acquired using a GE Signa LX 3T scanner (General Electric, Milwaukee, WI) using the stock quadrature head receiver coil, and functional images were collected with a single-shot echo planar imaging (EPI) pulse sequence. Three separate fMRI experiments were performed, and will be referred to as EXPB, EXPJ, and EXPC. The pulse sequence parameters for each experiment are shown in Table 3.1. The first two experiments were performed during the same scanning session, while the third was collected at a later date with parameters that are more representative of a typical experimental fMRI acquisition.

The human subject was scanned after providing informed consent using a protocol

	EXPB	EXPJ	EXPC
# Slices	9	9	9
Matrix Size	96×96	96×96	64×64
TE (ms)	42.8	42.8	26.0
TR (s)	1.0	1.0	1.0
Flip Angle	45°	45°	45°
Bandwidth (kHz)	125	125	125
Echo Spacing (ms)	0.768	0.768	0.680
Field of View (cm)	24	24	24
Slice Thickness (mm)	2.5	2.5	3.8
Repetitions	296	296	180
# Alternating TE's[a]	20	20	0
Functional Task	finger tap	finger tap	finger tap
Nuisance Task[b]	deep breath	jaw motion	none

Table 3.1: Pulse sequence parameters and tasks for each fMRI experiment.

---

[a] odd numbered images have 5 ms longer TE

[b] task performed at 0.167 Hz rate

approved by the Institutional Review Board (IRB). During all the experiments, the subject performed a bilateral finger-tapping task in a block design pattern, and on/off signaling was provided with a visual cue. For experiments EXPB and EXPJ, the block design pattern consisted of 16 blocks of 8 seconds of stimulus and 8 seconds rest, all following a 20 second initial rest, while EXPC had only 10 blocks of 8 seconds of stimulus and 8 seconds rest, all following a 20 second initial rest. EXPB and EXPJ also introduced intentionally sub-optimal conditions to emphasize the types of often occurring phenomena that can confound statistical analysis. This was accomplished using a secondary "nuisance" task, intended to induce an elevated yet reasonable amount of signal instability, performed simultaneously with the finger-tapping task. In EXPB, the same subject was instructed to breath deeply at a 0.167 Hz rate for the duration of the experiment, and a timing reference indicating when to inhale and exhale was provided visually along with the finger-tapping cue. Experiment EXPJ replaced the heavy breathing with periodic jaw movement at the same frequency. Specifically, the subject was given the same timing cue as provided to keep breathing consistent, but with breath in/out replaced by open/close mouth. For experiment EXPC, the subject was asked to perform the stimulus task only, with no nuisance task, and to remain as still as possible otherwise.

It is also important to note that for experiments EXPB and EXPJ, the TE was lengthened by 5 ms on odd numbered repetitions during acquisition of the first 20 repetitions to provide an initial absolute magnetic field map reference, $\Delta\hat{\omega}_0$, to be used as described below. These additional images were discarded before statistical activation analysis. This was not done for EXPC.

The results to follow are focused on analysis of EXPB and EXPJ to provide consistency of sequence parameters and experimental design (other than the nuisance task) across the data from which conclusions may be drawn. However, it is worthwhile to similarly investigate a situation representing more typical fMRI experimental conditions, and this purpose is served by EXPC. The results of this analysis are left for the Discussion section of this document and are thus considered for the purposes of discussion only.

3.2.2 Reconstruction and Dynamic Magnetic Field Correction

All acquired image data were reconstructed offline from raw GE p-files. Data processing required for image reconstruction and correction of magnetic field dynamics was done with a custom program written in C and designed in-house. The process flow involved image generation from k-space by inverse Fourier transform, Nyquist ghost removal [46], estimation of the dynamic field using Temporal Off-resonance Alignment of Single-echo Timeseries (TOAST) [68], and finally correction of the images with the calculated field maps.

The method for estimating the main magnetic field offset at each time point t, $\Delta\hat{\omega}_t$, from time variant portion of the main magnetic field off-resonance, $\delta\hat{\omega}_t$, and an initial absolute reference, $\Delta\hat{\omega}_0$, is described by Hahn et al. [68], and is applicable to single-shot gradient echo EPI (GE-EPI) pulse sequences. The calculation can be written as

$$\Delta\hat{\omega}_t = \frac{\arg\left\{ I_t \sum_{k=1}^{N-1} \frac{I_k^*}{|I_k|} \right\} - \arg\left\{ I_0 \sum_{j=1}^{N-1} \frac{I_j^*}{|I_j|} \right\}}{TE} + \Delta\hat{\omega}_0 \tag{3.1}$$

for a series of N images where I_t is the reconstructed complex-valued image at time t, TE is the echo time, $*$ denotes complex conjugation and the $\arg$ operator returns the phase angle of its argument. It is worth noting that $\Delta\hat{\omega}_0$ is not required to correct the field dynamics, but without it, absolute field correction is not possible and thus registration of the functional data to T_1 weighted anatomical images is not reliable.

The raw field maps were processed to reduce noise, control non-activation related high spatial frequency information captured by the field map and reduce estimation artifacts at the image boundaries before being applied in the correction. This was accomplished by using a locally weighted least squares regression [75]. The first step in this process was to censor voxels to be used in the fitting procedure. A binary mask of voxels above 7% of the maximum voxel magnitude was generated, representing voxels within the brain. Voxels well outside the brain were selected by dilating the original mask by 10 voxels and then inverting it. These voxels had the value of the estimated field (originally only noise) set to zero. This caused the fit of the raw estimated field to fall to zero outside the brain. The voxels not contained within either of these two masks were censored and not used in the fitting procedure.

The next step involved moving voxel by voxel over the entire image and fitting a weighted two-dimensional polynomial using the 20% of all non-censored voxels which are closest (by Euclidean distance) to the current voxel. After selecting the closest 20% of voxels, a tri-cube weight function is used to weight each point according to its distance from the current point. The weight for the j^{th} point, w_j, is found using

$$w_j = \left(1 - \left(\frac{d_j}{d_{max}}\right)^3\right)^3, \tag{3.2}$$

where d_j is the Euclidean distance between the current voxel and the j^{th} voxel and d_{max} is the maximum Euclidean distance between the current voxel and a voxel within the closest 20% of non-censored voxels. The two-dimensional polynomial coefficients were fit using weighted least squares according to

$$P = \left(X^T W X\right)^{-1} X^T W Y \tag{3.3a}$$

$$x_j = \left[1 \; d_{x,j} \; d_{x,j}^2 \; d_{y,j} \; d_{y,j}^2\right]. \tag{3.3b}$$

The j^{th} row of X is x_j, and $d_{x,j}$ and $d_{y,j}$ are the distances from the current voxel in the x-direction and y-direction of the the j^{th} voxel, respectively. W is a diagonal matrix, the j^{th} diagonal element of which is w_j from Eq. 3.2. P is a 5-element vector containing the polynomial coefficients.

Once the coefficients for the fit were computed at a specific point, the value of the processed estimated field at that point was calculated. It should be noted that the estimated value of the voxel of interest is simply the first element of P, because the distance from itself is clearly zero in each direction (i.e. designed to be located at position $x = y = 0$).

Once this processing has been carried out, the field maps were applied using the one-dimensional (phase-encoding direction) Simulated Phase Rewinding (SPHERE) [53] correction method to remove their effects from the original images.

As a final processing step, the angular mean [58] of each voxel time series following the dynamic field correction was subtracted out to prevent phase wrapping within the imaged object. No voxels inside the object drifted more than 2π radians over the length of the experiment, especially after being corrected for the field dynamics, and zeroing the mean was sufficient in all cases to prevent wraparound in voxels within the head.

3.2.3 Simulation

Simulations were performed to supplement and verify the results obtained from the human fMRI experiments described above. The simulator is designed to emulate the acquisition of k-space as would occur in an actual scan session. Generation of a single image (slice) requires two conceptually separate configuration specifications. First, certain properties of both the object to be "scanned" and the magnetic environment within the space occupied by the object must be provided. These include 2-dimensional spatial maps of spin density, $\rho(x, y)$, tissue transverse relaxation $T_2^*(x, y)$, and the magnetic field offset from resonance (resonance defined as 3.0 T), $\Delta B(x, y)$. The second configuration concerns the scanning parameters for the k-space acquisition itself (limited to GE-EPI), which include echo time, field of view, image matrix size and sampling bandwidth. These parameters provide the necessary information for the simulator to create x and y gradient waveforms (150 mT/m/s peak slew rate, 40 mT/m peak amplitude), G_x and G_y, emulating those which would be generated by an actual scanner given the specified input. Finally, sampling times, $m_{(k_x,k_y)}\Delta t$, are associated with each sampled k-space point and the "acquired" signal for the j^{th} image in a time series, S_j, is produced according to

$$S_j(m\Delta t) = \sum_{q=\frac{-N_x}{2}}^{\frac{N_x}{2}-1} \sum_{r=\frac{-N_y}{2}}^{\frac{N_y}{2}-1} \Bigg\{ \rho_j(q\Delta x, r\Delta y) e^{\left(\frac{-m\Delta t}{T^*_{2,j}(q\Delta x, r\Delta y)}\right)} \times e^{i\gamma\Delta t\left(\sum_{w=0}^{m}\{G_x(w\Delta t)q\Delta x + G_y(w\Delta t)r\Delta y\} + m\Delta B_j(q\Delta x, r\Delta y)\right)} \Bigg\}. \tag{3.4}$$

In the above equation, Δx and Δy are the spatial dimensions represented by a single point in the $N_x \times N_y$ point input parameter maps ρ, T_2^*, and ΔB. The simulations presented in this work used $\Delta x = \Delta y = 468.75\ \mu$m and $N_x = N_y = 512$. Note that these do not represent the spatial resolution and matrix size of the images *reconstructed* from the simulated data. Images were reconstructed at much lower resolution and matrix size (matching the of acquired data with 96 × 96 matrix size and 2.5 mm isotropic voxels). The higher resolution of the input parameter maps simply provides a more accurate simulation of the sub-voxel effects of motion and magnetic field gradients. The variable Δt represents the timing resolution of the gradient waveforms (*not* the sampling rate). The value of Δt can be any divisor of the sample rate, and the smaller its value, the closer the gradient sum over m

approximates the continuous integral over time $m\Delta t$ (0.1 μs used here).

Three separate series of 296 ($0 \leq j < 296$) single-slice images were simulated containing areas of locally induced temporal signal change designed to mimic a functional response, and will be referred to as SIMB, SIMJ and SIMC. The SIMB and SIMJ series were created using a temporally variant ΔB field and simulated motion in an attempt to emulate similar effects in EXPB and EXPJ, while the SIMC series contained neither and is intended to serve as a control.

The $\rho(x, y)$ parameter map, shown in Figure 3.1a, was the same for all three series, and was created using a slice from the reconstructed images from EXPB after it had been corrected for magnetic field inhomegeneity. The magnitude of the original image was sinc interpolated to dimensions of 512×512, and then masked to zero everywhere outside of the brain. The simulated functional responses, also identical in each, were induced by increasing the value of T_2^* and either increasing or decreasing the value of ΔB during task to elicit magnitude and phase changes, respectively. The variations were applied in a block design pattern identical to that used for the finger-tapping task in EXPB and EXPJ. The map of ρ and the locations containing these local variations are shown in Figure 3.1b, and each active area is a 13×13 square, measuring 6.1 mm on a side. The values of T_2^* and the portion of ΔB associated with local activity at each location are shown for task "off" and task "on" periods in Table 3.2. During task "off" periods and everywhere outside of the active locations, T_2^* is equal to 35 ms and the local ΔB equal 0.

The SIMB and SIMJ series were generated with simulated bulk motion, as previously mentioned. The amount of motion to apply was determined directly from the

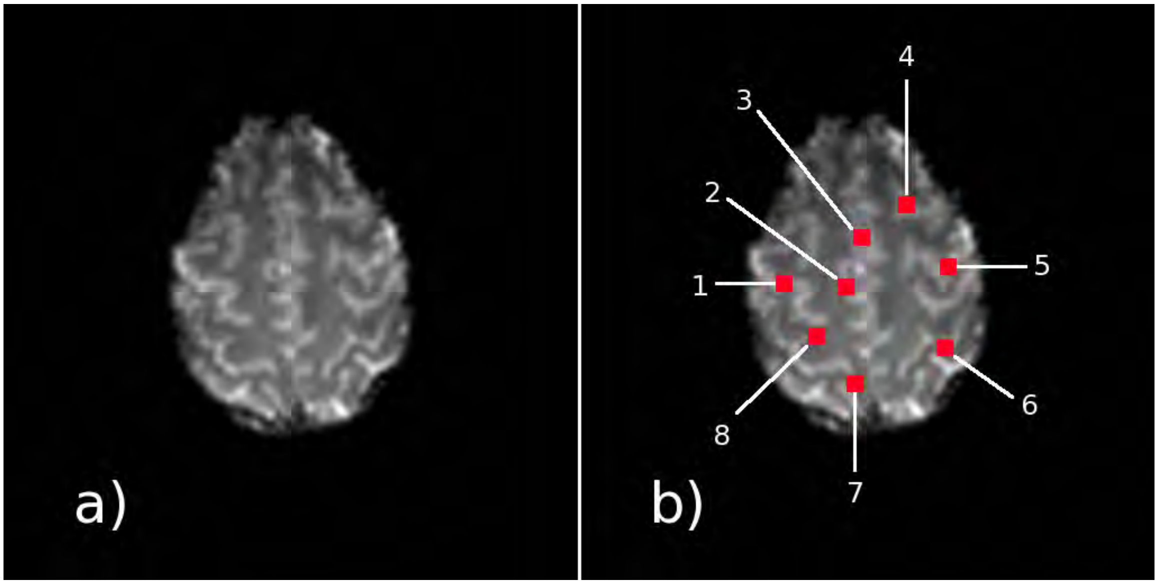

Figure 3.1: The ρ map used as input to the simulation (a). The same map is shown in (b), overlaid by the locations where activation was simulated in either magnitude, phase or both. The type and size of the simulated activity can be found for each numbered location in Table 3.2.

estimations of the motion made with the AFNI [29] plugin 2dImReg from EXPB for SIMB, and EXPJ for SIMJ. The simulated motion was implemented by shifting and rotating the ρ, T_2^*, and local activation related ΔB maps, discussed above, by the appropriate amount at each time point, j, before applying Equation 3.4.

In addition to the ΔB map for inducing phase activation related response, each simulated image series contained an additional magnetic field offset representing bulk field inhomogeneity. In SIMC, a temporally static field was applied, and it was generated using the static field ($\Delta\hat{\omega}_0$) estimated for EXPB following interpolation to dimensions of 512×512, similarly to the ρ map. SIMB and SIMJ were generated using the sum of the same map used for SIMC and the series of dynamic reference field maps ($\delta\hat{\omega}_t$ from Hahn et al. [68]) estimated for EXPB and EXPJ, respectively, also interpolated to 512×512. It should be noted that this portion of the ΔB was not included in the motion simulation process because it was assumed that it already contained the changes which occurred due to any motion that occurred. The full ΔB map that was finally applied in Equation 3.4 was the sum of this bulk field inhomogeneity map and the local activation field map (after having motion applied, if applicable).

A static magnetic field offset was applied to all three series as well. This field was simply the static field estimation from EXPB (nearly identical to that in EXPJ) following interpolation to dimensions of 512×512, similarly to the $\rho(x, y)$ map. The additional temporally dynamic fields used for SIMB and SIMJ were generated directly from those estimated in EXPB and EXPJ, respectively, again interpolated to a 512×512 matrix.

Location:	1	2	3	4	5	6	7	8
T_2^* (ms), Task “off”	35.0	35.0	35.0	35.0	35.0	35.0	35.0	35.0
T_2^* (ms), Task “on”	35.35	35.7	35.0	35.35	35.7	36.05	35.35	36.05
ΔB (nT), Task “off”	0.0	0.0	0.0	0.0	0.0	0.0	0.0	0.0
ΔB (nT), Task “on’	2.83	-4.25	2.83	0.0	1.42	-2.83	4.25	1.42

Table 3.2: Local values of T_2^* and ΔB during both task “off” and task “on” periods at locations 1 through 8. The area to which each refers is shown in Figure 3.1b.

Besides the already specified parameters, each series was simulated with identical scan parameters to EXPB and EXPJ above, with the exception of the echo spacing, which was 759 μs in the simulation. This includes the images with extended echo time during the initial 20 repetitions. The difference in echo spacing from that in the actual experimental data (768 μs) was due to roundoff errors in the calculation method of the simulated gradients. This small 9 μs difference should not be of any consequence.

Finally, once all three of the simulated image series were generated, each was duplicated 100 times and independently and identically distributed Gaussian random noise was added to the real and imaginary channels of the k-space samples. The variance of the added noise, equal to 10, was scaled such that the signal-to-noise ratio (SNR) of the reconstructed images was similar to that in EXPB and EXPJ, which was approximately 20 within the brain. Each image series was then processed in an identical manner to the human results.

3.2.4 Statistical Modeling and Analysis

The complex-valued generalized likelihood ratio detection model used is described in detail in Rowe [19], but will be summarized for clarity. The general form of the complex-valued multiple regression model, assuming a series of n complex-valued images and using notation similar to the original work is

$$y_t = [\rho_t \cos\theta_t + \eta_{Rt}] + \imath\,[\rho_t \sin\theta_t + \eta_{It}] \tag{3.5a}$$

$$r_t = \sqrt{y_{Rt}^2 + y_{It}^2}\,, \qquad \phi_t = \arctan\left(\frac{y_{It}}{y_{Rt}}\right) \tag{3.5b}$$

$$\rho = \mathbf{X}\boldsymbol{\beta}, \qquad \boldsymbol{\theta} = \mathbf{U}\boldsymbol{\gamma} \tag{3.5c}$$

where $(\eta_{Rt}, \eta_{It})' \sim \mathcal{N}(0, \Sigma), \Sigma = \sigma^2 I_2, \rho_t$ and θ_t are the *true* magnitude and phase elements of ρ and $\boldsymbol{\theta}$ at time t, and y_t is the *observed* complex-valued signal at time t, also represented as magnitude, r_t, and phase, ϕ_t. Additionally, assuming that s slices are acquired and each image has dimensions $h \times w$, $\boldsymbol{r}$ and $\boldsymbol{\phi}$ are $n \times (hws)$ matrices containing the magnitude (former) and phase (latter) measurements from an individual voxel in each column. The $n \times (q_1 + 1)$ matrix $\mathbf{X}$ and the $n \times (q_2 + 1)$ matrix $\mathbf{U}$ contain q_1 magnitude and q_2 phase regressors (besides a mean regressor) column-wise, and the corresponding coefficients in each voxel fill the columns of the $(q_1 + 1) \times (hws)$ matrix $\boldsymbol{\beta}$ and the $(q_2 + 1) \times (hws)$ matrix $\boldsymbol{\gamma}$.

Four hypothesis conditions are described by Rowe [19] which can be used to formulate a variety of statistical tests on the regression coefficients. The aforementioned hypotheses are $H_a\colon\ \mathbf{C}\boldsymbol{\beta} \neq 0, \mathbf{D}\boldsymbol{\gamma} \neq 0, H_b\colon\ \mathbf{C}\boldsymbol{\beta} = 0, \mathbf{D}\boldsymbol{\gamma} \neq 0, H_c\colon\ \mathbf{C}\boldsymbol{\beta} \neq 0, \mathbf{D}\boldsymbol{\gamma} = 0$, and $H_d\colon\ \mathbf{C}\boldsymbol{\beta} = 0, \mathbf{D}\boldsymbol{\gamma} = 0$, with linear constraint matrices for magnitude, $\mathbf{C}$ $(r_1 \times (q_1 + 1))$, and phase, $\mathbf{D}$ $(r_2 \times (q_2 + 1))$. Using these in proper combination of null and alternative hypotheses makes tests for arbitrary magnitude or phase response either with, without or regardless of a response (also arbitrary) in the other signal component possible, and provides all necessary capabilities for the analysis to follow.

After estimating the regression coefficients under both the null and alternative hypothesis, a χ_r^2 distributed general likelihood ratio test statistic, $-2\log(\lambda)$, can be computed using the variance of the residual error of the least squares fit for the null, $\tilde{\sigma}^2$, and alternative, $\hat{\sigma}^2$, hypotheses as

$$\sigma^2 = \frac{1}{2n}\Big[(\mathbf{r}-\mathbf{X}\boldsymbol{\beta})^T(\mathbf{r}-\mathbf{X}\boldsymbol{\beta}) + 2(\mathbf{r}-\mathbf{r}_*)^T\mathbf{X}\boldsymbol{\beta}\Big] \tag{3.6a}$$

$$-2\log(\lambda) = 2n\log\left(\frac{\tilde{\sigma}^2}{\hat{\sigma}^2}\right). \tag{3.6b}$$

The degrees of freedom, r, in the test statistic is dependent on the specific hypotheses being tested. A comparison of either H_b vs. H_a or H_d vs. H_c gives r equal to r_1, the full row rank of $\mathbf{C}$, while H_c vs. H_a or H_d vs. H_b tests yield r equal to r_2, the full row rank of $\mathbf{D}$. If comparing the H_d and H_a hypotheses, the test statistic has $r_1 + r_2$ degrees of freedom.

The stimulus reference function, $f_{stim}(t)$, was modeled here by a function that is simply -1 during task off periods and 1 during task on periods, shifted by an amount $\delta t_h = 4$ s to account for hemodynamic delay. The shifted boxcar was chosen as opposed to a more elaborate reference curve, for example the boxcar convolved with a gamma function, for the sake of simplicity. The relative accuracy of a boxcar and an alternative model function is impossible to determine and will vary with location, thus providing little motivation to change. Unless otherwise stated, the design matrices $\mathbf{X}$ and $\mathbf{U}$ were the same, with a column of 1's (mean regressor), a column with a linear ramp from -1 to 1 (linear trend regressor), and a column containing $f_{stim}(t - \delta t_h)$, effectively treated as the response model in this case. The test contrast matrices $\mathbf{C}$ and $\mathbf{D}$ have a single row of 0's with a single 1 in the column of $\mathbf{X}$ or $\mathbf{U}$, respectively, containing $f_{stim}(t - \delta t_h)$ ($\mathbf{C} = \mathbf{D}$).

Regression analysis of both magnitude-only and phase-only data were also used for the purposes of comparison, both of which are special cases of the model described above. To test the magnitude-only hypothesis, $\mathbf{X}$ remains as described above and the phase is left unconstrained under both null and alternative hypotheses (H_b vs. H_a), with $\mathbf{U}$ equal to an $n \times n$ identity matrix, $\mathbf{I}_n$ (The constraint matrix $\mathbf{D}$ is not used in the computation because phase is unconstrained under H_b and H_a). Similarly, allowing unconstrained magnitude under both hypotheses (H_c vs. H_a) with $\mathbf{X}$ equal to $\mathbf{I}_n$ performs a test of the phase-only with $\mathbf{U}$ unchanged (the constraint matrix $\mathbf{C}$ is unused in this case).

3.3 Results

3.3.1 Human

Regression analysis using the complex-valued model was performed on both fMRI time series after correction of only a static magnetic field inhomogeneity using $\Delta\omega_0$, as well as dynamic magnetic field errors using $\Delta\omega_t$. Estimates of the motion in two axes of translation and one of rotation were made using the AFNI plugin 2dImReg, also before and after each type of field correction. Motion compensation, when used, was applied by including the temporal motion estimates as additional regressors in the design matrices $\mathbf{X}$ and $\mathbf{U}$. Specifically, motion estimates made before applying field correction were used as regressors in $\mathbf{X}$ and $\mathbf{U}$ when computing activation in the time series of images that was not corrected for temporal magnetic field variations (motion correction only case). On the other hand, estimates of motion made after field correction were used to compute activation in the images that were corrected for temporal magnetic field variations (motion and field correction case). The series of images were *not* shifted or rotated at all using the motion estimates at all. The motivation for this analysis method will be discussed in the Discussion section to follow. The term motion correction or motion compensation will be used in the remainder of this analysis to refer to the inclusion of the motion estimates as additional regressors as described here and not as rigid body rotation and translation. This process yields the results of 4 processing types: none, motion compensation only, dynamic field correction only, and dynamic field correction and motion compensation. Static magnetic field correction is implied in the all four types.

Maps of $-\log_{10} p$ where p is the p-value associated with the χ^2 test statistic at a $p < 5 \times 10^{-4}$ unadjusted threshold in a single slice from EXPB and EXPJ after each combination of processing steps are shown for tests of the magnitude-only, phase-only and magnitude-and-or-phase in Figure 3.2. The anatomic underlay in each of these figures, and in the figures to follow, is the first image in the functional EPI time series. The hypotheses for the test of magnitude-and-or-phase are $H_{null} : \mathbf{C}\boldsymbol{\beta} = 0, \mathbf{D}\boldsymbol{\gamma} = 0, vs.\ H_{alt} : \mathbf{C}\boldsymbol{\beta} \neq 0, \mathbf{D}\boldsymbol{\gamma} \neq 0$, and all other parameters for each test are described in the Methods section of this document.

The different post-processes appear to have only a slight impact on the magnitude-only activation detection, as evident from Figures 3.2a and b, which show a single slice from EXPB and EXPJ with the processing combinations along the columns. This is not unexpected, and is in agreement with previous results reported by Hahn et al. [68], which analyzed the effect of the dynamic field correction and motion on the magnitude signal component and magnitude-only activations in some detail. This is especially true of the results of EXPB (Figure 3.2a), which involves the heavy breathing nuisance task and shows very little difference between the four different processing cases. The results of EXPJ (Figure 3.2b) show somewhat more significant differences, especially in the cases including motion compensation. Including motion correction appears to reduce the amount of detected activity, although there are a few areas where activity may be increased with its inclusion.

The phase-only activations clearly show that the different post-processing steps affect the detection of activation response in the phase signal (Figures 3.2c and d). In both experiments, the number of active voxels and their relative significance is elevated following any post-processing compared to none at all, with the exception of using motion compensation alone in EXPJ. This is significant in that the applied corrections not only stabilize the phase signal by removing spatially global variation, as was demonstrated by Hahn et al. [68], but additionally preserve spatially local variations and increase the detection power of task related signal of potential interest. In EXPB, results indicate that TOAST correction alone appears to allow for better activity detection than only motion compensation, however it is difficult to discern whether the application of both provides additional improvement or not due to the relative similarity between the activated regions when using the field only and when using both the field and motion in the correction.

The analysis of EXPJ (Figure 3.2d) indicates similar benefit from using only the

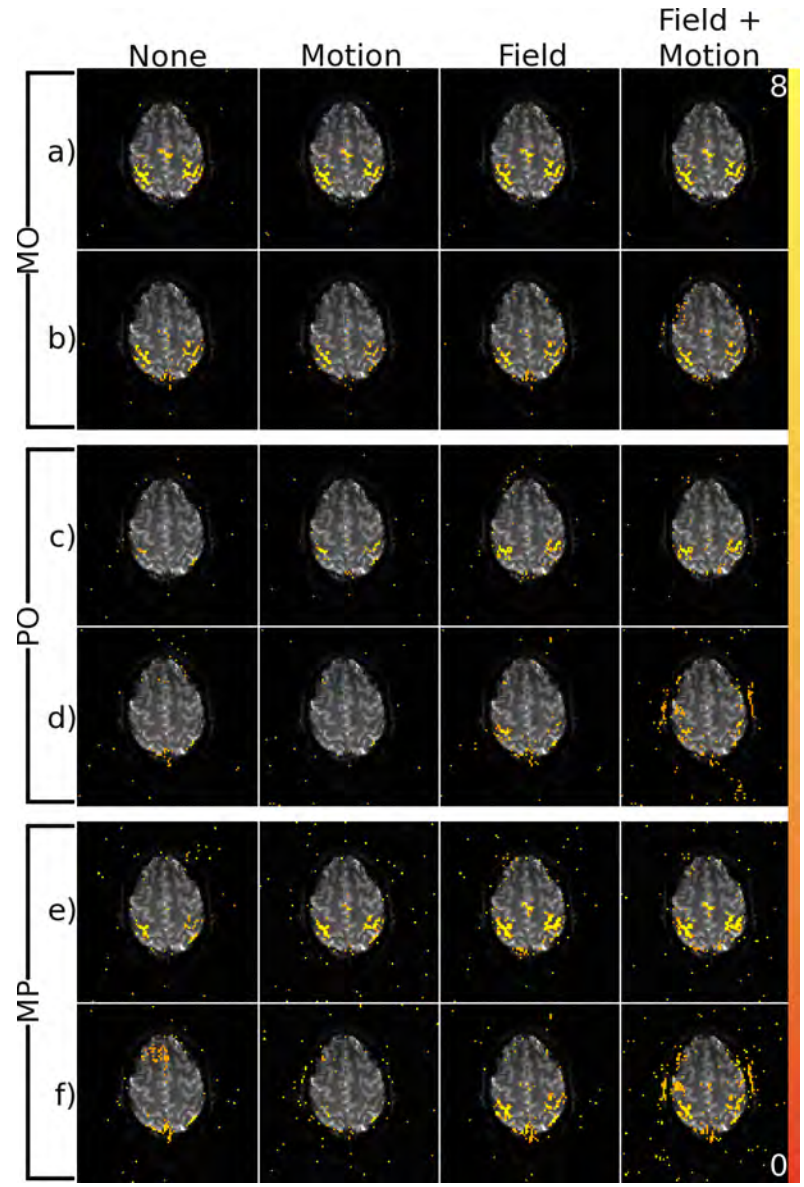

Figure 3.2: Maps of $-\log_{10} p$ where p is the p-value associated with the χ^2 statistics for magnitude-only (a,b), phase-only (c,d) and magnitude-and-or-phase (e,f) activation. The results of EXPB (a,c,e) and EXPJ (b,d,f) are shown for each activation model. From left to right, columns show results after no post-processing, motion compensation only, dynamic field correction only and both motion and field correction. Active voxels shown above a threshold of $p < 5 \times 10^{-4}$ (unadjusted).

field correction as in EXPB, but performing motion compensation in this case yields somewhat different results. As previously mentioned, motion correction alone has very little effect on the phase-only activity. However, when applied in conjunction with TOAST, an activation pattern results which is different in certain respects from what is shown using just TOAST. Specifically, when both corrections are applied significant activity is detected in the skull region on both the left and right sides and some additional activity is detected within the brain as well on the left side. The uniqueness and questionable anatomical relevance of this detected activity with respect to the finger-tapping functional task suggests that it is of an artifactual nature. This artifact may be related to the jaw motion occurring during acquisition, due to its location above the jaw bone, and the affect of this motion on the main magnetic field [27]. Detection of false positive activity has been described by Soltysik and Hyde [76] in the presence of similar jaw motion associated with chewing. In that case, however, the jaw motion was directly related to the task of interest, opposed to this case where the functional task and jaw motion occur at different frequencies. However, an additional factor could potentially be instability of the motion compensation regression model resulting from multicollinearity of the design matrix columns which include motion parameters.

The degree of multicollinearity in the independent variables of the linear model including the motion estimates in EXPJ was evaluated by using the condition number of the $\mathbf{X}'\mathbf{X}$ matrix. This value is defined as the square root of the ratio of its largest to smallest singular values, and provides information about the linear independence of the matrix's columns. An orthogonal matrix has a condition number of one, and a matrix containing one or more columns which are a perfect linear combination of the other columns has a condition number of infinity. The condition number without including motion parameters is 3.46, while including motion yields a condition number of 30.33 and 23.02. The literature states that a condition number of 10 represents the low end of where collinearity starts to affect the solution, while a condition number of 100 indicates serious effects of collinearity [77]. The model including motion is well into this range, thus multicollinearity may be causing instability.

The results provided in Figures 3.2e and f present little surprise given the magnitude-only and phase-only activations in Figures 3.2a-d. However, it is apparent that the activated locations are understandably not simply a combination of the magnitude-only and phase-only activations. The differences arise from the fact that the uncertainty of the overall fit in this case involves a combination of the uncertainty in both the magnitude and phase [78]. Intuitively, in the unprocessed data, the large phase variations cause increased uncertainty nearly uniformly, resulting in a loss of significance where activations in the magnitude were previously apparent. This “grouped” variation can become beneficial, however, if both magnitude and phase are properly modeled. In this case, the overall variation of both magnitude and phase is less than either alone, due to the increased number of data values, thus leading to significant detection of response which otherwise is too small. As a result, the magnitude-and-or-phase activations can be a superset of the magnitude-only and phase-only activations, and have greater significance where overlap occurs.

One notable characteristic of these results is the apparent difference between the activity detected in EXPB and EXPJ, given that the only difference between the two is the type of nuisance task being performed. Specifically, the size and significance of the activation seems greater in EXPB in both magnitude and phase even after full correction. The most likely reason for this are differences in the amount and type of motion present during each experiment. First, maintaining head position when opening and closing the mouth is a greater challenge than doing so during heavy breathing, and this was represented in the computed motion parameters in all 3 axes. The variance of the displacement in EXPB (for repetitions 31 through 296, the same set used for regression analysis) was 2.35×10^{-3} mm left-to-right, 5.30×10^{-3} mm anterior-to-posterior, and 9.36×10^{-3} degrees rotation around the inferior-superior axis, compared to 9.36×10^{-3} mm, 8.12×10^{-3} mm and 2.51×10^{-2} degrees in EXPJ, each of which is significantly larger than the corresponding variance in EXPB when using an F-test ($p < .001$). Besides containing greater amounts of bulk motion, the close proximity of the jaw motion in EXPJ to the imaging plane results in variable sub-voxel field gradients and thus variable signal dropout. This is not correctable using TOAST and is not necessarily associated with bulk motion, although there is likely a correlation between the two. Regardless, this phenomenon almost certainly decreases sensitivity of activation detection.

The data presented so far indicates that statistical tests for the presence of a task related signal component in the magnitude, phase or both has significantly more power after being processed. It is somewhat apparent by comparison of the statistics in Figures 3.2a and 3.2b with those in and 3.2c and 3.2d that there is a different pattern of activation in magnitude and phase, and thus potentially different physiologic information. However, the complex-valued regression more appropriately models

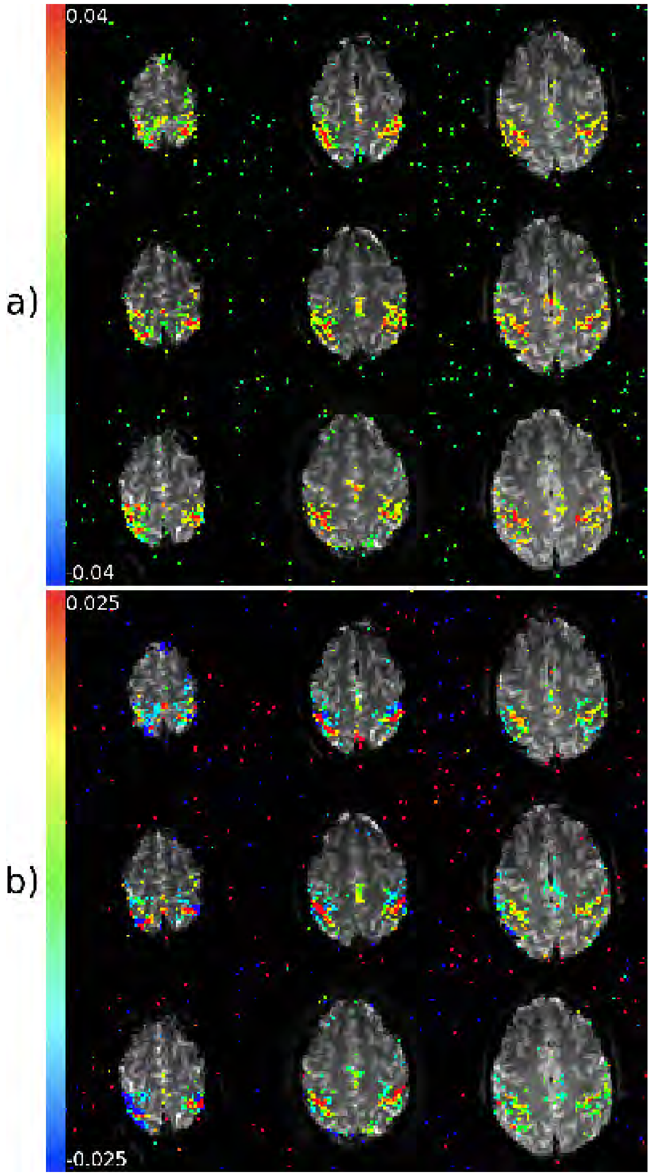

Figure 3.3: All slices from EXPB after dynamic field and motion correction are shown with overlays of β_{ref} (a) and γ_{ref} (b), calculated from the complex-valued regression test. The coefficients are shown where the χ^2 of the overall test was significant with $p < 5 \times 10^{-4}$ (unadjusted). β_{ref} and γ_{ref} are the estimated coefficients of the stimulus response reference function in the magnitude and phase, respectively, and are shown to be very different.

the two components in tandem, as described by Rowe [19] as well as the Statistical Modeling and Analysis section of this document, and thus presents a better representation of the joint magnitude and phase response through more accurate coefficient estimates. The individual response characteristics of the magnitude and phase, in addition to the relationship between them, can be visualized with more clarity in Figure 3.3. Here, all slices from the fully post-processed experiment EXPB data set are shown with overlay maps of β_{ref} (Figure 3.3a) and γ_{ref} (Figure 3.3b), the coefficients of the task reference regressor in the magnitude and phase, respectively. These coefficients are shown only where the overall test (χ^2) was significant to $p < 5 \times 10^{-4}$ (unadjusted). Using this display method, locations with only magnitude activation are located where the phase coefficients displayed are nearly 0, and vice versa for locations with only phase activation. The fact that each contains unique information is apparent, and the most notable pattern seems to be the increasing strength of the phase response in the superior direction. Thorough and conclusive interpretation of these results is not the focus of this work, and this information is provided here as further evidence that such results are accessible and potentially meaningful.

To supplement the regression analysis, time series modeling of the real and imaginary regression residuals was performed to determine both the initial characteristics of voxel time series and the temporal stabilizing effects of the dynamic field mapping and nuisance signal regression. In an ideal situation, as assumed by the linear regression model, residual errors in the real and imaginary channels are temporally independent and normally distributed. The degree to which these assumptions are violated influences the interpretation of the significance of the test statistic and coefficient estimators [79].

Voxel-wise tests for temporal independence of both real and imaginary residuals of the complex-valued regression after the different post-processing steps is displayed for a single slice (the same slice as used for previous analysis) from each experiment in Figure 3.4. These figures show maps of $-\log_{10} p$, where p is the p-value associated with the the χ^2 statistic of a Breusch-Godfrey test [80, 81] for the presence of autocorrelations at a time lag of 1, with voxels shown as significant above a threshold of $p < .001$ (unadjusted). The Breusch-Godfrey test is used instead of the Durbin-Watson test [82], which is the test used by Lou and Nichols [79], because of its insensitivity to deviations from normality of the samples. Results of these tests indicate that the presence of motion and a temporally dynamic magnetic field offset both influence the temporal independence of the residuals to varying degrees, which is an expected result. This is evident from the fact that neither the field nor motion correction alone are generally sufficient for removing the sample autocorrelation, while application of both consistently provides the minimum autocorrelation. It is worth noting that in the data from EXPJ remains significantly autocorrelated in part of the area above the jaw, even after full correction.

Voxel-wise analysis of the normality of the real and imaginary residuals from the complex-valued regression after the different post-processing steps is displayed in Figure 3.5. Specifically shown are the results of an Anderson-Darling test [83] in EXPB and EXPJ, which tests for deviations in the error from a normal distribution. In these images, voxels colored red represent those which reject the null hypothesis that the residuals belong to a normal distribution with probability $p < .01$. The

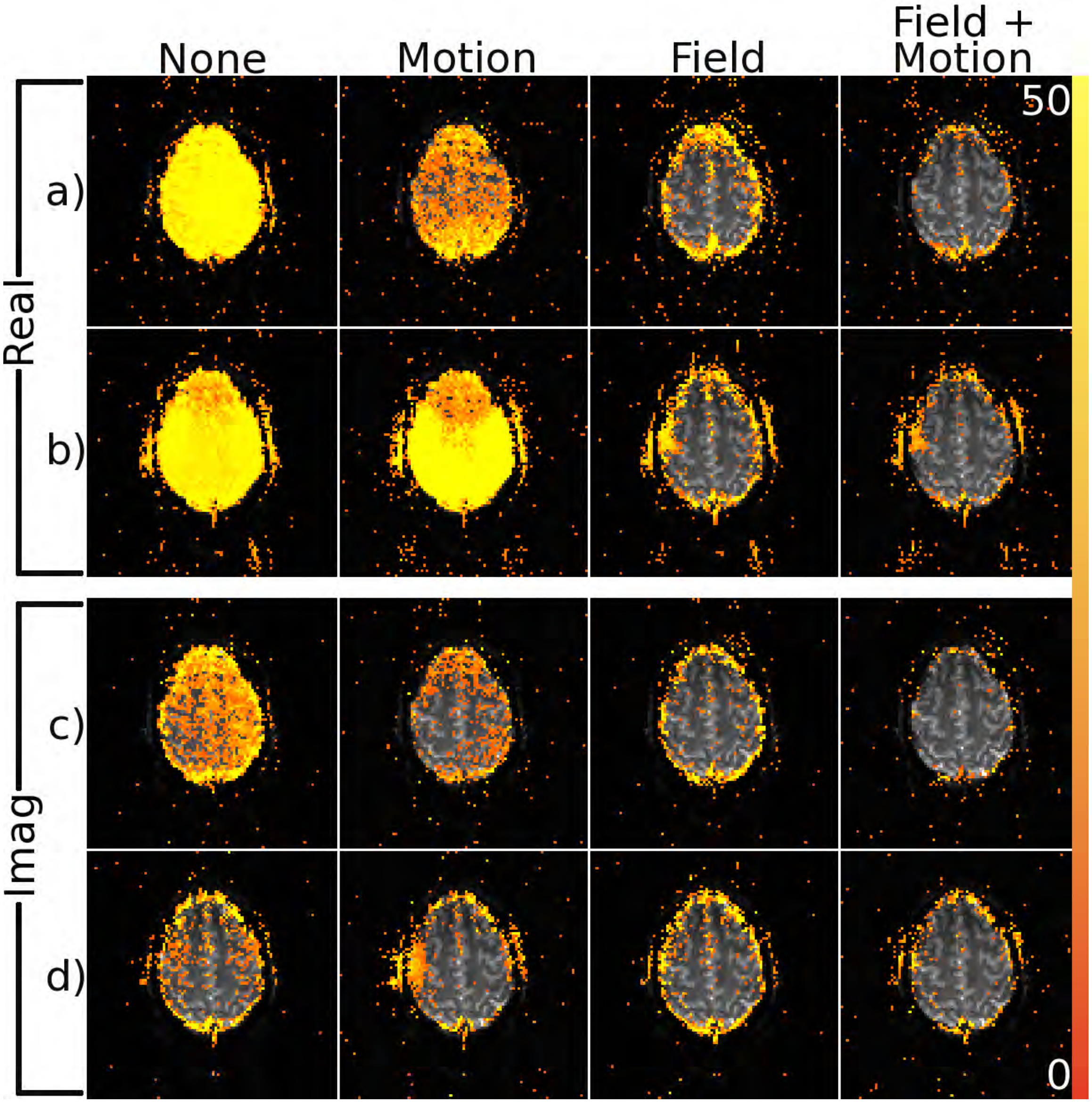

Figure 3.4: Maps of the χ^2 statistics resulting from voxel-wise Breusch-Godfrey tests for autocorrelations in the real (a,b) and imaginary (c,d) residuals of complex-valued regression at a lag of 1 after different post-processing steps. Significant voxels shown above a threshold of $p < .001$ (unadjusted). Results are shown for both EXPB (a,c) and EXPJ (b,d). Full correction results in the least amount of significant residual autocorrelation.

Anderson-Darling test is used because it has been shown to be one of the most powerful tests for deviations from normality [84], and is on par with the Shapiro-Wilk test [85], which is the test employed by Lou and Nichols [79]. Similar to the autocorrelations, it seems that application of both motion compensation and dynamic field correction provide the most desirable signal characteristics. However, in this case, either motion correction or field correction alone seem to provide nearly the same performance as the two combined, except in the case of the imaginary residuals from EXPJ. In that case, deviations from normality were the most severe, and the relative normality in the other cases may be the reason either correction alone performs as well as both together.

In EXPJ, there are a few areas which contain significantly autocorrelated and to a lesser extent non-normal residuals even after full correction. The greatest example of this can be seen in the real autocorrelations in Figure 3.4c. The failure to completely restore temporal independence and normality is likely two-fold. First, The spatial variation in the field is very large in these areas and may not be fully captured by the model, thus leaving it partially uncorrected. Additionally, because of these large spatial variations significant intra-voxel effects are likely to be present and this is not correctable with the TOAST method and is likely unrelated to bulk motion. It is interesting to note that the areas previously mentioned which become active in EXPJ in the test of magnitude-and-or-phase after applying both corrections (Figure 3.2f) coincide with locations where the autocorrelations and departures from normality are not fully removed. This combined with the relatively poor conditioning of the design matrix could explain why these areas become active in this case.

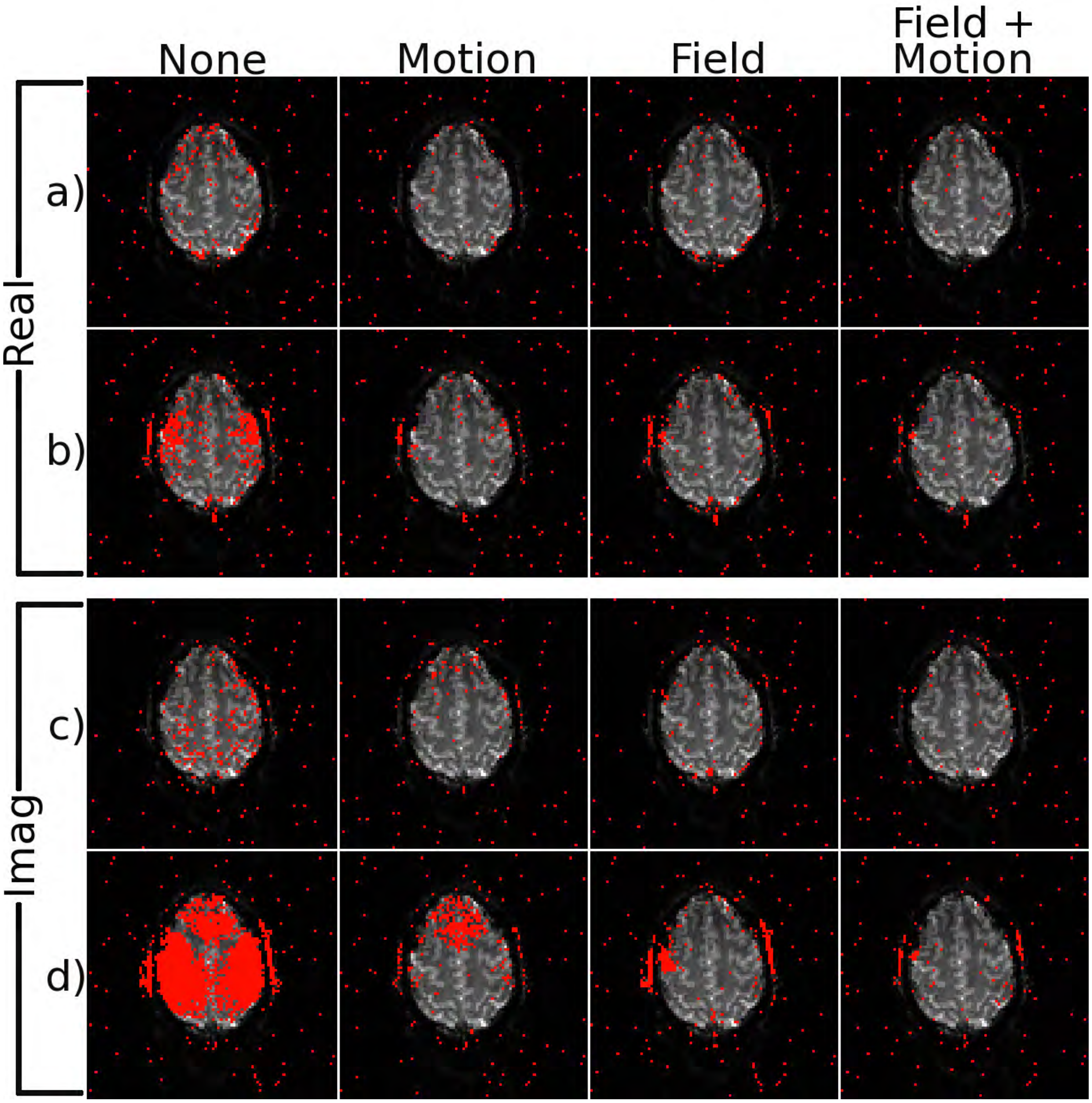

Figure 3.5: Maps of the results from voxel-wise Anderson-Darling tests for deviations from normality in the distributions of the real (a,b) and imaginary (c,d) residuals of complex-valued regression after different post-processing steps. Voxels colored red are those in which the null hypothesis is rejected with probability $p < .01$ (unadjusted). Results are shown for both EXPB (a,c) and EXPJ (b,d). Full correction results in the least amount of significant deviation from normality.

3.3.2 Simulation

Each of the 100 iterations of the simulated experiments SIMB and SIMJ were analyzed in exactly the same fashion as the human experiments, EXPB and EXPJ. The SIMC iterations were only processed corresponding to the "none" case of the human experiments as no dynamic field offset nor motion was present. The results were analyzed by quantifying the detection power, which is defined as the number of iterations out of 100 in which a test statistic was significant at a specified threshold. For each set of tests, the threshold for each individual test matched that used in the human data analysis. Only voxels meeting this threshold in at least 5 of the 100 tests are shown in the images, masking away the others. This choice of thresholding was used to provide optimal comparability with the human results. Each of the images resulting from simulation represent voxels where the true mean of the distribution is shifted such that at least 5% of its area lies over the percentage corresponding to the specific single test threshold of the area under the null distribution curve. This way, the probability that an unmasked voxel would be significant in a single trial at its single trial threshold is the same regardless of that threshold.

The results of magnitude-only, phase-only and magnitude-and-or-phase activation detection are shown in Figure 3.6 for the SIMC series and Figure 3.7 for SIMB and SIMJ. The results shown in Figure 3.7 present characteristics which appear to corroborate what was seen in the human data. First, magnitude-only activity (Figure 3.7a,b) is not drastically different between various post-processing steps, which is similar to the behavior of the experimental data, and it is arguable that the degree of variation in both simulated and acquired data is somewhat similar. Second,

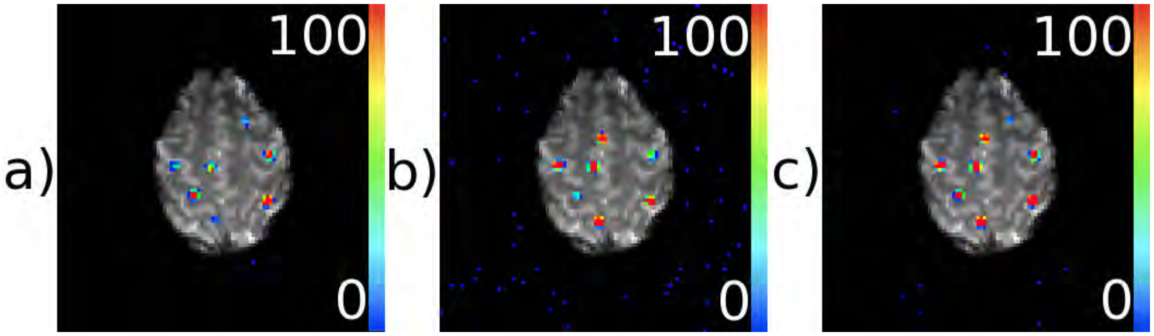

Figure 3.6: Maps of the detection power for magnitude-only (a), phase only (b) and magnitude-and-or-phase (c) in the SIMC simulation. Voxels are shown when detection power is 5% or greater. Detection power is defined as the percentage of iterations a voxel tested significant at $p < 5 \times 10^{-4}$ (unadjusted).

phase-only detection power in SIMB and SIMJ, shown in Figures 3.7c and 3.7d, is significantly reduced without dynamic field correction and reaches power levels near the control with the field correction applied. The relative effect of the motion compensation alone corresponds to some degree with the acquired data, in that a small amount of power is recovered from the unprocessed case. It is of interest to note that the previously mentioned area which becomes active outside of the motor cortex in EXPJ after applying both corrections is not reproduced in SIMJ. This may be caused by the imperfect representation of the exact field changes or motion that occurred, the lack of through plane field gradients in the simulation, or some other signal source present in the experimental data that was not included in the simulation. Finally, the magnitude-and-or-phase power in SIMB and SIMJ (Figures 3.7e,f) show responses to post-processing similar to those observed in experimental data in the majority of cases as well.

It should be noted that the detection power shown for SIMC is not expected to be

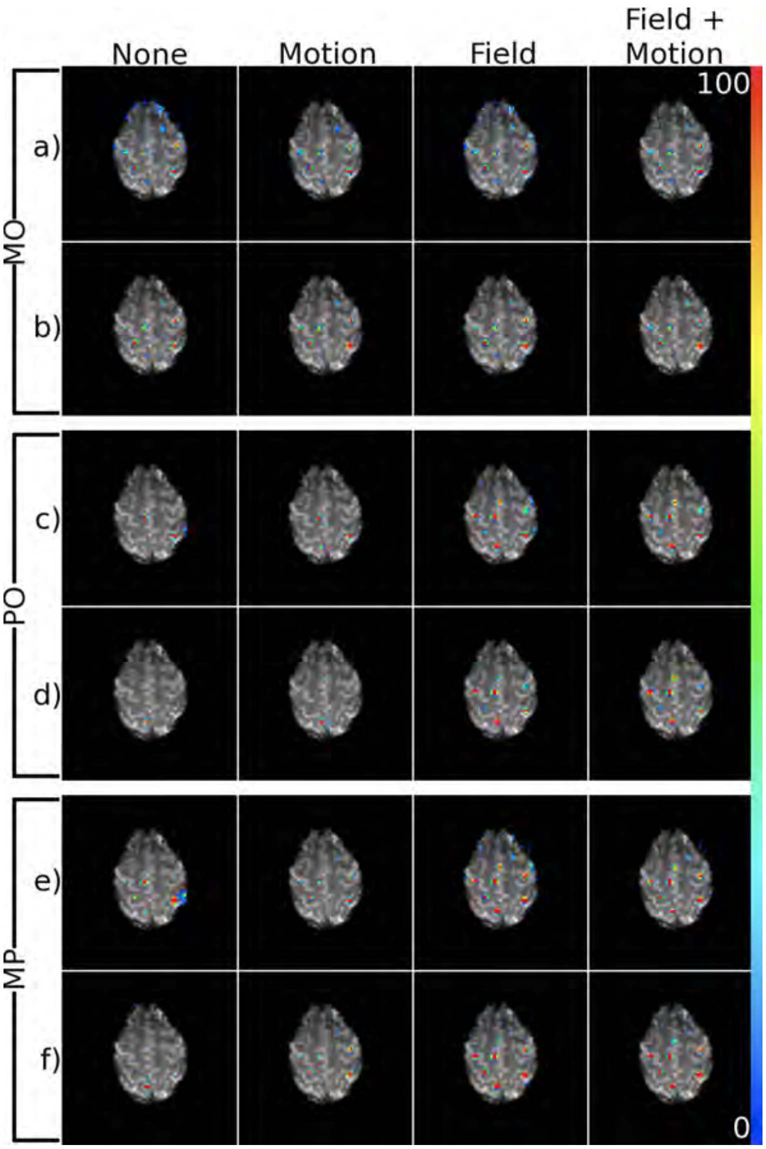

Figure 3.7: Maps of the detection power for magnitude-only (a,b), phase-only (c,d), and magnitude-and-or-phase (e,f) activation. The results of SIMB (a,c,e) and SIMJ (b,d,f) are shown for each activation model. From left to right, columns show results after no post-processing, motion compensation only, dynamic field correction only and both motion and field correction. Voxels are shown when detection power is 5% or greater. Detection power is defined an the percentage of iterations a voxel tested significant at $p < 5 \times 10^{-4}$ (unadjusted).

achievable in either SIMB or SIMJ. The motion applied to both SIMB and SIMJ shifts the active locations around through time, and the motion compensation applied will not account for this. The correction for motion which is applied will simply remove variance in the signal that is correlated with the estimated motion. Achieving the smallest difference between the control and the test cases is still obviously the goal, however.

The temporal autocorrelations and distribution normality of the real and imaginary residuals following complex-valued regression after the different post-processing steps in SIMB and SIMJ were investigated in the same manner as done for EXPB and EXPJ previously. The results of the voxel-wise Breusch-Godfrey test of temporal independence and the Andreson-Darling test of deviations from normality are shown in Figures 3.8 and 3.9, respectively. The same tests for SIMC resulted in no significance for either test beyond the expected type 1 errors, and are not shown here.

The images in Figures 3.8 and 3.9 show that the simulated motion and magnetic field variations cause significant autocorrelation and deviations from normality as seen in experimental data. Additionally, the autocorrelations appear to be more problematic than non-normality in this case as well. The corrections also seem to have a similar impact in the simulated data as they do experimentally. In the autocorrelations, neither motion nor TOAST correction alone generally provide as good a result as the two together. The deviations from normality, when not very strong, appear to be corrected equally well by either motion or field correction alone, but across the board, the best results are achieved by applying both in tandem.

Beyond the similarities between simulated and experimental data in terms of how

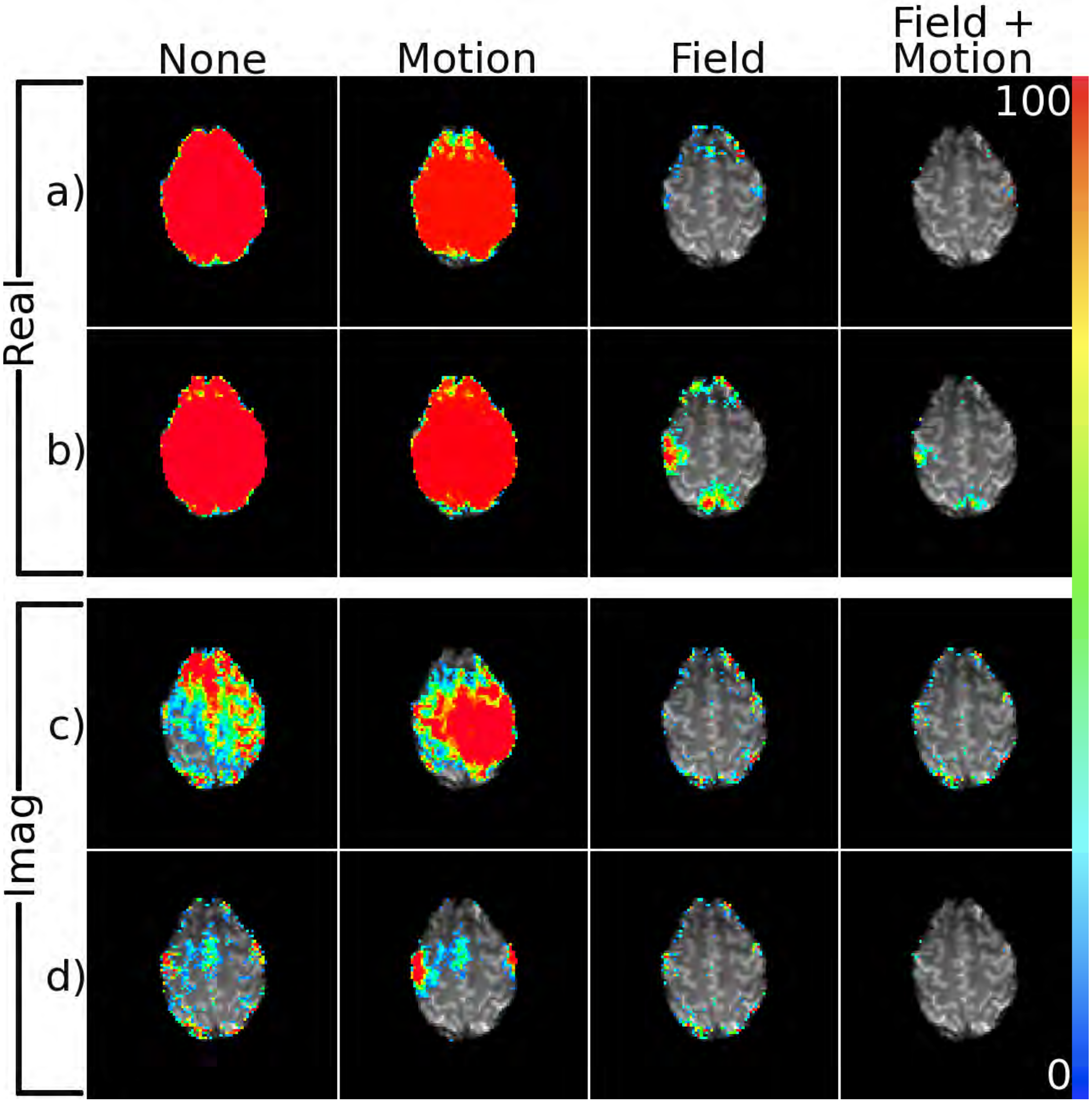

Figure 3.8: Maps of the detection power for voxel-wise Breusch-Godfrey tests of autocorrelations in the real (a,b) and imaginary (c,d) residuals of complex-valued regression at a lag of 1 after different post-processing steps. Voxels are shown when detection power is 5% or greater. Detection power is defined an the percentage of iterations a voxel tested significant at $p < .001$ (unadjusted). Results are shown for both SIMB (a,c) and SIMJ (b,d).

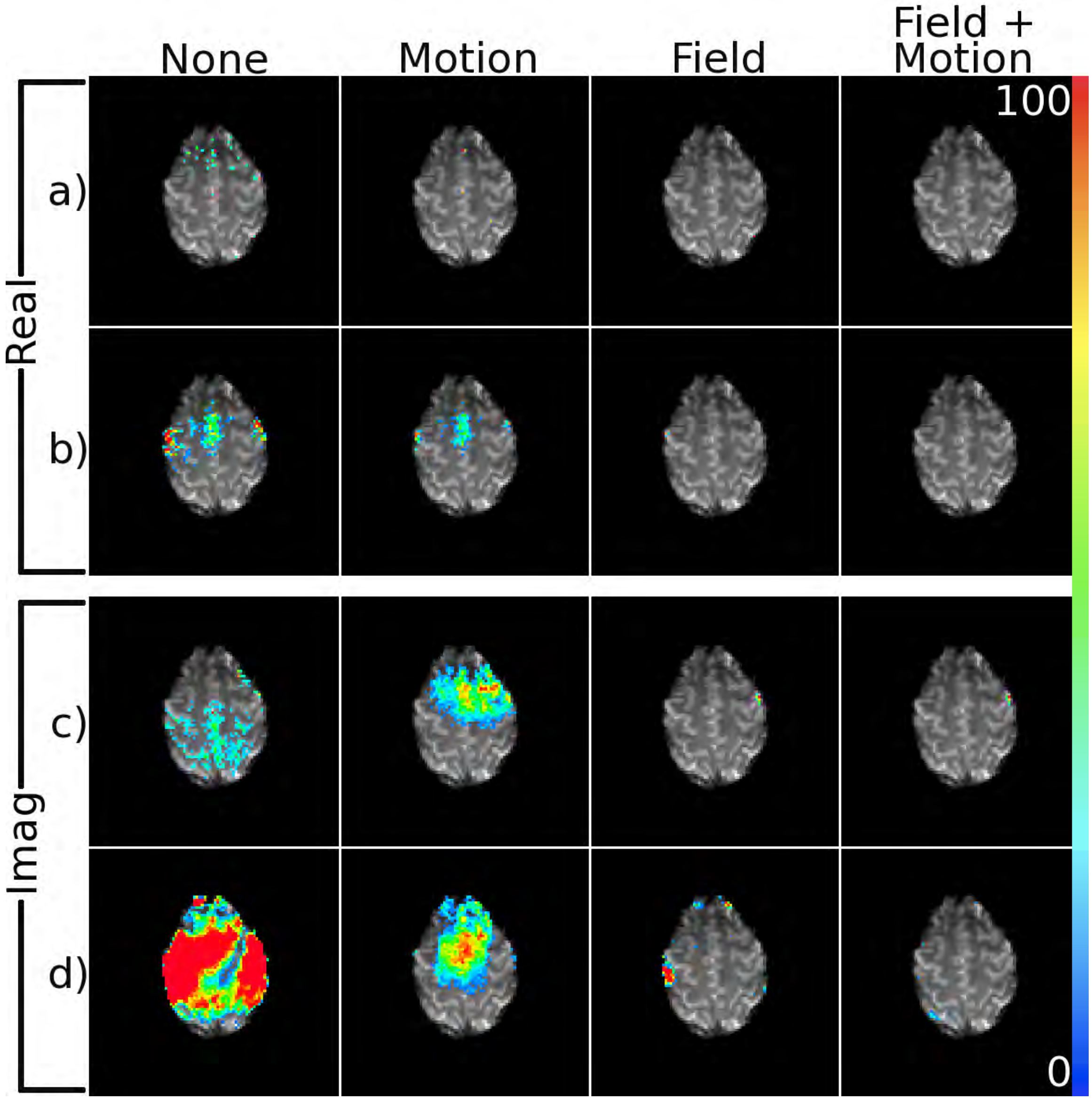

Figure 3.9: Maps of the detection power for voxel-wise Anderson-Darling tests for deviations from normality in the distributions of the real (a,b) and imaginary (c,d) residuals of complex-valued regression after different post-processing steps. Voxels are shown when detection power is 5% or greater. Detection power is defined an the percentage of iterations a voxel tested significant at $p < .01$ (unadjusted). Results are shown for both SIMB (a,c) and SIMJ (b,d).

the corrections affect the temporal signal characteristics, there also seem to be similarities between the two with respect to the pattern of autocorrelation and non-normality. Connections between them can be seen in many cases, and this helps to support the validity of the simulation and the repeatability of the corrections.

3.4 Discussion

The experimental and simulated data presented thus far have demonstrated the improvements that can be achieved with complex-valued fMRI analysis using TOAST and motion correction in situations containing known nuisance signals that are likely exaggerated compared to what will usually occur during a common fMRI experimental acquisition. While this shows that this methodology can be beneficial in more extreme and difficult cases, it does not necessarily indicate the expected benefit in more common environments. As previously mentioned, a more typical fMRI acquisition was not included in the Results section above so that the argument presented there relied on consistent, comparable data. Rather a quick inspection of the complex-valued activation statistics after performing TOAST and motion correction in a fMRI time series acquired with more common parameters and without any nuisance task is presented here for the purposes of discussion.

Figure 3.10 shows the activations detected using the model for magnitude-only (Figure 3.10a), phase-only (Figure 3.10b) and magnitude-and-or-phase (Figure 3.10c) in EXPC. The details of the acquisition of EXPC can be found in Table 3.1 and the Methods section above. The results of the magnitude-only statistics show behavior similar to what was observed in EXPB and EXPJ, i.e. little difference between each case. Phase-only results are slightly more interesting. Around the motor cortex, the results are the same as those previous in that little to no activity is present without correction and applying TOAST, and TOAST with motion correction yields activations in that area. However, without any correction, a large area of activity is detected in the anterior part of the brain that appears artifactual in nature. In this case applying the corrections removes the significant activity in this area. Finally, the magnitude-and-or-phase activity is what is expected given the magnitude-only and phase-only data. Most importantly, the significance of activations in the expected areas, i.e. motor cortex, is increased by the corrections, while the activity in the anterior brain is reduced by them. In these final results, the activity in the motor cortex, although diminished, is present with no correction at all.

Two things can be said of these results. First, it appears that some improvement, in terms of phase-only and complex-valued detection power, is possible using the two correction methods in this case. However, the degree of improvement, especially in the magnitude-and-or-phase activations, is diminished compared to that seen in EXPB and EXPJ, which is not unexpected. Second, the corrections seem to be beneficial with respect to removal of artifactual activity in this case, which was not necessarily the case in EXPB and EXPJ. It is hard to predict the occurrence of such artifacts, but it seems reasonable to think that these corrections could reduce their effects.

Rather than reduce artifacts, the use of both motion correction and field correction as opposed to simply field correction alone seemed to induce an artifact in EXPJ in the phase-only and magnitude-and-or-phase activations as previously mentioned, and it was suggested that ill-conditioning of the design matrix when including motion estimations as regressors may be a contributing factor. This potential ill-conditioning is a

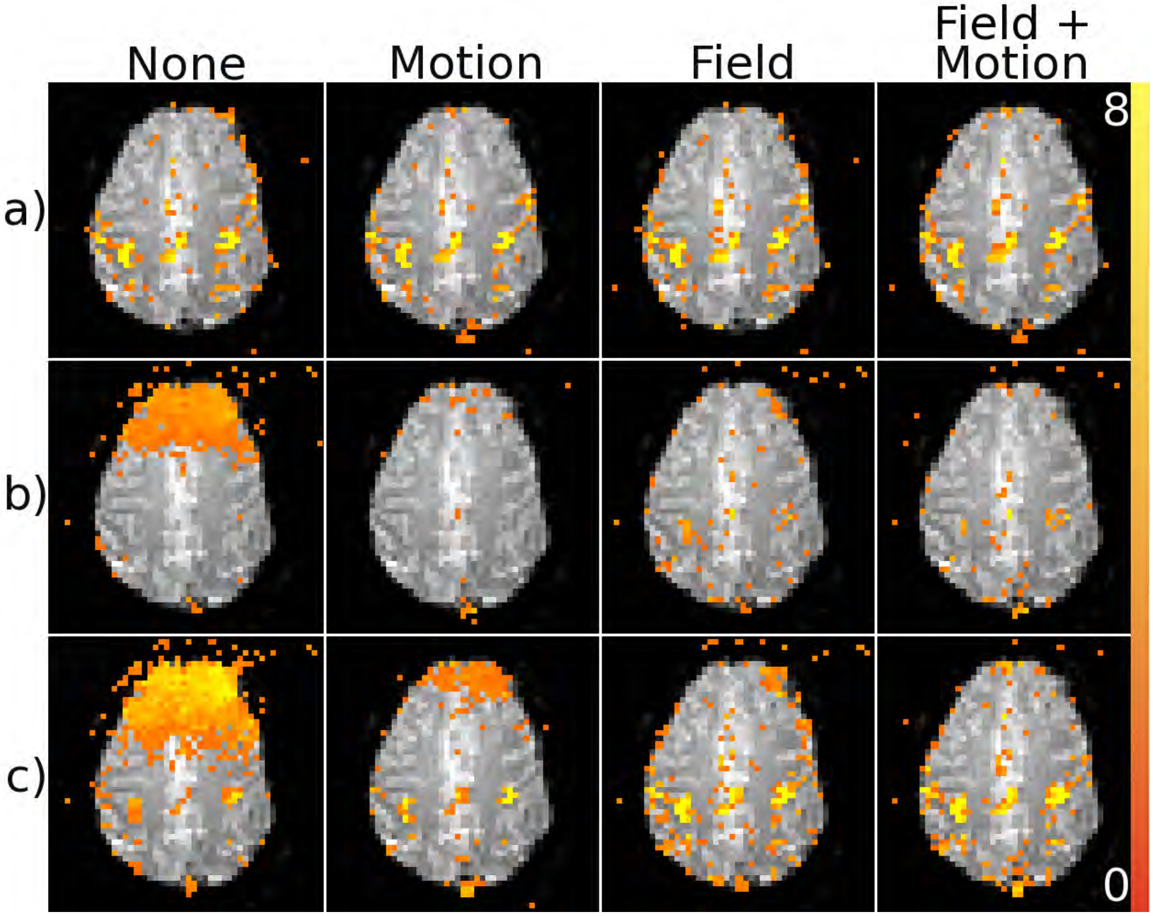

Figure 3.10: Maps of $-\log_{10} p$ where p is the p-value associated with the χ^2 statistics for magnitude-only (a), phase-only (b) and magnitude-and-or-phase (c) activation in EXPC after different post-processing corrections. Active voxels shown above a threshold of $p < 5 \times 10^{-4}$ (unadjusted).

weakness associated with performing motion compensation in this way. Additionally, certain signal components may not arise due to motion, but motion regressors can, in certain situations, account for some of the signal, reducing the significance of the task reference regressor and thus the detection of true activation. It is possible that this problem can be eliminated through use of a motion correction scheme tailored for complex-valued fMRI data, and further work is necessary to determine whether this is feasible. However, the data shows in the other cases that even this imperfect motion compensation appears to be beneficial in a general sense, and including it as a post-processing correction still provides the best results. This certainly seems to be true with regard to residual temporal autocorrelations and non-normality.

The processing techniques used to optimize the complex-valued fMRI signal presented here represent only two of the potentially useful methods. The dynamic magnetic field correction appears to provide the foundation for the demonstrated improvements, and motion correction was included because of its common use in many fMRI experiments. Additionally, these two methods alone provide a significantly more optimal and robust time series, and can be employed without any special pulse sequence modifications or physiologic monitoring during experimentation, thus may be applied to any EPI fMRI data set previously collected if the complex-valued images are available.

Additional benefit may be realized by using time series representing unwanted signal components other than motion as nuisance regressors during statistical analysis. These may be based on respiration, heart rate or any other physiologic process monitored during an experiment [32], or can be derived directly from from the acquired data itself along with a short reference scan [86, 87]. While the work of Glover et al. [32], de Zwart et al. [86] and Bianciardi et al. [87] discuss application for magnitude-only data, extension to complex-valued data is possible in the same manner used for motion parameter regression in this work. This type of technique would likely complement the field correction well, providing the capability to compensate for detrimental signal which is more spatially localized and often not associated with a bulk magnetization shift, such as cardiac induced pulsatile blood flow or modulated blood oxygenation with respiration.

The complex-valued regression analysis used in this work is only applied in a very rudimentary and straightforward manner as a means of demonstrating the initial challenges facing the technique and its potential utility following the correction processes. Further work is necessary to focus more on utilizing its flexibility to apply more appropriate complex-valued functional response models and investigate the complex-valued functional impulse response now that a foundation exists to consistently achieve a robust complex-valued time series.

Chapter 4

Physiologic noise in complex-valued time series

The complex-valued noise correction methodology which has been developed over the previous two chapters is extended again here with the addition of physiologic covariates of heart beat and respiration to the nuisance regression. As in the previous chapter, the inclusion of an additional correction motivates a comparison between different combinations of each to determine which corrections are useful under which conditions and whether a correction works better when performed with another than when performed alone. Data was acquired from a human subject, both in a "resting-state" and performing a functional task. The resting state data was analyzed almost exclusively in the phase, as physiologic covariate nuisance regression in the magnitude is well studied. We compare temporal phase variance with temporal magnitude SNR, which should have a inversely proportional relationship under ideal conditions. We also investigate the phase power spectrum after different corrections and test for significant differences between the signal power across frequencies. The fit of the physiologic covariates in the magnitude and phase is presented as well as the spatial correlation structure of the phase through time. Finally, we also compute complex-valued activations in the functional data set and compare results between corrections. We will show that including physiologic regression doesn't appear to have as great an impact on the phase time series as either TOAST or motion regression, but it does provide some benefit with respect to the phase signal (and certainly provides a benefit with respect to the magnitude signal). Interestingly, the performance of motion and physiologic regression together seems to be much better than would be expected given the results of each individually. In all, we argue that these analyses indicate that we can approach the theoretical noise limit in the phase (i.e. where phase standard deviation is equal to the inverse magnitude temporal SNR) with these corrections.

4.1 Introduction

The functional magnetic resonance imaging (fMRI) signal is corrupted not only by random thermal noise, but by systematic noise associated with bulk motion of the head as well as noise associated with heart beat and respiration. The signal not of interest due to motion is usually dealt with by estimating the motion occurring throughout the acquisition and using the estimations to register each acquired volume to a common reference using tools such as the AFNI plugin 3dvolreg [29]. Reduction of physiologic noise, on the other hand, is often accomplished by applying RETROICOR [32] using the information from physiologic recordings of the subject's heart rate and respiration during the scan. These corrections are both typically done for the magnitude of the signal only, due to the fact that phase is typically discarded when performing statistical analysis of the blood oxygenation level dependent (BOLD) fMRI to detect active brain areas [35].

It is becoming more and more likely that it may be beneficial to consider including the phase in analysis of fMRI data. First, the BOLD phase response may be non-negligible in brain areas containing uniformly oriented vasculature (typically macrovasculature) [2, 44, 61] and results have been reported that complex-valued analysis can suppress activation from these areas [44, 78]. A phase response may additionally be associated with BOLD activity in areas of microvasculature [63]. Whether the phase response in these two cases can be distinguished has yet to be shown; however it may present an opportunity to use the phase to probe the vascular structure at the site of activation. Second, it has been suggested that the response in the fMRI signal directly associated with neuronal action potentials may be manifested to some degree in the phase [10, 12, 16, 64, 65]. Whether or not this response can be detected in vivo is still not clear, but it seems most likely to be found in the complex-valued signal. Finally, statistical analysis of only the magnitude of the fMRI signal has inherent drawbacks. For one, only half the data is used which reduces statistical detection power. Noise in the magnitude is also not normally distributed, an assumption generally made in least-squares regression used to detect activation, at high signal-to-noise ratio (SNR). This is typically not a problem inside the brain given the scan parameters most commonly used, but can be an issue where B_0 field inhomogeneity causes signal dropout or in experiments with atypically high resolution or short repetition times where SNR is reduced. Recent work has also shown that non-negativity and edge effects may be problematic when performing magnitude-only BOLD fMRI analysis [88].

The apparent advantages of complex-valued statistical analysis of fMRI data begs the question as to why it is so uncommon in practice. Previous work by Nencka and Rowe [44], Hahn et al. [68, 89] have demonstrated the difficulty of complex-valued signal modeling, suggesting that unexpectedly large noise in the phase (given complementary noise in the magnitude) is the culprit. If the complex-valued signal is corrupted by thermal noise alone and SNR is high, the phase and magnitude SNR should be inversely related. Recent investigations into the noise characteristics of the phase signal have indeed shown that temporal variation in the phase is typically much larger than expected for a given magnitude SNR [34, 67]. If this additional phase variance is not accounted for, including phase in the statistical model greatly reduces detection power.

It is reasonable to assume that the sources of variance in the phase are the same as those in the magnitude, i.e. motion and physiologic phenomena such as respiration and heart rate, with the case being that these effects manifest much more strongly in the phase than the magnitude. This assumption, at least with respect to physiologic phenomena (specifically respiration), appears to have been corroborated by Petridou et al. [34], who showed that performing physiologic RETROICOR regression on the phase signal reduced phase variance by 7%-90% while similarly reducing magnitude variance by an average of 1%-2%. In white matter, the ratio of phase to magnitude SNR approached the theoretical value, but did not quite do so in grey matter. Hahn et al. [89] demonstrated a method for improving complex-valued time series characteristics with regard to residual normality and temporal autocorrelation, as well as vastly improving the utility of complex-valued activation detection. That method involved using a dynamic magnetic field mapping technique, referred to as temporal off-resonance alignment of single-echo time series (TOAST), to correct for the undesirable phase variance, in addition to incorporating a compensation for bulk motion using motion estimates as models for nuisance signal in the regression analysis.

It is the goal of this work to both compare the performance of removing physiologic sources of noise from the phase using physiologic RETRICOR regressors with TOAST and motion compensation, and to incorporate complex-valued physiologic RETROICOR regressors into the method used in Hahn et al. [89], such that TOAST is applied to remove spatially correlated noise of arbitrary sources and motion and physiologic noise sources are modeled as nuisance signal in the regression analysis used to detect activation. The performance of TOAST, motion regression and physiologic noise regression will be evaluated by investigating the phase variance, the spectral phase signal characteristics, spatial phase correlation structure and activation maps when applying different combinations of correction techniques.

4.2 Materials and Methods

4.2.1 Data Acquisition

Two fMRI data sets were acquired with a single human subject in a single scan session using a GE Signa LX 3T scanner (General Electric, Milwaukee, WI) using the stock quadrature head receiver coil, and functional images were collected with a single-shot echo planar imaging (EPI) pulse sequence (9 slices, 96 × 96 matrix, $2.5\,mm \times 2.5\,mm \times 2.5\,mm$ voxels, $42.8\,ms$ TE, $1\,s$ TR, 45° flip angle, $125\,kHz$ readout bandwidth, $0.768\,ms$ echo spacing, 510 repetitions). During both acquisitions, the echo time was increased in 2.5 ms increments from repetition 11-15 and this was repeated again for repetitions 16-20. This provided information to compute a static magnetic field offset map using the method described in Reber et al. [37]. The first of the two scans was acquired with the subject at rest, with eyes open fixated on a single point of their choice. This is similar to the type of data acquired for functional connectivity MRI [90], and thus does not include any signal fluctuations related to any explicit stimulus. During the second scan, the subject was asked to perform a simple unilateral finger tapping task, with a block design of 16 epochs of 15 s on, 15 s off, beginning at repetition 31 (repetitions 1-30 were all off). The subject was queued when to tap and when to rest visually, where the screen was black during rest and the word “tap” was displayed when the subject was to perform the finger tapping task.

The subjects respiration and heart rate were monitored during both acquisitions using a bellows belt and pulse oximeter. The pulse oximeter was placed on the hand opposite that used for finger tapping to avoid inducing artifacts in the heart rate signal.

4.2.2 Data Processing and Analysis

All acquired image data were reconstructed offline from raw GE p-files. Data processing required for image reconstruction and correction of magnetic field dynamics was done with a custom program written in C and designed in-house. The process flow for every correction method involved image generation from k-space by inverse Fourier transform, Nyquist ghost removal and correction for global, zero-order, off-resonance using three navigator echos [91] and estimation of the static magnetic field offset from repetitions 10-20 with varying echo times was performed using the method of Reber et al. [37]. To summarize these processes, the ghosting, caused by alternating shifts in the readout lines of k-space acquired in opposite directions, is corrected using the Fourier shift theorem to shift each readout line of k-space by the amount calculated from navigator echoes. The zero-order off-resonance is corrected by removing the accumulated phase due to the off-resonance, again measured from the navigator echoes, from each readout line of k-space. The phase removed from each line is dependent on the off-resonance value and the time between the acquisition of the readout line and the application of the RF excitation pulse. Calculation of the static magnetic field offset involves fitting a line to the relationship between the phase in each voxel and echo time. The slope of that line represents the static off-resonance and is computed voxel-wise. When TOAST was used, the dynamic field was found and combined with the static field map as described in [68]. Other dynamic magnetic field mapping techniques than TOAST have been proposed, such as that described by Roopchansingh et al. [45]. The basis for the choice to use TOAST opposed to another technique here is based on the discussion of the advantages and drawbacks of both TOAST and other dynamic field mapping techniques by Hahn et al. [68].

Before applying field maps in the correction, the raw maps (both static alone or the combination of static and dynamic as needed) were processed to reduce noise, while maintaining low spatial frequency information and eliminating high spatial frequency field fluctuations potentially related to desirable activity, with the goal of minimizing estimation artifacts at the image boundaries. This was accomplished by using a locally weighted least squared regression [75]. The first step in this process was to censor voxels to be used in the fitting procedure. A binary mask of voxels above 7% of the maximum voxel magnitude was generated, representing voxels within the brain. Voxels well outside the brain were selected by dilating the original mask by 10 voxels and then inverting it. These voxels had the value of the estimated field (originally only noise) set to zero. This caused the fit of the raw estimated field to fall to zero outside the brain. The voxels not contained within either of these two masks were censored and not used in the fitting procedure.

The next step involved moving voxel by voxel over the entire image and fitting a weighted two-dimensional polynomial using the 20% of all non-censored voxels which are closest (by Euclidean distance) to the current voxel. After selecting the closest 20% of voxels, a tri-cube weight function is used to weight each point according to its distance from the current point. The weight for the j^{th} point, w_j, is found using

$$w_j = \left(1 - \left(\frac{d_j}{d_{max}}\right)^3\right)^3, \tag{4.1}$$

where d_j is the Euclidean distance between the current voxel and the j^{th} voxel and d_{max} is the maximum Euclidean distance between the current voxel and a voxel within the closest 20% of non-censored voxels. The two-dimensional polynomial coefficients were fit using weighted least-squares according to

$$P = \left(X^T W X\right)^{-1} X^T W Y \tag{4.2a}$$

$$x_j = \left[1 \; d_{x,j} \; d_{x,j}^2 \; d_{y,j} \; d_{y,j}^2\right] \tag{4.2b}$$

The j^{th} row of X is x_j, and $d_{x,j}$ and $d_{y,j}$ are the distance from the current voxel in the x-direction and y-direction of the j^{th} voxel, respectively. W is a diagonal matrix, the j^{th} diagonal element of which is w_j from Equation 4.1. P is a 5-element vector containing the polynomial coefficients.

Once the coefficients for the fit were computed at a specific point, the value of the processed estimated field at that point was calculated. It should be noted that the estimated value of the voxel of interest is simply the first element of P, because the distance from itself is clearly zero in each direction (i.e. designed to be located at position $x = y = 0$).

Once this processing has been carried out, the field maps were applied using the one-dimensional (phase-encoding direction) Simulated Phase Rewinding (SPHERE) [53] correction method to remove their effects from the original images.

As a final processing step, the angular mean [58] of each voxel time series following the dynamic field correction was subtracted out to prevent phase wrapping within the imaged object. No voxels inside the object drifted more than 2π radians over the length of the experiment, especially after being corrected for the field dynamics, and zeroing the mean was sufficient in all cases to prevent wraparound in voxels within the head.

The complex-valued generalized likelihood ratio detection model used is that described in detail by Rowe [19]. In short, the model allows separate design matrices for the magnitude and phase as well as separate contrast matrices to perform arbitrary general linear tests of the significance of various linear combinations of regressors. In this work, magnitude and phase design matrices were identical (but resulted in different estimated magnitude and phase coefficients). They included a constant and linear trend in each case, and included regressors to compensate for motion, physiologic RETROICOR regressors, or both as appropriate. Motion regressors were computed using the AFNI plugin 3dvolreg [29] which yields 6 separate waveforms (3 for translational, 3 for rotational motion). If TOAST is also being used, motion was estimated after applying TOAST. Physiologic RETROICOR regressors were computed from the respiration and heart beat waveforms as described by Glover et al. [32], resulting in 8 waveforms (4 for respiration, 4 for heart rate). Modeling of the data set including finger tapping included one additional reference function in the design matrices corresponding to the task stimulus. The stimulus reference function was modeled here by a function that is simply -1 during task off periods and 1 during task on periods, shifted by $4\,s$ to account for hemodynamic delay. The shifted boxcar was chosen as opposed to a more elaborate reference curve, for example the boxcar convolved with a gamma function, for the sake of simplicity and consistency. The relative accuracy of a boxcar and an alternative model function is not well known with respect to the phase response, and will likely vary with location.

The spectra and spatial correlations of the residual phase time series following the regression were investigated and are presented in the results to follow. Additionally, activation maps showing results of tests of the significance of the stimulus reference function in both magnitude and phase are presented.

4.3 Results

Characteristics of the distribution of the phase variance, magnitude variance, and ratio of phase standard deviation to the inverse temporal magnitude SNR (tSNR) in all voxels within the brain over all 9 slices in the resting state data set ($n = 14579$) are shown following various corrections in Figure 4.1. These boxplots show the minimum, maximum, median, 1^{st} and 3^{rd} quartiles where outliers are removed if they are greater than the value of quartile 3 plus 5 times the interquartile range. The phase variance plots in Figure 4.1a show that TOAST reduces the variance by a much larger amount than either motion or physiologic regression alone, however, the use of all three provides minimum phase variance of the corrections applied. The ratio of phase standard deviation to inverse magnitude tSNR plots in Figure 4.1b again show that without TOAST, this ratio does not approach the theoretical value of 1. With TOAST alone or with TOAST and physiologic regression, however, the median ratio is near 0.965, and the 75^{th} percentile is near 1.01, indicating that nearly 75% of voxels have lower than theoretical ratios. When motion regression is added, the median rises to around 1.02 (slightly lower with TOAST and physiologic regression), indicating that the distribution is centered right around the theoretical value. The reason the ratio rises with motion regression can be seen from Figure 4.1c, which shows boxplots of magnitude variance distribution. TOAST does not change the magnitude variance distribution much (although the minimum 25^{th} and 75^{th} percentiles and the minimum median are obtained with TOAST, motion and physiologic regression), however, the motion regression significantly reduces magnitude variance and thus magnitude tSNR. It is apparent that without TOAST, motion and physiologic regression reduce phase variance more than magnitude variance, but with TOAST, motion regression does the opposite which physiologic regression seems to reduce each in equal proportions.

The square root of the power spectra (magnitude of Fourier spectra) of the phase in voxels within all 9 slices of the brain in the resting state data set ($n = 14579$) were compared to determine how well TOAST, motion regression and physiologic regres-

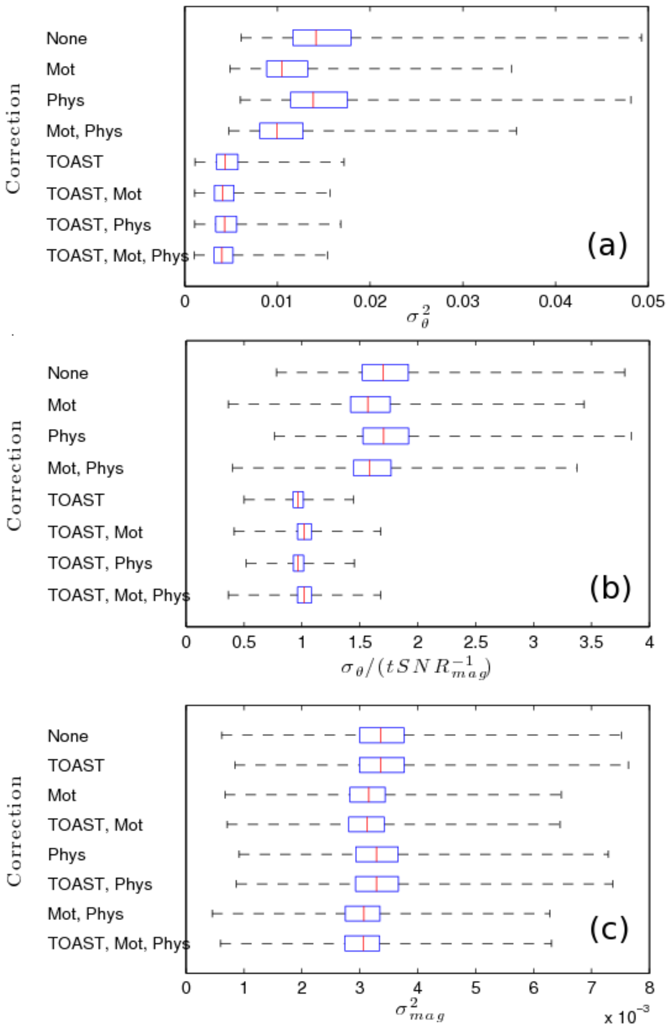

Figure 4.1: Boxplots of distribution characteristics of the phase variance, σ_θ^2, (a), the ratio of phase standard deviation to inverse magnitude temporal SNR, $\sigma_\theta/(tSNR_{mag}^{-1})$, (b) and the magnitude variance, σ_{mag}^2, (c) in all voxels within the brain over all 9 slices in the resting state data set following various corrections. For each correction, the median value is shown as a red line and the blue box is bounded on the left by the 25^{th} percentile and on the right by the 75^{th} percentile (i.e. 1^{st} and 3^{rd} quartiles). The black dotted lines show the minimum value on the left and the maximum on the right, after removing outliers. Values are considered outliers if they lie more than 5 times the interquartile range (width of blue box) above the 75^{th} percentile.

sion removed noise both individually and when used together. The square root power was used because pairwise differences in the square root of the power are normally distributed, whereas differences in power are not. This allows the significance of the mean difference in power at each frequency following different correction methods to be computed with a pairwise t-test. However, for simplicity the use of the term power going forward will refer to the square root power unless specifically noted otherwise.

The mean phase power spectrum is shown before applying any corrections in Figure 4.2a. It shows an elevation in the very low frequencies as well as a hump around 0.1 Hz. An important point should be made here considering this spectrum. The reconstruction process included a zero-order main field off-resonance correction as part of the method described in Nencka et al. [91]. This effectively removes a large amount of the constant (over space) frequency off-set, and thus the associated phase accumulated, at each time point over the acquisition. This alone immensely reduces the power in the phase near the respiration frequency especially, which is between about 0.05-0.1 Hz. If this zero-order correction is not made, the peak in the average power is many times larger than shown in Figure 4.2a. However, the zero-order off-resonance drifted over the course of the scan so severely that if left uncorrected, the images at the end of the acquisition appear shifted by nearly 6 voxels compared to those at the beginning. This drift is most likely due to gradient coil related heating, but could have other potential causes such as an instability in the shimming field. The zero-order correction almost completely fixes this. The important point here is that not only will further correction have less impact than it otherwise might have, but this may have also affected the temporal phase characteristics enough so that the physiologic regressors (specifically with respect to respiration) may no longer fit as well over the whole brain. This should be kept in mind when interpreting the results to follow.

The plots in Figures 4.2b-h show mean pairwise differenced between the uncorrected signal and the signal following various combinations of applied corrections. Additionally, red stars are shown below frequencies at which the uncorrected phase power is greater than the corrected phase power by pairwise t-test at Bonferroni corrected $p < .05$ (uncorrected $p < 2.96 \times 10^{-5}$). It should be noted that the sample size here is very large ($n = 14579$), so it requires very little positive mean difference to reach the extreme level of significance used here. While it is still a useful statistic, more qualitative comparison between correction combinations is important.

The most apparent result shown in Figures 4.2b-e, which depict the pairwise difference between the power in the uncorrected signal and the signal corrected with either TOAST (Fig. 4.2b), physiologic waveforms (Fig. 4.2c), motion (Fig. 4.2d) or both motion and physiologic waveforms (Fig. 4.2e), is that TOAST clearly performs far better than any of the others on their own (note the difference in scale in Figure 4.2b and Figures 4.2c-e). It is also interesting to note that using physiologic regressors alone makes little impact (mean difference < 0.5 everywhere), although it does significantly reduce power at a wide range of frequencies (although, mostly clustered at lower frequency). Motion regression alone does much better at very low frequency, removes a peak near 0.1 Hz, and also significantly reduced power at a range of frequencies. However, it clearly increases the power at many frequencies as well, notably around 0.025 Hz, between 0.075 Hz and 0.1 Hz, and at a few other frequencies near

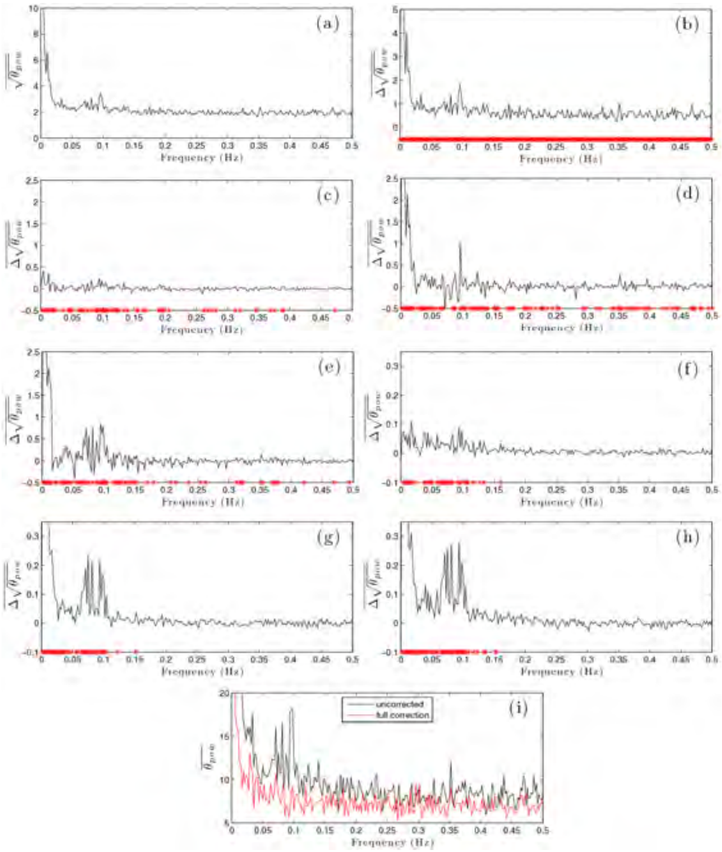

Figure 4.2: Voxels used for these plots were all those inside the brain in all slices from the resting state data set ($n = 14579$). The mean voxel square root of the phase power spectrum, $\overline{\sqrt{\theta_{pow}}}$, (i.e. the Fourier spectrum magnitude) with no correction is shown in (a). In (b)-(e), the mean of the pairwise voxel difference in square root phase power, $\overline{\Delta\sqrt{\theta_{pow}}}$, between the uncorrected data and data corrected with TOAST only (b), physiologic regression only (c), motion regression only (d), and both motion and physiologic regression (e) is shown. In (f)-(h), the mean of the pairwise voxel difference in square root phase power, $\overline{\Delta\sqrt{\theta_{pow}}}$, between the data corrected with TOAST only and the data corrected with TOAST and physiologic regression (f), TOAST and motion regression (g), and TOAST, motion and physiologic regression (h) is shown. Red stars indicate frequencies where the mean pairwise difference is significantly greater than zero at $p < .05$ threshold, Bonferroni corrected for multiple comparisons. The mean voxel phase power, $\overline{\theta_{pow}}$, with no corrections as well as after correction with TOAST, motion and physiologic regression is shown in (i).

0.15 Hz and 0.28 Hz. Interestingly, including the physiologic waveforms with motion does much better than might be expected from the results of physiologic regression alone. The power in the physiologically related frequencies (heart rate is aliased into the low frequencies near the respiration frequency) is reduced as well as very low frequency power. There are still, however, clearly multiple frequencies where mean phase power increases a substantial amount.

The fact that TOAST reduces power so much more than any of the other methods motivates Figures 4.2f-h, which show pairwise differences between phase signal power after correction with only TOAST and the phase power after correction with physiologic waveforms (Fig. 4.2f), motion (Fig. 4.2g) and both motion and physiologic waveforms (Fig. 4.2h) in addition to TOAST. This allows the relatively small, but non-negligible, effect of the regressions to be seen clearly. Similarly to the results without TOAST, the motion regression alone seems to be slightly more beneficial than physiologic regression alone. The motion regression reduces power significantly at very low frequencies as well as in the 0.05 Hz to 0.1 Hz range, while physiologic regression reduces power over a similar frequency range but to a lesser degree. In this case the combination of motion and physiologic regression performs about as one would expect. In fact, although not shown here, the mean difference between motion alone and both motion and physiologic regression (all with TOAST) yields something very similar to the difference between no regression and just physiologic regression (again with TOAST in both cases) (Fig. 4.2f). These plots also show that when applied in conjunction with TOAST, all of the regressions result almost exclusively in decreases in power, and in the few cases where mean power difference is negative, it is negligible. This is in stark contrast to what is seen without TOAST. Additionally, the frequencies which are significantly reduced by the regressions when applied with TOAST are all below 0.16 Hz. When applied without TOAST, significant power reduction was achieved over the range of frequencies. Finally, the regressions clearly have a reduced impact following TOAST (noting the scale on Figures 4.2f-h compared to Figures 4.2c-e). This is not unexpected, since it is likely TOAST removes much of the signal power that the regressions were removing in the absence of TOAST. What is being removed by regression in this case is likely spatially localized. TOAST does not remove this by design since desirable signal activity is expected to have similar spatial characteristics. In all, it is clear that the best results (in terms of mean phase signal power spectrum) are achieved using TOAST, motion and physiologic regression in tandem.

Figure 4.2i shows the mean phase power spectrum (not the square root in this case) in the fully corrected signal (TOAST and full regression) plotted in red. The original uncorrected phase power (again not the square root as in Figure 4.2a) is shown as well for reference. The improvement is clear, but there clearly remains an elevated (on average) phase power which is significantly elevated relative to higher frequency (> 0.1 Hz) components below about 0.075 Hz. Further investigation beyond the scope of this paper would be interesting to attempt to identify the source of the phase fluctuations at these frequencies.

Further investigation of the effect of complex-valued physiologic regression applied with and without TOAST is shown in Figure 4.3. The significance of the regression coefficients corresponding to the 8 physiologic RETROICOR waveforms was tested

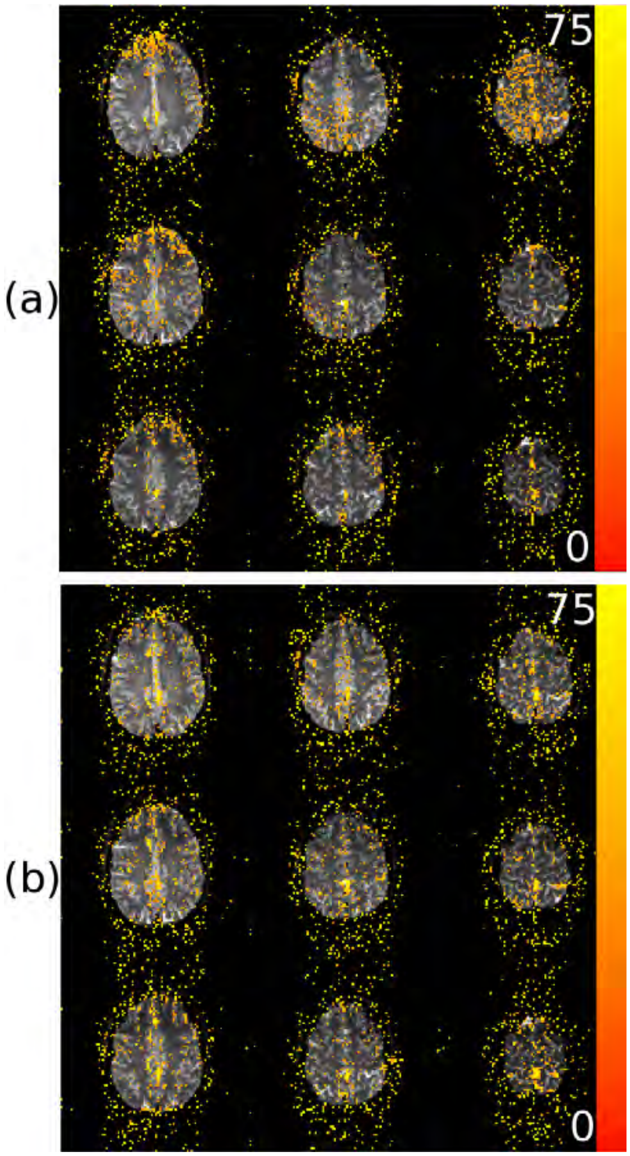

Figure 4.3: Maps of the χ^2 (16 degrees-of-freedom) statistics associated with tests of the significance of the 8 physiologic RETROICOR regressors in the magnitude-and-or-phase without TOAST (column a) and with TOAST (column b). All nine slices from inferior to superior (top to bottom, left to right) are shown from the resting state data set. Active voxels are shown above a threshold of $p < .01$ (unadjusted). Color saturates at a χ^2 of 75, corresponding to $p < 1.3 \times 10^{-9}$.

in both the magnitude and phase. The significance of each coefficient was tested individually in magnitude and phase and the test statistic resulting from the complex-valued regression was thus Chi-square distributed with 16 degrees of freedom. Figure 4.3a shows the result of the test in all slices from the resting state data set without TOAST and Figure 4.3b shows the same but with TOAST. The significance of the physiologic regressors appears increased with TOAST in certain slices but the opposite appears true in others. The physiologic regression appears to remove more phase power without TOAST than with TOAST (see Figures 4.2c and 4.2f), so one might expect much greater significance when not using TOAST. However, TOAST itself removes a large amount of phase variance so that a similar proportion of variance is removed by physiologic regression in that case as when TOAST is not used. The most important thing to notice is that the spatial distribution of significant voxels is different to some degree when TOAST is used, as opposed to when it is not. Without TOAST, there are some slices that clearly show patterns where significant voxels are grouped closely over a large area in space, which suggests that physiologic noise is present on large spatial scales. This is clearest in the anterior brain in the top slice (most inferior) and the global nature of the significant voxels in the seventh slice from the top in Figure 4.3a, although there are other locations in other slices as well. When TOAST is applied, the active voxels are much more spatially distributed, i.e. there are no large clusters of significant voxels, indicating that TOAST removed physiologic noise over large spatial scales but that residual physiologic noise is present on much smaller scales. It is worth noting when interpreting these results that the significance may be related to reduction in the variance of the phase, magnitude or both.

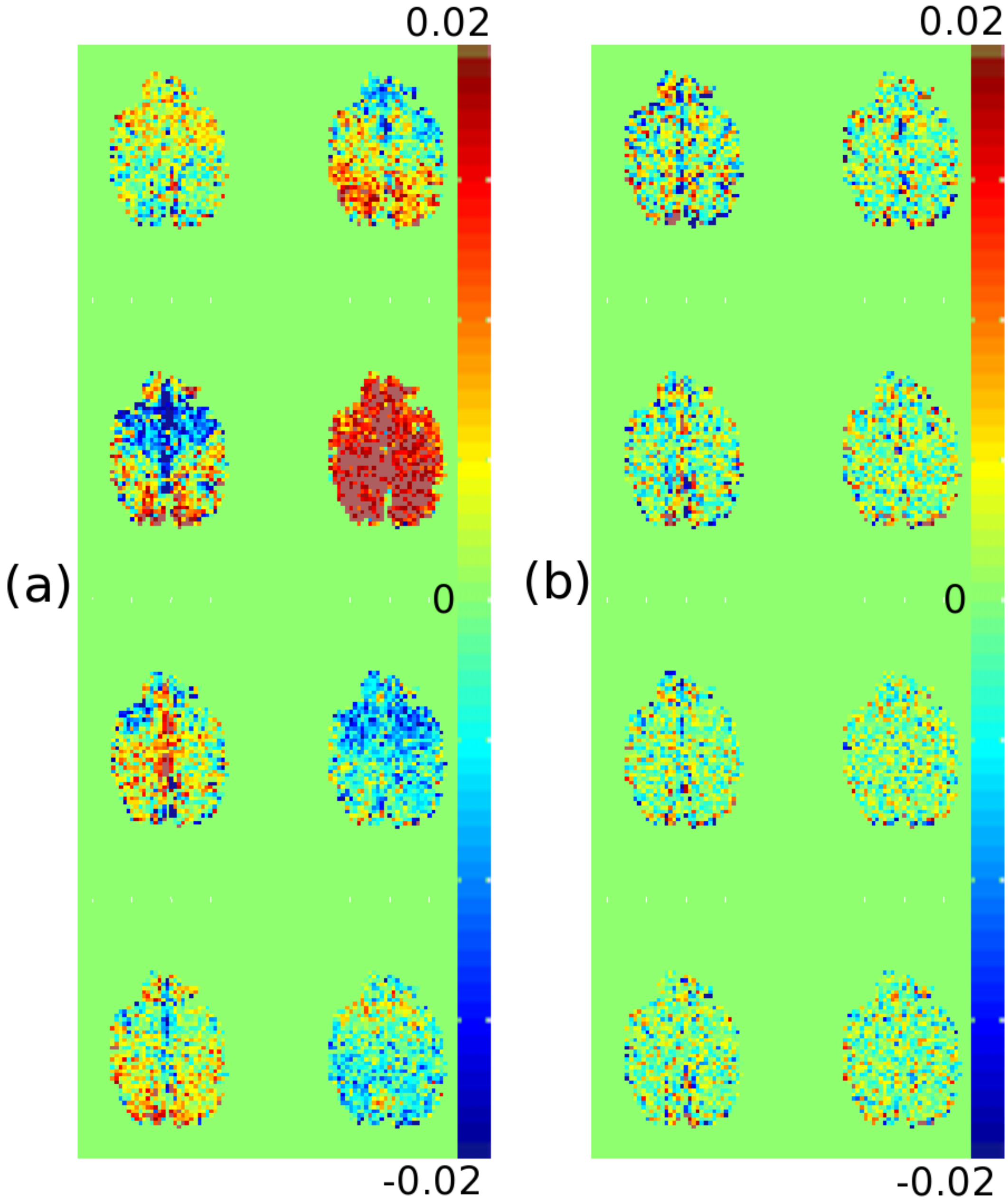

Figure 4.4: Maps of the coefficients fit to each of the 8 physiologic RETROICOR regressors in the phase in a single slice of the uncorrected data (a) and the data corrected with TOAST (b) in the resting state data set.

To determine exactly how the physiologic regressors are fit, maps of the regression coefficients for the 8 physiologic RETROICOR phase regressors are shown in Figure 4.4 for a single slice in the resting state data set. The fit of the regressors without TOAST is shown in Figure 4.4a and the fit following TOAST is shown in Figure 4.4b. It is clear that without TOAST, spatially global patterns are apparent, while following TOAST the pattern of non-zero coefficients is much more spatially localized (no large scale patterns are apparent). This corroborates the assumption stated earlier and the results in Figure 4.3 that following TOAST, physiologic regression is removing signal that exists on small spatial scales.

A final analysis of the performance of the corrections is shown in Figure 4.5. A random voxel (indicated by the dark red voxel at the center of the black square in Figure 4.5c) from within the brain was chosen from a single slice in the resting state data set. The phase residual of this voxel was then correlated with the phase residuals of every other voxel in the slice. This was done for the uncorrected signal (Figure 4.5a), the signal corrected with only motion and physiologic regression (Figure 4.5b), and the signal fully corrected with TOAST, motion and physiologic regression (Figure 4.5c). The global correlations are extreme in the uncorrected signal and are somewhat reduced after performing just motion and physiologic regression, but significant spatial correlations remain. The fully corrected signal, however, provides a much more desirable spatial correlation structure, further indicating that application of all corrections is ideal.

Activations related to the finger-tapping task in the functional data set are shown for two different slices in Figure 4.6 following different combinations of applied cor-

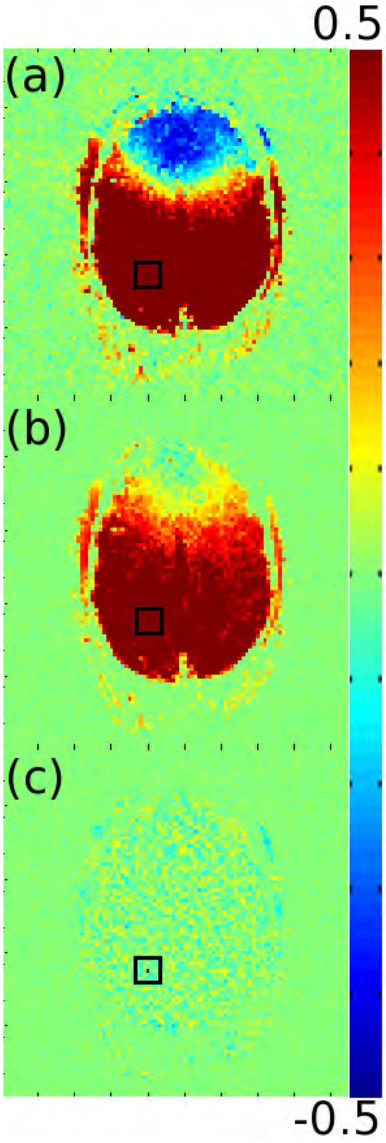

Figure 4.5: Maps of the correlation coefficients between the phase residuals in a randomly chosen voxel in the brain (at the center of the black square in a-c) and all other voxels in a single slice in the resting state data set with no correction (a), motion and physiologic regression (b), and TOAST, motion and physiologic regression (c). The red voxel in (c) is the randomly chosen voxel.

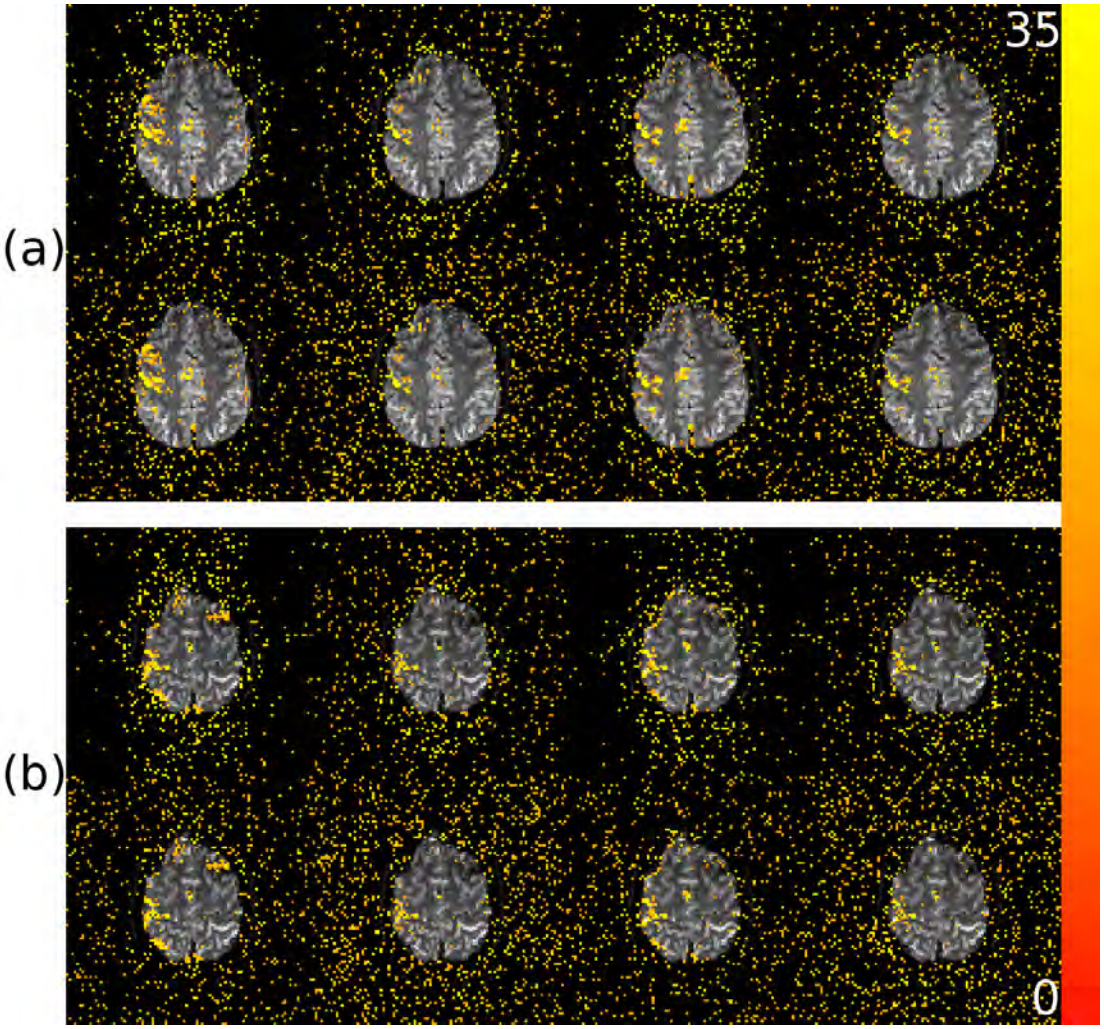

Figure 4.6: Maps of the χ^2 (2 degrees-of-freedom) statistics associated with tests of the significance of the finger-tapping stimulus reference function in the magnitude-and-or-phase. Two of the nine slices in the finger-tapping data set are shown, with a more inferior slice in (a) and a more superior slice in (b). Along the top row of both (a) and (b) from left to right are shown results of no correction, motion regression only, TOAST only, and TOAST and motion correction. The bottom row of both (a) and (b) show results following the same corrections as shown in the row above, with the addition of physiologic regression. Active voxels are shown above a threshold of $p < 5 \times 10^{-4}$ (unadjusted) and masked to show only those within the brain. Color saturates at a χ^2 of 35, corresponding to $p < 2.5 \times 10^{-8}$.

rections. Figure 4.6a shows detected activity in the magnitude and phase in one of the more inferior axial slices and Figure 4.6b shows the same for a more superior slice. Along the top row of both Figure 4.6a and 4.6b, from left to right, are shown results of no correction, motion regression only, TOAST only, and TOAST and motion correction. The bottom row of both Figure 4.6a and 4.6b show results following the same corrections as shown in the row above, with the addition of physiologic regression. Analysis similar to this has already been presented by Hahn et al. [89] for TOAST and motion regression, so this analysis will concern only the effect of physiologic regression on detected activation patters. First, though, it is worth taking notice of the fact that in the uncorrected data, significant activity is detected, where it was shown in Hahn et al. [89] that activations were nearly completely absent in uncorrected data. The difference here is the zero-order off-resonance correction was made, which acts as a crude dynamic field correction. This removes a large portion of the phase variance and makes activity apparent (although not shown, uncorrected activation patterns for this data set when the zero-order correction is not applied almost entirely disappear). However, the uncorrected results here still appear to contain significant artifactual activations, showing that the zero-order correction is not sufficient. In terms of the performance and benefit of the physiologic regression, almost no difference in the activation patterns are evident when adding physiologic regression to the correction. This is not terribly surprising given the spectral analysis previously shown. As previously mentioned, it is likely that physiologic regression would have more of an effect when the zero-order off-resonance is not applied.

4.4 Discussion

Work by Hahn et al. [89] has previously demonstrated the efficacy of TOAST, a dynamic field correction technique, and the use of motion regression in complex-valued time series with respect to time series characteristics and complex-valued statistical modeling. Here, this methodology was implemented with the addition of physiologic regression using RETROICOR regressors in complex-valued fMRI. Generally, the RETROICOR correction is made independently, prior to detection of activation. In our case, however, we implement the RETROICOR regressors directly into the complex-valued linear model. This is a more appropriate technique as all modeled waveforms, including both those of nuisance and those of functional relevance, are simultaneously fit to the data. Just as the previously mentioned work showed that the best results were obtained by applying both TOAST and motion regression, these results show that adding physiologic regression as well provides even better noise reduction. However, the addition of physiologic regression does seem to add much in and of itself.

The relatively small reduction in phase variance obtained with physiologic regression here seems much smaller than reported in previous work by Petridou et al. [34]. In fact, although the ratio of the phase standard deviation to the inverse magnitude tSNR was reduced to near the theoretical ratio of 1 over all voxels within the brain when applying TOAST with motion and physiologic regression, whether or not physiologic regression is included negligibly changes this ratio. We suspect the major reason for this is the inclusion of the zero-order off-resonance correction applied as part of the reconstruction in this work, which was not applied by Petridou et al. [34].

As previously discussed, this does much of the work of removing phase variance due to respiration in particular, due to its manifestation over large, even global, spatial scales. This is precisely what Petridou et al. [34] reported and they found that much of the reduction from phase RETROICOR was in respiratory frequencies. Thus, following zero-order off-resonance correction, less phase variation is left for physiologic regression to remove. Additionally, the zero-order correction might change the temporal characteristics of the phase noise such that the fit of the RETROICOR regressors is suboptimal. Finally, the previous work was also performed at 7T, which likely results in higher phase noise in and of itself compared to this work at 3T.

It is also interesting to note that motion regression, especially after TOAST has been applied, performs quite a bit better than physiologic regression. One reason this might be is that relatively global phase variations from off-resonance fluctuations produce the effect of bulk motion. The motion estimates pick this up and are thus best suited to remove the phase associated with this apparent motion. If the zero-order correction alters the temporal characteristics of the respiration effects, the motion estimates would pick this up, but the physiologic regressors would fail to do so. It is somewhat puzzling, however, that the combination of physiologic and motion regressors with TOAST performs much better than expected from the performance of motion or physiologic regressors alone without TOAST. This does, however, demonstrate the benefit of regressing motion and physiologic regressors simultaneously. If RETROICOR were to be applied independently first, the combined benefit shown here would likely not be obtained.

Other models of physiologic processes besides RETROICOR, for example respiration per volume time (RVT) described by Birn et al. [23] or the cardiac response function described by Chang et al. [33], may also be useful to include in noise regression. It is unlikely that including other physiologic regressors would make much difference when applied with TOAST, motion and physiologic RETROICOR corrections as done here, however. These corrections reduce the average power in the phase signal to nearly the level of high frequency power, which is likely representative of the thermal noise floor. If TOAST is not used, it is more likely that additional models of physiologic noise would provide a significant benefit.

Motion correction has been applied here only by including estimates of bulk motion as nuisance regressors in the linear model. Motion is often corrected through registration of each volume in the time series to a reference volume using the motion estimates. This is not done here because registration of complex-valued volumes is not as straightforward as registration of magnitude data alone [92]. Further work is necessary to develop a robust registration method for complex-valued image volumes, and as such, is not applied here. It is likely that doing so could provide further reduction in phase noise, however.

In all, previous literature and these results strongly suggest that TOAST is the crucial component for reducing phase noise in complex-valued fMRI data. However, the TOAST correction alone is suboptimal and further sources of noise, especially those which manifest over small spatial scales, remain and can be reduced significantly with regression of motion and physiologic regression.

Chapter 5

Applications of complex-valued artifact reduction in fMRI

A noise correction methodology has been built, tested and characterized in the work presented in the previous three chapters. It has been shown to be robust and effective, and this is supported by substantial analyses. The point of noise reduction, of course, is to perform statistical analyses more effectively. The work in this chapter demonstrates some of the complex-valued statistical analyses that might be of potential investigative interest. The emphasis on the comparison between corrected and uncorrected data is gone, since this has been well established, and we focus on a variety of complex-valued tests and analyses in the corrected data. Various potential hypothesis tests of the presence of contrast in magnitude or phase will be compared to show that all are indeed feasible and to show the differences in the test statistic significance in each. One interesting result is that the proportion of voxels containing some degree of stimulus related contrast in the phase is roughly equal to the proportion of those containing some degree of stimulus related magnitude contrast. We also investigate the complex-valued response estimated from complex-valued deconvolution and show that a variety of responses, that are duplicated in multiple data sets, appear to differ (to varying degrees) from the typical hemodynamic response function usually used to model response to stimulus.

5.1 Introduction

The typical analysis of fMRI data generally involves fitting a model of the hemodynamic response, resulting from blood oxygenated level dependent (BOLD) contrast [35], to an applied functional stimulus in the magnitude of the time series. This is a fairly robust process, evidenced by the fact that although the shape of the response varies somewhat with anatomical location [93], the response is typically strong enough that a poor model will perform well enough in most cases. However, the detection of functional response in the phase is not necessarily so similar. While some work has been published regarding detected phase response to activation [4, 63, 94], it is not nearly so well understood as the magnitude. In most of the studies, phase response is modeled identically to magnitude response, and there is certainly rationale to do so. However, there is reason to believe that information in the magnitude and phase may be quite complimentary, and different types of response in the phase may be of interest.

There are a variety of reasons why fMRI phase response is studied less than the magnitude. The most probable is due to the fact that magnitude BOLD contrast is so large and easy to detect. Another is that noise is typically much more prevalent in phase than in magnitude [34], which prevents reliable detection of activity. However, corrections have been recently developed, specifically a dynamic magnetic field mapping technique termed TOAST [68], that provide the requisite noise reduction for adequate complex-valued statistical power [68, 89]. Finally, activation related hemodynamic changes in the microvasculature are not expected to produce a phase response in the MRI signal.

Here, we will utilize these previously developed corrections to demonstrate and characterize a variety of statistical tests of functionally related contrast in complex-valued fMRI. We will show that these different potential hypotheses tests can be used with sufficient power and will also characterize the differences in the resulting test statistics between different sets of contrast tests and constraint conditions. Following these results, we will investigate the estimated functional response to stimulus in the magnitude and phase resulting from a complex-valued deconvolution. The goal is to show the types of response waveforms present in each and that, especially in the phase, these waveforms can vary quite a bit from the typical hemodynamic response function which is typically used to model the response in fMRI experimentation.

5.2 Materials and Methods

5.2.1 Data Acquisition

Two fMRI data sets were acquired with a single human subject in a single scan session using a GE Signa LX 3T scanner (General Electric, Milwaukee, WI) using the stock quadrature head receiver coil, and functional images were collected with a single-shot echo planar imaging (EPI) pulse sequence (9 slices, 96×96 matrix, $2.5\,mm \times 2.5\,mm \times 2.5\,mm$ voxels, $40.4\,ms$ TE, $1\,s$ TR, $45°$ flip angle, $125\,kHz$ readout bandwidth, $0.720\,ms$ echo spacing, 510 repetitions). During both acquisitions, the echo time was increased in 2.5 ms increments from repetition 11-15 and this was repeated again for repetitions 16-20. This provided information to compute a static magnetic field offset map using the method described in Reber et al. [37]. During both scans the subject performed a unilateral finger tapping task in a block design with 16 epochs of 15 s of task and 15 s of rest following an initial period of rest lasting 30 s. The queue alerting the subject when to rest and when to tap was provided visually on a screen, where the screen was black during rest periods and displayed the word "tap" during task periods. In addition to the functional stimulus, the subject was asked to perform a "nuisance" task as well. During the first acquisition, the subject was told to repeatedly swallow and perform a sucking action as if eating a piece of hard candy. During the second, the subject was instructed to chew as if chewing gum. These tasks were intended to induce larger than average fluctuations in the main magnetic field to provide evidence of the fact that the applied corrections were capable of handling situations that deviated significantly from ideal.

The subjects respiration and heart rate were monitored during both acquisitions using a bellows belt and pulse oximeter. The pulse oximeter was placed on the hand opposite that used for finger tapping to avoid inducing artifacts in the heart rate signal.

5.2.2 Data Processing and Analysis

All acquired image data were reconstructed offline from raw GE p-files. Data processing required for image reconstruction and correction of magnetic field dynamics was done with a custom program written in C and designed in-house. The process flow the reconstruction and correction involved image generation from k-space by inverse Fourier transform, Nyquist ghost removal using three navigator echos [91], and estimation of the static magnetic field offset from repetitions 10-20 with varying echo times which was performed using the method of Reber et al. [37]. To summarize these processes, the ghosting, caused by alternating shifts in the readout lines of k-space acquired in opposite directions, is corrected using the Fourier shift theorem to shift each readout line of k-space by the amount calculated from navigator echoes. Calculation of the static magnetic field offset involves fitting a line to the relationship between the phase in each voxel and echo time. The slope of that line represents the static off-resonance and is computed voxel-wise. TOAST was then applied by estimating the dynamic field and combining it with the static field map as described in [68].

The raw maps (both static alone or the combination of static and dynamic as needed) were processed to reduce noise, while maintaining low spatial frequency information and eliminating high spatial frequency field fluctuations potentially related to desirable activity, with the goal of minimizing estimation artifacts at the image boundaries. This was accomplished by using a locally weighted least squared regression [75]. The method used here is identical to that described in previous work by Hahn et al. [89] involving TOAST. To summarize the method, certain voxels are selectively censored to be excluded from any of the fits, and voxels well outside the brain are set to zero. Then, for each voxel, a weighted polynomial is fit to a subset of all non-censored voxels in the vicinity of the current voxel. The polynomial fit is weighted such that voxels nearer the target voxel carry more weight in the fitting model. The fit itself is accomplished using a weighted least squares estimation of the polynomial coefficients. The fitted polynomial is then used to estimate the target voxel. This is repeated for all voxels.

Once the field map processing has been carried out, the maps were applied using the one-dimensional (phase-encoding direction) Simulated Phase Rewinding (SPHERE) [53] correction method to remove their effects from the original images.

As a final processing step, the angular mean [58] of each voxel time series following the dynamic field correction was subtracted out to prevent phase wrapping within the imaged object. No voxels inside the object drifted more than 2π radians over the length of the experiment, especially after being corrected for the field dynamics, and zeroing the mean was sufficient in all cases to prevent wraparound in voxels within the head.

The complex-valued generalized likelihood ratio detection model used is that described in detail by Rowe [19]. In short, the model allows separate design matrices for the magnitude and phase as well as separate contrast matrices to perform arbitrary general linear tests of the significance of various linear combinations of regressors. In this work, magnitude and phase design matrices were identical (but resulted in different estimated magnitude and phase coefficients). They included a constant and linear trend in each case, as well as nuisance covariates to compensate for motion, respiratory and cardiovascular effects. Motion regressors were computed using the AFNI plugin 3dvolreg [29] which yields 6 separate waveforms (3 for translational, 3 for rotational motion). These were estimated following correction with TOAST. Physiologic RETROICOR regressors were computed from the respiration and heart beat waveforms as described by Glover et al. [32], resulting in 8 waveforms (4 for respiration, 4 for heart rate).

Modeling of the functional response was done using a deconvolution method [95]. The stimulus reference function was represented by a function that is -1 during task off periods and 1 during task on periods. This reference function was then lagged over the range of $0 - 14\,s$ and added to both the magnitude and phase design matrices. The resulting design matrices both had 30 columns (6 motion covariates, 8 physiologic covariates, 14 lagged stimulus references, a constant and a linear trend).

Constraint matrices were generated so that general linear tests could be performed to determine whether the estimated deconvolved response was significant. The linear constraint matrices $\mathbf{C}$ and $\mathbf{D}$, again identical for magnitude ($\mathbf{C}$) and phase ($\mathbf{D}$), were 14×30 matrices constructed by concatenating a 14×14 identity matrix onto the right of a 14×16 matrix of all zeros. Using these constraints, coefficients and residual variance were estimated under four different hypotheses: H_a: $\mathbf{C}\boldsymbol{\beta} \neq 0, \mathbf{D}\boldsymbol{\gamma} \neq 0, H_b$: $\mathbf{C}\boldsymbol{\beta} = 0, \mathbf{D}\boldsymbol{\gamma} \neq 0, H_c$: $\mathbf{C}\boldsymbol{\beta} \neq 0, \mathbf{D}\boldsymbol{\gamma} = 0,$ and H_d: $\mathbf{C}\boldsymbol{\beta} = 0, \mathbf{D}\boldsymbol{\gamma} = 0.$ Using the variance estimations from each hypothesis, 5 different general linear tests were performed to determine the significance of the deconvolution in several cases. These hypotheses are (1) H_d vs. H_a, (2) H_b vs. H_a, (3) H_c vs. H_a, (4) H_d vs. H_b and (5) H_d vs. H_c. These test for significance in (1) magnitude, phase or both, (2) significance in magnitude regardless of any phase response, (3) significance in the phase regardless of magnitude response, (4) significance in magnitude tending to bias against voxels containing functional phase response, and (5) significance in the phase tending to bias against voxels containing functional magnitude response. These tests will be performed on both data sets and comparisons made between the tests' significance to identify and confirm the type of differences they are designed to detect. Additionally, the linear regression will only be performed on voxel time series from within the brain. This can significantly reduce computational load, which is not insignificant in this case with 980 data points, 60 regressors and up to 28 simultaneous general linear tests.

The estimated functional response in each voxel will be generated by multiplying the 14 lagged stimulus regressors by the associated coefficients estimated in the linear least squares fitting procedure. This is designed to produce the response in the absence of the noise in the measured data. With this information, we can investigate the types of responses in the phase that are estimated in different areas of the brain. We also compare the estimated response to the average over all epochs in the measured data to determine whether the fit is reasonable or if there may be some artifacts induced by the fit itself.

5.3 Results and Discussion

The results from the 5 different hypothesis tests from a single slice in both data sets are shown in Figure 5.1. The slice shown here was chosen because it contained a cluster of voxels with significant phase in the interior of the brain, which most other slices do not contain (although near surface phase activations are prevalent in most slices). The observations we will make can be observed from any of the slices in the data sets. From left to right, the voxels testing above a significance threshold of $p < 5 \times 10^{-4}$ are shown for the test for magnitude and phase contrast (Fig. 5.1a,f), magnitude contrast with unrestricted phase (Fig. 5.1b,g), magnitude contrast with restricted phase (Fig. 5.1c,h), phase contrast with unrestricted magnitude(Fig. 5.1d,i)

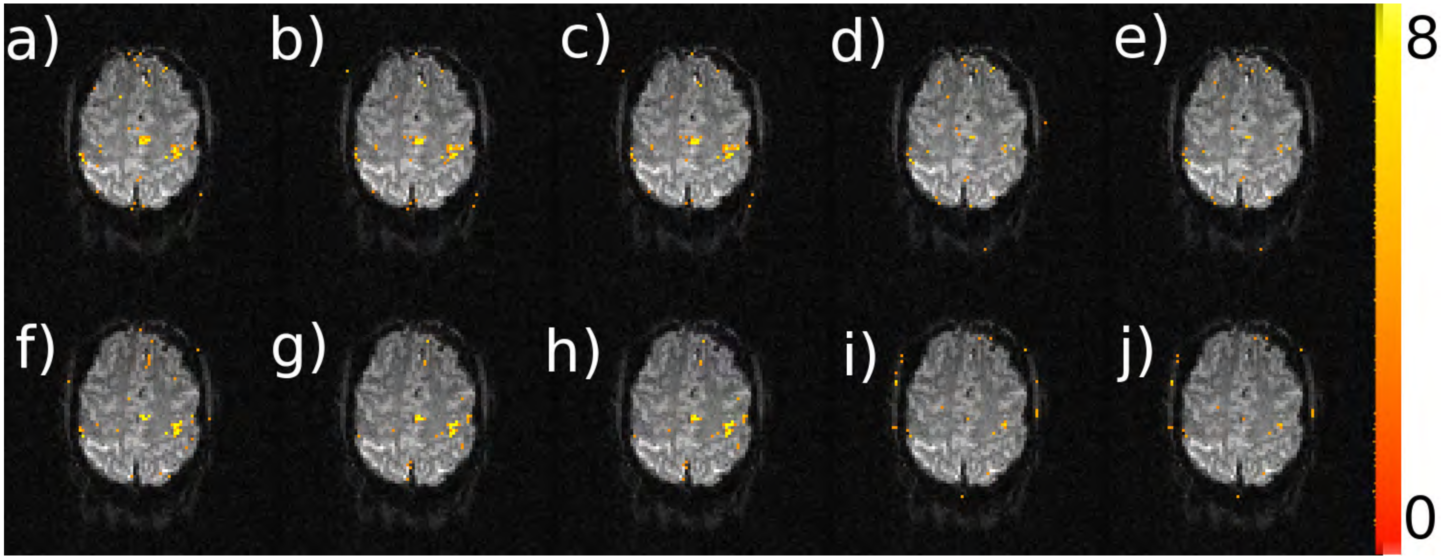

Figure 5.1: Maps of $-\log_{10} p$ where p is the p-value associated with the χ^2 statistics for magnitude and phase contrast (a,f), magnitude contrast with unrestricted phase (b,g) magnitude contrast with restricted phase (c,h), phase contrast with unrestricted magnitude (d,i) and phase contrast with restricted magnitude (e,j). The data set with swallowing is shown in (a-e) and the data with chewing is in (f-j). Active voxels shown above a threshold of $p < 5 \times 10^{-4}$ (unadjusted).

and phase contrast with restricted magnitude (Fig. 5.1e,j). For these images, the χ^2 test statistic has been converted to $-log_{10}(p)$, where p is the p-value associated with the χ^2. This normalizes the intensity across all tests, which do not all yield χ^2 statistics with equal degrees of freedom.

The first point to note is the similarity of the activation patterns between data sets. While the first does appear to have a slightly more significant response in general, the difference is relatively small and the spatial distribution is similar in both. The comparison between the effect of different hypothesis tests is also generally equivalent in both data sets. First, the test for both magnitude and phase contrast (Fig. 5.1a,f) seems to provide the greatest significance, but it is not clear whether this case or the magnitude contrast with unrestricted phase (Fig. 5.1b,g) yields more activation. There are certainly voxels in Fig. 5.1a and f that are not active in (Fig. 5.1b,g, and vise versa. This does make sense, however. Effectively, testing for contrast in the magnitude and phase simultaneously will provide greatest significance when contrast in both exists. However, if only one component contains contrast, the test for contrast in that component alone will be a stronger test. Figure 5.1 shows that the test for contrast in both signal components will yield significance where neither test for contrast in one component alone reaches significance. However, the opposite can be true as well. Of additional interest is the comparison between the magnitude/phase contrast test with the other component restricted in one case but not the other (comparisons between Fig. 5.1b,g and c,h or between d,i and e,j). Few, if any differences between the maps can be seen between the two cases in either case of the contrast being tested. One reason for this is the relatively high level of the significance threshold.

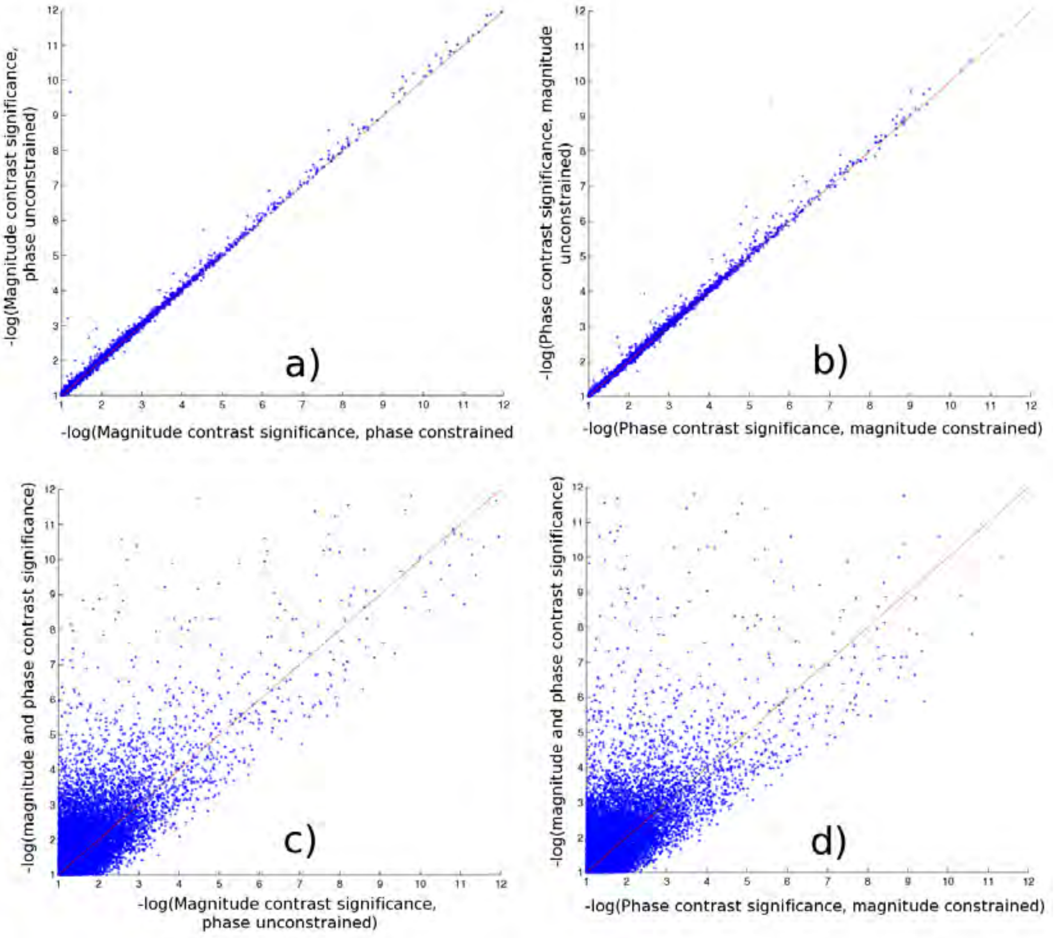

Figure 5.2: Scatter plots representing the relative significance resulting from various hypotheses tests. A point plotted at (x,y) in the scatter plot indicates a voxel that tests at $x = -log_{10}(p)$ under the contrast hypothesis on the x-axis and at $y = -log_{10}(p)$ under the hypothesis on the y-axis. The red diagonal line is the $x = y$ line. Points above the line test higher on the y-axis contrast than the x-axis contrast and vice versa. The plots in (a) and (b) show how constraining the non-contrast component (phase in (a), magnitude in (b)) can bias against voxels that contain some response in those components. Plots in (c) and (c) show that a large number of voxels are more significantly active in both magnitude and phase than only one or the other (points above red line), while some contain only magnitude or phase response (points below the red line).

The bias towards or against the significance of the statistic due to (un)restriction of the non-contrast covariates is dependent on how large the contrast is and how much variance the non-contrast covariates can account for.

We continue to investigate the differences between the statistical test results by making scatterplots of the $-log_{10}(p)$ of the test statistic in a voxel with 2 different tests to compare on the x and y axes. These scatter plots are shown in Figure 5.2. Figure 5.2a shows the magnitude contrast with restricted vs. unrestricted phase, 5.2b shows phase contrast with unrestricted vs. restricted magnitude contrast, 5.2c shows magnitude contrast vs. magnitude and phase contrast and 5.2d shows phase contrast vs. magnitude and phase contrast. In Figures 5.2c and d, the magnitude and phase contrasts have unrestricted phase and magnitude, respectively. The plotted points are those from both data sets combined. What the scatter plots show quite conclusively is what was just mentioned above. The difference between the statistics for tests of contrast in a single component (Fig. 5.2a,b) vary only a little depending on whether the non-component contrast is constrained or not. It is pretty clear that points bias somewhat towards the unconstrained non-contrast covariate case, or rather biases away from the constrained case, but most points show a small bias and thus only those hovering near the threshold will be relevant. On the other hand, the difference between the magnitude and phase contrast hypothesis test and a single component contrast results in large differences. In plots of dual contrast versus only magnitude and only phase contrast, the majority of the points are more significant using dual contrast. This indicates that these points indeed contain some degree of response in both the magnitude and phase. If this were not the case, they would instead fall

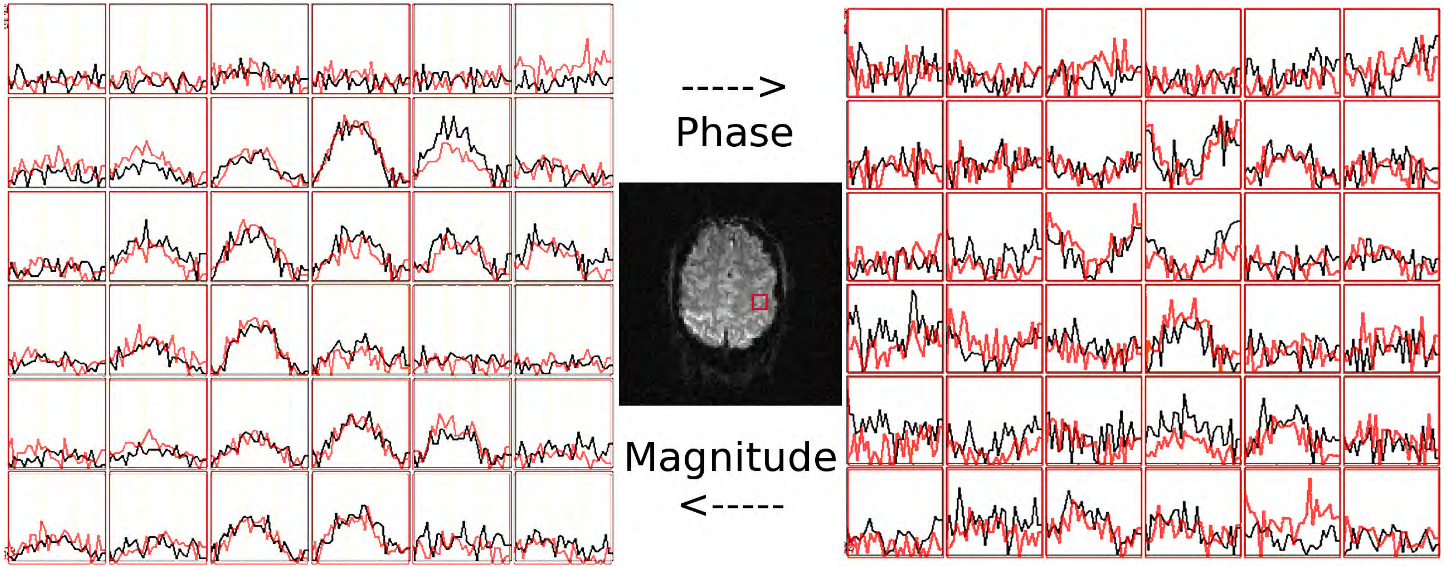

Figure 5.3: Plots of estimated voxel functional response computed by linear regression. The voxels being plotted are those contained within the red box on the central slice image. Black lines are used for plots of voxels from the chewing data set and red lines are used to plot voxels from the swallowing data set. Plot scale is constant over the cells in a matrix of plots, but may vary between matrices. The time scale on the x-axis runs from 0 to 29 seconds, where zero is the onset of stimulus.

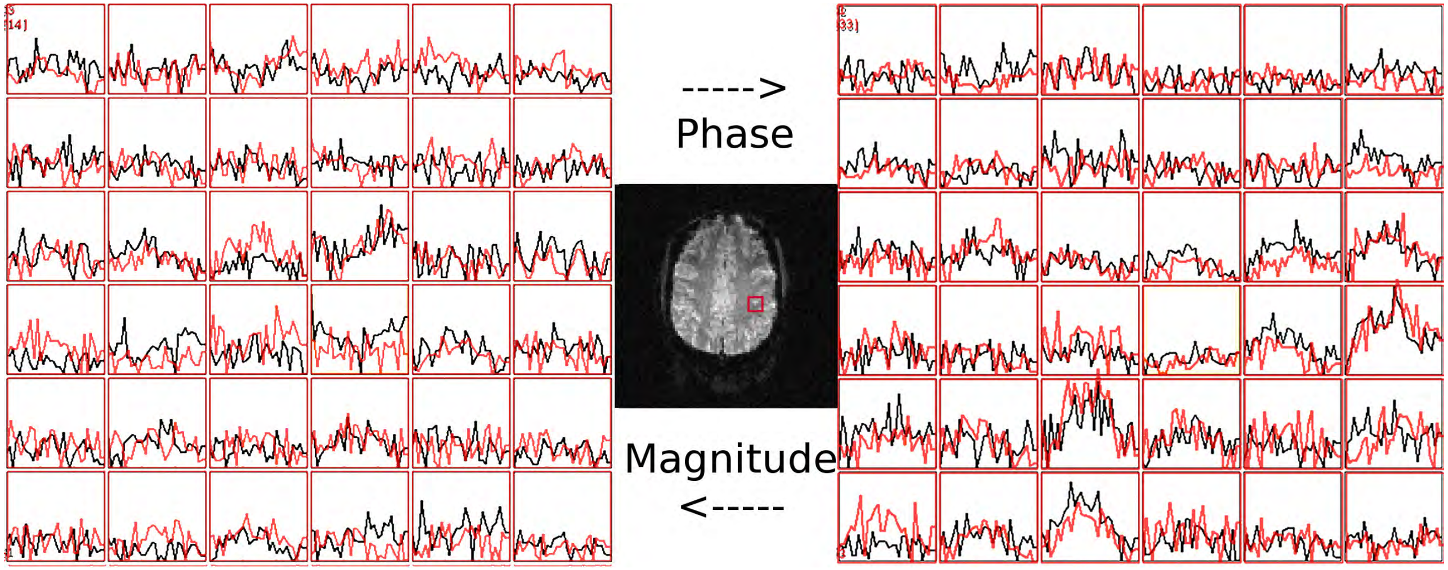

Figure 5.4: Plots of estimated voxel functional response computed by linear regression. The voxels being plotted are those contained within the red box on the central slice image. Black lines are used for plots of voxels from the chewing data set and red lines are used to plot voxels from the swallowing data set. Plot scale is constant over the cells in a matrix of plots, but may vary between matrices. The time scale on the x-axis runs from 0 to 29 seconds, where zero is the onset of stimulus.

into the strip of points that lie under the red line (representing the line where the two statistics are equal), indicating that the single contrast test is more significant. These are points that truly only have contrast in the one component. The width of the strip of points below the red line is the statistical penalty paid when testing for both magnitude and phase contrast when only single component contrast is present.

In addition to the test statistics, we also investigate the fitted response functions in the magnitude and phase. Because we performed a deconvolution, we can estimate arbitrary linear response to stimulus (although we gain this in exchange for statistical power). In Figures 5.3–5.6, we present plots of the estimated response function in both magnitude and phase over a 6×6 voxel square area in both data sets. The scales on each plot within a single grid are consistent (for both red and black lines), but may be different between grids. Each of the figures contains a map that indicates exactly where the voxels being plotted are located. The plots in Fig. 5.3–5.5 are of voxels around the area where cortical activity might be expected to occur. This is not to say that all responses in these areas are directly related to said activity. The voxels in Figure 5.6 are located in the posterior of the brain, distal from the expected area of activity and near large vasculature. A large amount of information is presented in these 4 figures, but it is provided so that two things are clear. First, the estimated responses in each dataset (chewing and swallowing data sets), which are fitted completely independently of one another, match extraordinarily well in both magnitude and phase. This is the case in many locations (nearly everywhere the response approaches significance), and we consider it to be important that substantial evidence of this is given. That the responses match between data sets strongly suggests that

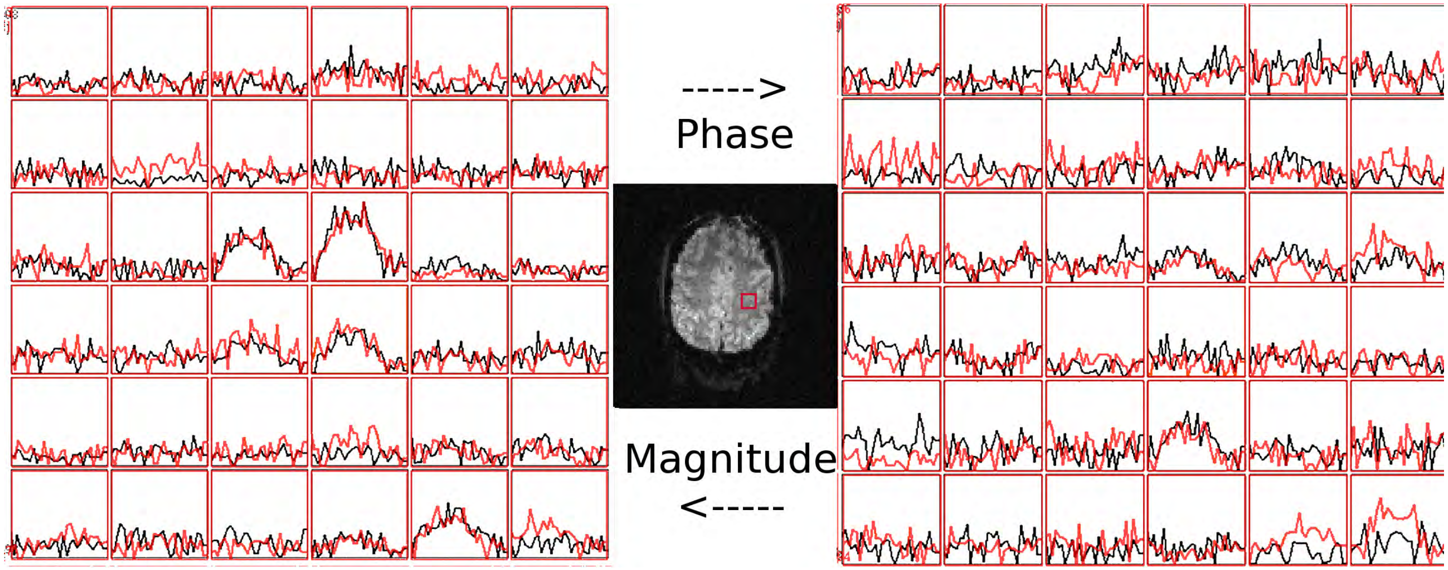

Figure 5.5: Plots of estimated voxel functional response computed by linear regression. The voxels being plotted are those contained within the red box on the central slice image. Black lines are used for plots of voxels from the chewing data set and red lines are used to plot voxels from the swallowing data set. Plot scale is constant over the cells in a matrix of plots, but may vary between matrices. The time scale on the x-axis runs from 0 to 29 seconds, where zero is the onset of stimulus.

the corrections are doing what we expect them to. We will take the opportunity to mention here the importance of the different nuisance tasks performed during data acquisition. The difference in the two nuisance tasks intentionally force the field fluctuations to be different in each data set. Not only does this provide opportunity to demonstrate that the correction can handle either case equally well, but in the event that the TOAST correction itself is inducing artifacts into the time series, this makes it very likely that the artifacts would be different in each data set. Similarly, the physiologic state and bulk motion is different during each experiment and artifacts of the nuisance regression would manifest differently in the two reconstructed time series. Because the responses seem to match quite well, we can safely assume that if the corrections induce artifacts of their own, they are very small.

The second reason we present such a large amount of data is that we want to identify a wide range of responses that, although they may not reach significance under the hypotheses which we tested, are present in both data sets and match very closely across them. If very similar responses are found in both data sets, it suggests that there may be something real behind the response, but it may be very small or simply not being tested for appropriately. In terms of variations in response waveforms, there are many. Some of it is certainly noise related variation, but certain types of waveform characteristics are repeatedly present in both sets of data. For example, the phase response in many of the voxels in Fig. 5.6, which shows voxels in the posterior brain near large vessels, is quite different, for the most part, from the response in and around the active cortex, as indicated by the plots in Fig 5.3-5.5. Another other relatively interesting characteristic evident in the phase response of

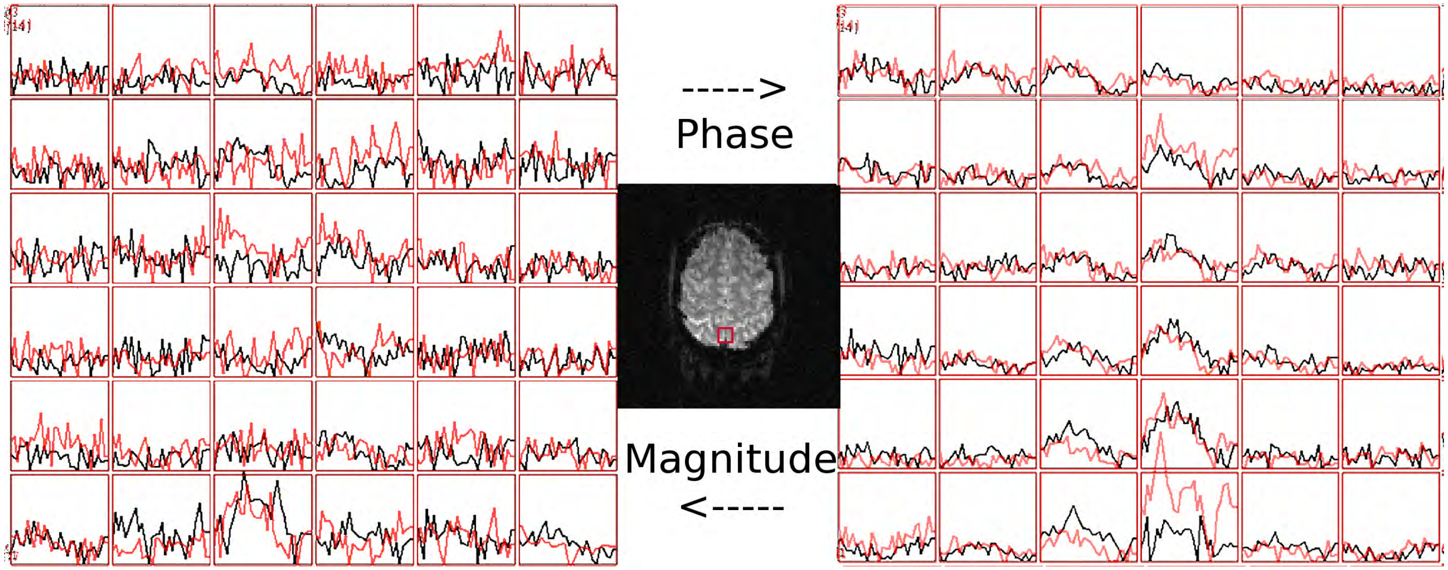

Figure 5.6: Plots of estimated voxel functional response computed by linear regression. The voxels being plotted are those contained within the red box on the central slice image. Black lines are used for plots of voxels from the chewing data set and red lines are used to plot voxels from the swallowing data set. Plot scale is constant over the cells in a matrix of plots, but may vary between matrices. The time scale on the x-axis runs from 0 to 29 seconds, where zero is the onset of stimulus.

both data sets in many voxels shown in these figures is the presence of transients, or spikes, that often occur about 4-8 seconds following stimulus onset (which coincides with $x = 0$ in these plots), and then again approximately $15\,s$ later. These timings are coincidental with the typical delay to onset of hemodynamic response function [96] and the time between them is the stimulus duration. All four figures show them to some degree, but the best examples are probably in Fig. 5.4, and Fig. 5.3 shows quite a few as well. Otherwise, the shape of the phase response seems to be quite variable, but again, similar variability is seen in both data sets suggesting that it may be somehow related to the stimulus as opposed being simply a results of noise. Of course, in certain places the phase response is very similar to the typical magnitude hemodynamic response function.

One final comparison is made in Figure 5.7 between the estimated response and the measured response averaged over all 16 epochs in both data sets from voxels in the same grid as shown in Figure 5.5. This is done to make sure that the deconvolution itself is not inducing consistent errors in the estimated coefficients. The linear regression with the lagged stimulus reference functions is about the only thing applied to both data sets that is identical. It is simply prudent to check and make sure that the measured and estimated response functions don't differ drastically. Indeed, the black (estimated) and red (epoch averaged measurement) lines plotted in Fig. 5.7 are very similar, so the least squared fitting appears to be working very well.

There really are many potentially interesting details contained in the data presented in Figures 5.3-5.6, but it is beyond the scope of this work to probe their underlying causes or the exact implications of certain types of response waveforms.

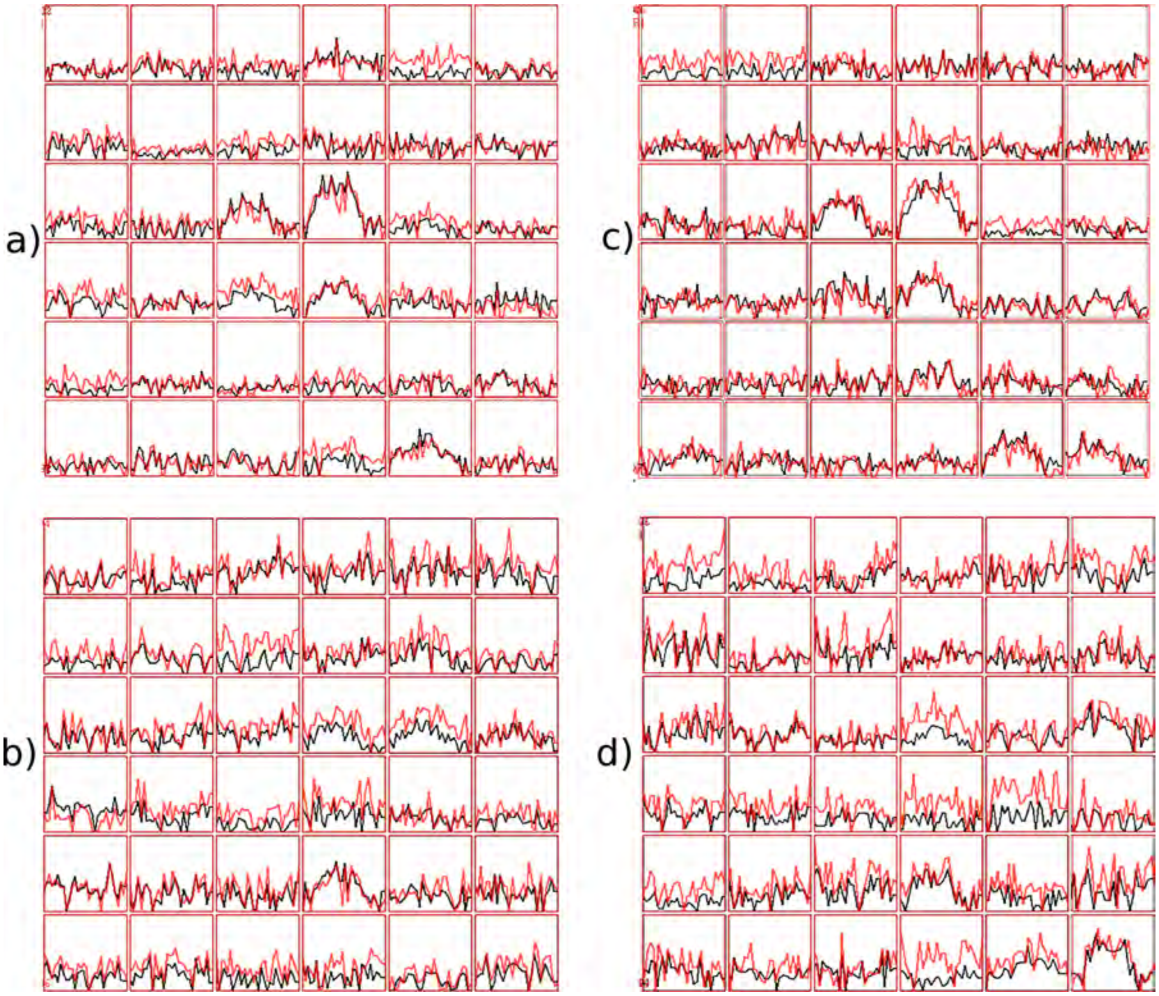

Figure 5.7: Plots of voxel functional response. The voxels being plotted are the same as those within the red box in Figure 5.5. The black lines are estimated functional response and the red lines are the measured response averaged over all 16 epochs. (a) shows the magnitude response in the chewing data set, (b) is the magnitude response in the swallowing data set, (c) shows the estimated and epoch averaged measured phase response in the chewing data set, and (d) show the same as (c) for the swallowing data. Plot scale is constant over the cells in a matrix of plots, but may vary between matrices. The time scale on the x-axis runs from 0 to 29 seconds, where zero is the onset of stimulus.

For this, extensive simulated data and well controlled and designed experimentation will be required. However, we believe that what has been presented here provides realistic experimental insight into testing for a variety of types of signal contrast in addition to demonstrating that all of these tests are feasible now that the necessary noise correction techniques have been developed and validated. Furthermore, we have shown that accurate estimation of the complex-valued response to functional stimulus is quite feasible. The similarity between the datasets, which is expected given that they are acquired from the same subject performing the same functional task, is an indication that our corrections and analysis are accurate, since there is little potential for correlated noise to be induced in the data sets in any way that has not already been ruled out. Not only can the response be estimated, but the evidence suggests that it might be worthwhile to start doing so, since the initial statistical results indicate that a large majority of voxels contain some degree of functional response in both magnitude and phase, and the complex-valued functional response may become a useful investigative tool.

Chapter 6

Conclusion

6.1 Summary of Presented Work

The research that has been presented here has followed a logical progression. From the identification and characterization of the problems inherent to complex-valued statistical analysis of fMRI time series, to development, application and verification of complex-valued noise reducing techniques, and finally a demonstration of a variety of the types of complex-valued analyses that can be applied to fMRI data sets when noise has been corrected appropriately.

We began with work, presented in chapter 2, that first attempted to apply a complex-valued constant phase model to fMRI data and showed that statistical power was greatly reduced compared to a magnitude-only model. This suggested that the problem was related to increased phase variance, as opposed to a magnitude-related issue, and we thus endeavored to find a solution for the time variant magnetic field fluctuations that were the most likely culprit for such large and spatially global phase variance. The culmination of this effort was the TOAST dynamic field correction method. We rigorously tested the method through simulation, phantom and human experimentation and characterized its performance. Most importantly, we showed that after applying TOAST to the data, statistical power was restored to complex constant phase model tests.

Because there is other noise in complex-valued time series that bulk dynamic magnetic field corrections like TOAST aren't intended to correct, we worked towards building a reliable noise correction framework over chapters 3 and 4. This involved using TOAST as a foundation for the correction and including nuisance covariates of bulk motion, respiratory and cardiovascular effects in the linear model used to detect functional activity. As the correction scheme was built upon, each of the components were analyzed in detail, both individually and as a group. We found that the best performance in terms of ideality of the corrected complex-valued time series was to perform all together as a group. An indirect benefit of this analysis was that we were able to simultaneously characterize the noise present in uncorrected acquired data. We looked at normality and autocorrelation structure of the real and imaginary time series in chapter 3, and focused more on the spectral signature of the phase, as well as the relationship between phase variance and magnitude SNR in chapter 4. In all cases, uncorrected data is very corrupted and the corrections work quite well at providing a much more ideal time series.

This complex-valued noise correction framework is put to good use in the fifth chapter. We no longer focus on the need for it or exactly what it accomplishes, as this is very well established in the previous three chapters, and can just assume with confidence that after being applied, data can be processed with complex-valued techniques as needed. We focus on showing the results of statistical tests for different combinations of functionally related contrast in the magnitude and phase fMRI signal. Following these results is an analysis of the estimated complex-valued functional response to stimulus. Two similar data sets are reconstructed, corrected and analyzed to show that this response, especially in the phase, can assume a variety of different forms, including that of a more traditional hemodynamic response function, that are found consistently in the same locations in both data sets. The message is clear that the complex-valued statistical tests are feasible in these corrected data sets and contrast in fMRI data can be detected under a variety of different constraints. Additionally, the functional phase response, which is not well understood and, frankly, understudied is shown to be of potential interest. The final determination on this matter is a potential avenue of future research.

6.2 Future Work

The stage now seems to be set for robust application of complex-valued techniques in fMRI. This suggests quite a few opportunities for future research projects. First, an effort to make complex-valued techniques standard in fMRI experimentation could be advantageous. It would make use of all of the acquired data and even if contrast in the phase is not tested for, appropriate models of its response would allow greater statistical power for detecting contrast in the magnitude.

Of course, the key phrase here is “appropriate models of its response.” Work to determine exactly what these models look like is required before complex-valued analysis can become the standard. The dependence on the phase response on the specific vascular morphology as well as the functional relationship between blood flow, blood volume and oxygen consumption makes this a potentially difficult task. Similar statements can be said about the magnitude response, and even though extensive efforts to determine precisely how these processes are manifested in the fMRI response, thorough understanding is still evasive. However, experimentation and analysis in the complex domain may provide the additional information and investigative techniques required to make the desired advancements in understanding.

Other areas of study could possibly take advantage of the work we have presented in this dissertation. One is the endeavor to directly detect neuronal currents using fMRI. Our correction framework may provide the means to determine with some degree of certainty whether neuronal current induced contrast is a feasible mechanism for studying brain function. Another is functional connectivity MRI (fcMRI). It is not certain whether complex-valued correlations are a useful way to analyze resting state data, but given that we have shown that functionally related phase response is quite prevalent and the noise reduction techniques are now available to make such study a feasible reality, it would certainly seem to be worth the effort to find out.

These are certainly not the only research topics that could potentially make use of the progress we have made through the work we have presented here. Complex-valued analytical methods are only natural in MRI given that the acquired signal is inherently complex-valued. The ability to control noise in the complex domain is an important step in the process of making complex-valued analysis a reality.

Bibliography

[1] S. Ogawa, R. S. Menon, D. W. Tank, S. G. Kim, H. Merkle, J. M. Ellermann, and K. Ugurbil. Functional brain mapping by blood oxygen level-dependent contrast magnetic resonance imaging. *Biophysical Journal*, 64:803–812, 1993.

[2] R. S. Menon. Postacquisition suppression of large-vessel BOLD signals in high-resolution fMRI. *Magnetic Resonance in Medicine*, 47(1):1–9, 2002.

[3] A. S. Nencka and D. B. Rowe. Complex constant phase method removes venous BOLD component in fMRI. *Proceedings of the International Society of Magnetic Resonance in Medicine*, 13:495, 2005.

[4] Z. Feng, A. Caprihan, K. B. Blagoev, and V. D. Calhoun. Biophysical modeling of phase changes in BOLD fMRI. *NeuroImage*, 49(4):540–548, 2009.

[5] J. A. Detre, W. Zhang, D. A. Roberts, A. C. Silva, D. S. Williams, D. J. Grandis, A. P. Koretsky, and J. S. Leigh. Tissue specific perfusion imaging using arterial spin labeling. *NMR in Biomedicine*, 7:75–82, 1994.

[6] L. Hernandez-Garcia, A. L. Vazquez, and D. B. Rowe. Complex-valued analysis

of arterial spin labeling based fMRI signals. *Magnetic Resonance in Medicine*, 63(6):1597–1608, 2009.

[7] M. D. Does, J. Zhong, and J. C. Gore. In vivo measurement of adc change due to intravascular susceptibility variation. *Magnetic Resonance in Medicine*, 41: 236–240, 1999.

[8] A. Darquié, J. B. Poline, C. Poupon, H. Saint-James, and Denis Le Bihan. Transient decrease in water diffusion observed in human occipital cortex during visual stimulation. *Procedures of the National Academy of Science*, 96(16):9391–9395, 2001.

[9] D. E. Prah, E. S. Paulson, A. S. Nencka, and K. M. Schmainda. A simple method for rectified noise floor suppression: Phase-corrected real data reconstruction with application to diffusion-weighted imaging. *Magnetic Resonance in Medicine*, 64:418–429, 2010.

[10] P. A. Bandettini, N. Petridou, , and J. Bodurka. Direct detection of neuronal activity with MRI: fantasy, possibility, or reality? *Applied Magnetic Resonance*, 29(1):65–88, 2005.

[11] L. S. Chow, G. G. Cook, E. Whitby, and M. N. J. Paley. Investigation of MR signal modulation due to magnetic fields from neuronal currents in the adult human optic nerve and visual cortex. *Magnetic Resonance Imaging*, 24(6):681–691, 2006.

[12] N. Petridou, D. Plenz, A. C. Silva, M. Loew, J. Bodurka, and P. A. Bandettini.

Direct magnetic resonance detection of neuronal electrical activity. *Proceedings of the National Academy of Sciences*, 103(43):16015–16020, 2006.

[13] L. S. Chow, A. Dagens, Y. Fu, G. G. Cook, and M. N. J. Paley. Comparison of BOLD and direct-MR neuronal detectrion (DND) in the human visual cortex at 3T. *Magnetic Resonance in Medicine*, 60:1147–1154, 2008.

[14] Q. Lou, H. Lu, D. M. Senseman, K. Worsley, Y. Yang, and J. Gao. Physiologically evoked neuronal current MRI in a bloodless turtle brain: detectable or not? *NeuroImage*, 47(4):1268–1276, 2009.

[15] D. Konn, P. Gowland, and R. Bowtell. MRI detection of weak magnetic fields due to an extended current dipole in a conducting sphere: a model for direct detection of neuronal currents in the brain. *Magnetic Resonance in Medicine*, 50 (1):40–49, 2003.

[16] L. Heller, B. Barrowe, and J. George. Modeling direct effects of neural current on MRI. *Human Brain Mapping*, 30:1–12, 2007.

[17] A. M. Cassarà, G. E. Hagberg, M. Bianciardi, M. Migliore, and B. Maraviglia. Realistic simulations of neuronal activity: a contribution to the debate on direct detection of neuronal currents by MRI. *NeuroImage*, 39(1):87–106, 2008.

[18] K. J. Worsley and K. J. Friston. Analysis of fMRI time-series revisited-again. *NeuroImage*, 2:173181, 1995.

[19] D. B. Rowe. Modeling both the magnitude and phase of complex-valued fMRI data. *NeuroImage*, 25(4):1310–1324, 2005b.

[20] M. J. McKeown, S. Makeig, C. G. Brown, T. P. Jung, S. S. Kindermann, A. J. Bell, and T. J. Sejnowski. Analysis of fmri data by blind separation into independent spatial components. *Human Brain Mapping*, 6:160–188, 1998.

[21] V. D. Calhoun, T. Adali, G. D. Pearlson, P. C. M. van Zijl, and J. J. Pekar. Independent component analysis of fMRI data in the complex domain. *Magnetic Resonance in Medicine*, 48:180–192, 2002.

[22] A. Kastrup, T. Q. Li, G. H. Glover, and M. E. Moseley. Cerebral blood flow-related signal changes during breath-holding. *AJNR American Journal of Neuroradiology*, 20:1233–1238, 1999.

[23] R. M. Birn, J. B. Diamond, M. A. Smith, and P. A. Bandettini. Separating respiratory-variation-related fluctuations from neuronal-activity-related fluctuations in fMRI. *NeuroImage*, 31(4):1536–1548, 2006.

[24] R. M. Birn, M. A. Smith, T. B. Jones, and P. A. Bandettini. The respiration response function: the temporal dynamics of fmri signal fluctuations related to changes in respiration. *NeuroImage*, 40(2):644–654, 2008.

[25] C. Chang and G. H. Glover. Relationship between respiration, end-tidal CO_2, and BOLD signals in resting-state fmri. *NeuroImage*, 47:1389–1393, 2009.

[26] M. S. Dagli, J. E. Ingeholm, and J. V. Haxby. Localization of cardiac-induced signal change in fMRI. *NeuroImage*, 9:407–415, 1999.

[27] R. M. Birn, P. A. Bandettini, R. W. Cox, A. Jesmanowicz, and R. Shaker. Mag-

netic field changes in the human brain due to swallowing or speaking. *Magnetic Resonance in Medicine*, 40(1):55–60, 1998.

[28] D. Raj, D. P. Paley, A. W. Anderson, R. P. Kennan, and J. C. Gore. A model for susceptibility artefacts from respiration in functional echo-planar magnetic resonance imaging. *Physics in Medicine and Biology*, 45:3809–3820, 2000.

[29] R. W. Cox. AFNI: Software for analysis and visualization of functional magnetic resonance neuroimages. *Computers and Biomedical Research*, 29:162–173, 1996.

[30] M. Costagli, R. A. Waggoner, K. Ueno, K. Tanaka, and K. Cheng. Correction of 3D rigid body motion in fMRI time series by independent estimation of rotational and translational effects in k-space. *NeuroImage*, 45:749–757, 2009.

[31] K. J. Friston, S. Williams, R. Howard, R. S. Frackowiak, and R. Turner. Movement-related effects in fMRI time-series. *Magnetic Resonance in Medicine*, 35:346–355, 1996.

[32] G. H. Glover, T. Q. Li, and D. Ress. Image-based method for retrospective correction of physiological motion effects in fMRI: RETROICOR. *Magnetic Resonance in Medicine*, 44(1):162–167, 2000.

[33] C. Chang, J. P. Cunningham, and G. H. Glover. Influence of heart rate on the BOLD signal: the cardiac response function. *NeuroImage*, 44:857–859, 2009.

[34] N. Petridou, A. Schafer, A. Gowland, and R. Bowtell. Phase vs. magnitude information in functional magnetic resonance imaging time series: toward understanding the noise. *Magnetic Resonance Imaging*, 27(8):1046–1057, 2009.

[35] S. Ogawa, T. M. Lee, A. R. Kay, and D. W. Tank. Brain magnetic resonance imaging with contrast dependent on blood oxygenation. *Proceedings of the National Academy of Sciences*, 87(24):9868–9872, 1990.

[36] P. Jezzard and R.S. Balaban. Correction for geometric distortion in echo planar images from B_0 field variations. *Magnetic Resonance in Medicine*, 34:65–73, 1995.

[37] P. J. Reber, E. C Wong, R. B. Buxton, and L. R. Frank. Correction of off resonance-related distortion in echo-planar imaging using EPI-based field maps. *Magnetic Resonance in Medicine*, 39(2):328–330, 1998.

[38] S. A. Kannengiesser, Y. Wang, and E. M. Haacke. Geometric distortion correction in gradient-echo imaging by use of dynamic time warping. *Magnetic Resonance in Medicine*, 42:585–590, 1999.

[39] P. F. Van de Moortele, J. Pfeuffer, G. H. Glover, K. Ugurbil, and X. Hu. Respiration induced B_0 fluctuations and their spatial distribution in the human brain at 7 tesla. *Magnetic Resonance in Medicine*, 47:888–895, 2002.

[40] R. L. Barry and R.S. Menon. Modeling and suppression of respiration-related physiological noise in echo-planar functional magnetic resonance imaging using global and one-dimensional navigator echo correction. *Magnetic Resonance in Medicine*, 54:411–418, 2005.

[41] P. Jezzard and S. Clare. Sources of distortion in functional mri data. *Human Brain Mapping*, 8:80–85, 1999.

[42] M. D. Robson, J. C. Gore, and R. T. Constable. Measurement of the point spread function in MRI using constant time imaging. *Magnetic Resonance in Medicine*, 38:733–740, 1997.

[43] D. B. Rowe and B. R. Logan. A complex way to compute fMRI activation. *NeuroImage*, 23(3):1078–1092, 2004.

[44] A. S. Nencka and D. B. Rowe. Reducing the unwanted draining vein BOLD contribution in fMRI with statistical post-processing methods. *NeuroImage*, 37 (1):177–188, 2007.

[45] V. Roopchansingh, R. W. Cox, A. Jesmanowicz, B. D. Ward, and J. S. Hyde. Single-shot magnetic field mapping embedded in echo planar time-course imaging. *Magnetic Resonance in Medicine*, 50:839–843, 2003.

[46] A. Jesmanowicz, E. C. Wong, and J. S. Hyde. Phase correction for EPI using internal reference lines. *Proceedings of the Society of Magnetic Resonance in Medicine*, 12:1239, 1993.

[47] P. Van Gelderen, J. A. de Zwart, P. Starewicz, R. S. Hinks, and J. H. Duyn. Real-time shimming to compensate for respiration-induced B_0 fluctuations. *Magnetic Resonance in Medicine*, 57:362–368, 2007.

[48] X. Hu, T. H. Parrish, and P. Erhard. Retrospective estimation and correction of physiological fluctuation in functional MRI. *Magnetic Resonance in Medicine*, 34:201–212, 1995.

[49] C. Hutton, A. Bork, O. Josephs, R. Deichmann, J. Ashburner, and R. Turner. Image distortion correction in fMRI: a quantitative evaluation. *NeuroImage*, 16: 217–240, 1995.

[50] P. van Gelderen, J. A. de Zwart, P. Starewicz, R. S. Hinks, and J. H. Duyn. Real-time shimming to compensate for respiration induced b_0 fluctuations. *Magnetic Resonance in Medicine*, 57:362–368, 2007.

[51] F. Lamberton, N. Delcroix, D. Grenier, B. Mazoyer, and M. Joliot. A new EPI-based dynamic field mapping method: application to retrospective geometrical distortion corrections. *Journal of Magnetic Resonance Imaging*, 26:747–755, 2007.

[52] H. Zeng, J. C. Gatenby, Y. Zhao, and J. C. Gore. New approach for correcting distortions in echo planar imaging. *Magnetic Resonance in Medicine*, 52:1373–1378, 2004.

[53] Y. M. Kadah and X. Hu. Simulated phase evolution rewinding (SPHERE): A technique for reducing B_0 inhomogeneity effects in MR images. *Magnetic Resonance in Medicine*, 38(4):615–627, 1997.

[54] P. A. Bandettini, A. Jesmanowicz, E. C. Wong, and J. S. Hyde. Processing strategies for time-course data sets in functional MRI of the human brain. *Magnetic Resonance in Medicine*, 30(2):161–173, 1993.

[55] D. B. Rowe and B. R. Logan. Complex fMRI analysis with unrestricted phase is equivalent to a magnitude-only model. *NeuroImage*, 24(2):603–606, 2005.

[56] L. I. Lin. A concordance correlation coefficient to evaluate reproducibility. *Biometrics*, 45:255–268, 1989.

[57] B. R. Logan and D. B. Rowe. An evaluation of thresholding techniques in fMRI analysis. *NeuroImage*, 22(1):95–108, 2004.

[58] D. B. Rowe, C. P. Meller, and R. G. Hoffmann. Characterizing phase-only fMRI data with an angular regression model. *Journal of Neuroscience Methods*, 161 (2):331–341, 2007.

[59] P. Munger, G. R. Crelier, T. M Peters, and G. B. Pike. An inverse problem approach to the correction of distortion in EPI images. *I.E.E.E. Transactions on Medical Imaging*, 19:681–689, 2000.

[60] G. Liu and S. Ogawa. EPI image reconstruction with correction of distortion and signal losses. *Journal of Magnetic Resonance Imaging*, 24:683–689, 2006.

[61] F. G. C. Hoogenraad, J. R. Reichenbach, E. M. Haacke, S. Lai, K. Kuppusamy, and M. Sprenger. In vivo measurement of changes in venous blood-oxygenation with high resolution functional MRI at 0.95 tesla by measuring changes in susceptibility and velocity. *Magnetic Resonance in Medicine*, 39(1):97–107, 1998.

[62] H. M. Duvernoy, S. Delon, and J. L. Vannson. Cortical blood vessels of the human brain. *Brain Research Bulletin*, 7(5):519–79, 1981.

[63] F. Zhao, T. Jin, P. Wang, X. Hu, and S.-G. Kim. Sources of phase changes in BOLD and CBV-weighted fMRI. *Magnetic Resonance in Medicine*, 57(3): 520–527, 2007.

[64] J. Bodurka and P. A. Bandettini. Toward direct mapping of neuronal activity: Mri detection of ultraweak, transient magnetic field changes. *Magnetic Resonance in Medicine*, 47(6):1052–1058, 2002.

[65] J. Bodurka, A. Jesmanowicz, J. S. Hyde, H. Xu, L. Estkowski, and S. J. Li. Current-induced magnetic resonance phase imaging. *Journal of Magnetic Resonance*, 137(1):265–271, 1999.

[66] D. Konn, S. Leach, P. Gowland, and R. Bowtell. Initial attempts at directly detecting alpha wave activity in the brain using MRI. *Magnetic Resonance Imaging*, 22:1413–1427, 2004.

[67] G. E. Hagberg, M. Bianciardi, V. Brainovich, A. M. Cassarà, and B. Maraviglia. The effect of physiological noise in phase functional magnetic resonance imaging: from blood oxygen level-dependent effects to direct detection of neuronal currents. *Magnetic Resonance Imaging*, 26(7):1026–1040, 2008.

[68] A. D. Hahn, A. S. Nencka, and D. B. Rowe. Improving robustness and reliability of phase-sensitive fMRI analysis using Temporal Off-resonance Alignment of Single-echo Timeseries (TOAST). *NeuroImage*, 44(3):742–752, 2009.

[69] S. Lai and G. H. Glover. Detection of BOLD fMRI signals using complex data. *Proceedings of the International Society of Magnetic Resonance in Medicine*, 3: 1671, 1997.

[70] J. Lee, M. Shahram, A. Schwartzman, and J. M. Pauly. Complex data analysis

in high-resolution SSFP fMRI. *Magnetic Resonance in Medicine*, 57(5):905–917, 2007.

[71] F. Y. Nan and R. D. Nowak. Generalized likelihood ratio detection for fMRI using complex data. *I.E.E.E. Transactions on Medical Imaging*, 18(4):320–329, 1999.

[72] D. B. Rowe. Parameter estimation in the magnitude-only and complex-valued fMRI data models. *NeuroImage*, 25(4):1124–1132, 2005a.

[73] D. B. Rowe. Magnitude and phase signal detection in complex-valued fMRI data. *Magnetic Resonance in Medicine*, 62(5):1356–1357, 2009.

[74] T. Johnstone, K. S. O. Walsh, L. L. Greischar, A. L. Alexander, A. S. Fox, R. J. Davidson, and T. R. Oakes. Motion correction and the use of motion covariates in multiple-subject fMRI analysis. *Human Brain Mapping*, 27(10):779–788, 2006.

[75] W. S. Cleveland and S. J. Devlin. Locally-weighted regression: an approach to regression analysis by local fitting. *Journal of the American Statistical Association*, 83:596–610, 1988.

[76] D. A Soltysik and J. S. Hyde. Strategies for block-design fMRI experiments during task-related motion of structures of the oral cavity. *NeuroImage*, 29(4): 1260–1271, 2006.

[77] D. A. Belsley, E. Kuh, and R. E. Welsch. *Regression Diagnostics: Identifying Influential Data and Sources of Collinearity*. John Wiley and Sons, New York, 1980.

[78] D. B. Rowe and A. S. Nencka. Complex activation surpresses venous BOLD in GE-EPI fMRI data. *Proceedings of the International Society of Magnetic Resonance in Medicine*, 14:2834, 2006.

[79] W. L. Lou and T. E. Nichols. Diagnosis and exploration of massively univariate neuroimaging models. *NeuroImage*, 19:1014–1032, 2003.

[80] L. G. Godfrey. Testing against general autoregressive and moving average error models when the regressors include lagged dependent variables. *Econometrica*, 46:1293–1302, 1978.

[81] T. S. Breusch. Testing for autocorrelation in dynamic linear models. *Australian Economic Papers*, 17:334–355, 1979.

[82] J. Durbin and G. S. Watson. Testing for serial correlation in least squares regression, III. *Biometrika*, 58:1–19, 1971.

[83] T. W. Anderson and D. A. Darling. Asymptotic theory of certain 'goodness-of-fit' criteria based on stochastic processes. *Annals of Mathematical Statistics*, 23: 193–212, 1952.

[84] M. A. Stevens. EDF statistics for goodness of fit and some comparisons. *Journal of the American Statistical Association*, 69:730–737, 1974.

[85] S. S. Shapiro and M. B. Wilk. An analysis of variance test for normality (complete samples). *Biometrika*, 62:591–611, 1965.

[86] J. A. de Zwart, P. van Gelderen, M. Fukunaga, and J. H. Duyn. Reducing correlated noise in fMRI data. *Magnetic Resonance in Medicine*, 59(4):939–945, 2008.

[87] M. Bianciardi, P. van Gelderen, J. H. Duyn, M. Fukunaga, and J. A. de Zwart. Making the most of fMRI at 7 T by suppressing spontaneous signal fluctuations. *NeuroImage*, 44(2):448–454, 2009.

[88] Z. Chen and V. D. Calhoun. Two pitfalls of BOLD fMRI magnitude-based neuroimage analysis: non-negativity and edge effect. *Journal of Neuroscience Methods*, In Press, doi:10.1016/j.jneumeth.2011.05.018, 2011.

[89] A. D. Hahn, A. S. Nencka, and D. B. Rowe. Enhancing the utility of complex-valued functional magnetic resonance imaging detection of neurobiological processes through postacquisition estimation and correction of dynamic B_0 errors and motion. *Human Brain Mapping*, In Press, doi: 10.1002/hbm.21217, 2011.

[90] B. B. Biswal, F. Z. Yetkin, V. M. Haughton, and J. S. Hyde. Functional connectivity in the motor cortex of resting human brain using echo-planar MRI. *Magnetic Resonance in Medicine*, 34(4):537–541, 1995.

[91] A. S. Nencka, A. D. Hahn, and D. B. Rowe. The use of three navigator echoes in Cartisian EPI reconstruction reduces Nyquist ghosting. *Proceedings of the International Society of Magnetic Resonance in Medicine*, 16:3032, 2008.

[92] A. D. Hahn and D. B. Rowe. Methodology for robust motion correction of

complex-valued fMRI time series. *Proceedings of the International Society of Magnetic Resonance in Medicine*, 18:3051, 2010.

[93] M. A. Beau, O. Leontiev, J. E. Perthen, C. Liang, A. E. Lansing, and R. B. Buxton. Regional differences in the coupling of cerebral blood flow and oxygen metabolism changes in response to activation: implications for BOLD-fMRI. *NeuroImage*, 39(4):1510–1521, 2008.

[94] S. K. Arja, Z. Feng, Z. Chen, A. Caprihan, K. A. Kiehl, T. Adali, and V. D. Calhoun. Changes in fMRI magnitude data and phase data observed in block-design and event-related tasks. *NeuroImage*, 49(4):3149–3160, 2010.

[95] N. Wiener. *Extrapolation, Interpolation, and Smoothing of Stationary Time Series.* MIT Press, Cambridge, MA, 1964.

[96] A. T. Lee, G. H. Glover, and C. H. Meyer. Discrimination of large venous vessels in time-course spiral blood-oxygen-level-dependent magnetic-resonance functional neuroimaging. *Magnetic Resonance in Medicine*, 33(6):745–54, 1995.

Signature Page

This dissertation was prepared under the direction of the chairperson of Andrew David Hahn's supervisory committee and has been approved by all members of that committee. It was submitted to the Dean of the Graduate School of Biomedical Sciences, Medical College of Wisconsin and was approved as a partial fulfillment of the requirements for the degree of Doctor of Philosophy.

Committee in Charge:

Daniel Rowe	Chairperson
Gary Glover	
James Hyde	
Robert Prost	
Kathleen Schmainda	
Ravi Misra	Dean of the Graduate School of Biomedical Sciences